Spin Structure of the Proton and the Q^2 Evolution of the Gerasimov-Drell-Hearn Integral

by

Alexander Skabelin

B.S., Moscow Institute of Physics and Technology (1994)

Submitted to the Department of Physics
in partial fulfillment of the requirements for the degree of

Doctor of Philosophy in Physics

at the

MASSACHUSETTS INSTITUTE OF TECHNOLOGY

February 2002

Author . . . .

Department of Physics

December 18, 2001

Certified by . . . .

William Bertozzi

Professor of Physics

Thesis Supervisor

Accepted by . . . .

Thomas J. Greytak

Professor of Physics

Associate Department Head for Education

Spin Structure of the Proton and the Q^2 Evolution of the Gerasimov-Drell-Hearn Integral

by

Alexander Skabelin

Submitted to the Department of Physics
on December 18, 2001, in partial fulfillment of the
requirements for the degree of
Doctor of Philosophy in Physics

Abstract

We studied the inclusive reaction $\overrightarrow{e}\overrightarrow{p} \rightarrow e'X$ with a $2.5GeV$ and a $4.2GeV$ incident beam of polarized electrons. The virtual photon four momentum squared, Q^2, varied from $0.2GeV^2/c^2$ to $1GeV^2/c^2$ and the center of mass total energy W ranged up to $2GeV$. The measurement was performed at the CEBAF Large Acceptance Spectrometer (CLAS) of the Thomas Jefferson National Accelerator Facility during the Fall of 1998. A cryogenic NH_3 target was used as a source of protons polarized in the direction of the incident electron beam. For the first time, proton spin structure functions were studied with precision in the resonance region. The data indicate that a dramatic change in the spin structure occurs between the deep inelastic high Q^2 region and the region of low Q^2 where photons become nearly real.

Thesis Supervisor: William Bertozzi
Title: Professor of Physics

Contents

List of Figures

List of Tables

Chapter 1

Physics Motivation

1.1 Introduction

The main objective of physics is to describe nature. Most of matter is built from three building blocks: protons, neutrons and electrons. It is natural that understanding the structure and laws of the interactions between these fundamental building blocks is of paramount importance to physics as a science. We have spent many decades trying to understand the electron, which appears to be the simplest block. This investigation resulted in the creation of the most successful theory so far, which is Quantum Electrodynamics (QED). It brought with it numerous benefits to society such as lasers, computers and cellular phones, and completely changed the world around us. The investigation of protons and neutrons, on the other hand, started relatively recently, in the 20th century. We are at the beginning of this new investigation and we can already show that we have brought benefits to society.

Phenomenologically, protons and neutrons (collectively called nucleons) can be described by structure functions. An important property of electrons and nucleons is that they are spin $\frac{1}{2}$ fermions. The existence of the intrinsic spin creates new degrees of freedom. These polarized degrees of freedom provide much more information about the structure of the nucleon than unpolarized degrees only. If we are to completely describe the nucleons, we have to investigate polarized degrees of freedom and perform experiments in which both the electrons and nucleons are polarized.

At this point in time we have a good understanding of the static properties of the proton and neutron at zero energy, which corresponds to looking at a nucleon with a poor resolution microscope. The spin, the charge, the mass and the magnetic moment have been successfully measured and are the only properties that the static nucleon has. However, there is another side of the resolution spectrum. We can create special conditions in the lab that will correspond to looking at a nucleon with a very high resolution. This regime is called Deep Inelastic Scattering (DIS); it can be well described by Quantum Chromodynamics (QCD).

Unfortunately the world around us corresponds to neither of these limiting cases. Most matter is governed by energies of the order of the nucleon mass or less. This intermediate region is precisely that which is the least understood. Building a successful theory in this region will require incorporation of our knowledge of both the Deep Inelastic and Static properties of the nucleon. This is a very challenging problem. Even the relevant degrees of freedom are different in these two regimes: Deep Inelastic Scattering is described by quarks and gluons, while low energy phenomena are described by mesons and nucleons. Bringing two descriptions together and forming a complete picture of the nucleon is one of the most important problems in contemporary physics. To tackle this problem, state of the art facilities such as the Jefferson Laboratory have been built. This laboratory hosts an electron accelerator that allows us to study the electron-hadron interaction in the intermediate energy region with an unprecedented precision.

We can ask ourselves what would be the best tool for studying the transition between these two regimes, and, for bringing these two diverse pictures together. One conclusion is that a good approach is one that is uniform internally (uses the same degrees of freedom) in its description of the nucleon starting from low and ending at high resolution. Fortunately such a tool exists. The work of Gerasimov in 1965 [2], [3] gave us an important sum rule that describes the interaction of nucleons with real photons (zero resolution). This sum rule is discussed in Section 1.4. The sum rule can be naturally generalized to virtual photons (non zero resolution). The DIS limit of the Gerasimov sum rule has a clear interpretation in terms of the DIS structure functions. This limit is also related to the famous Bjorken sum rule [4] that connects properties of protons and neutrons in the DIS region. The Bjorken sum rule is discussed in Section 1.6.

Protons and neutrons are both poorly understood at moderate Q^2. The neutron, being neutral and unstable in its free state, is a much harder object to deal with experimentally. In this thesis we will concentrate exclusively on the proton.

To summarize:

1) Nucleons are the main building blocks of the Universe but so far they are not well understood.

2) The intermediate energy region is an important one and one of the least understood.

3) Polarization degrees of freedom are very important.

4) The generalized Gerasimov sum rule is an important tool because of its uniform treatment of the entire region, starting from low resolution and ending at very high resolution.

5) An excellent experimental facility in the region of interest is the Jefferson Laboratory.

1.2 Notations and Conventions Used in the Text

We will use the standard convention where the speed of light in the vacuum, c, and Planck's constant, $\frac{h}{2\pi}$, are both equal to one. Most of the time we will use all physical quantities in the form of 4-vectors instead of 3-vectors. Letters with Greek subscripts and superscripts, e.g., k_μ and k^μ, are 4-vectors while Latin letters are used for 3-vectors, e.g., l^a. The metric tensor $g^{\alpha\beta}$ has the following form: $g^{00} = 1, g^{ii} = -1, g^{ij} = 0$ for $i \neq j (i, j = 1, 2, 3)$. The fine-structure constant, $\frac{e^2}{\hbar c}$, is denoted by α. The Dirac gamma matrices are denoted by γ^ν with $\gamma_5 = i\gamma^0\gamma^1\gamma^2\gamma^3$. The Dirac sigma matrices are defined by:

$$\sigma^{\mu\nu} = \frac{i}{2}[\gamma^\mu, \gamma^\nu]. \tag{1.1}$$

$[\gamma^\mu, \gamma^\nu]$ is the anti-commutator of two gamma matrices. The proton mass is taken to be

$$M_p = 938 MeV. \tag{1.2}$$

The proton charge is expressed in units of the electron charge e, and the anomalous magnetic moment $\mu_a = 1.793$ is expressed in units of the nuclear magneton $\frac{e}{2M_p}$.

1.3 Inclusive Electro-production

It is possible to study nucleon structure by colliding nucleons or by colliding nucleons with electrons. The second method is superior to the first in many ways. The main advantage is that the electron as a projectile has a very well understood structure. Therefore, the interpretation of the experimental results is a relatively straightforward task. Nuclen-nucleon collisions, on the other hand, have both the target and the projectile as structurally unknown quantities. The advantage of the nucleon-nucleon or nuclei-nuclei collision is that one can achieve higher center of mass energies. This is mainly because both particles have high mass while the electron is very light. This advantage, however, is of no relevance to us since the Jefferson Laboratory has sufficient energy to do the job. Therefore, we conclude that an electron-nucleon facility such as the Jefferson Laboratory would be one of the best places to study nucleon structure in the intermediate Q^2 region.

The next important question is what would be an interesting reaction to concentrate on. We can argue that, as a first look, the inclusive reaction, being an average of all the reaction channels, is the right place to start. Global properties of the nucleon as well as the important Gerasimov sum rule are directly related to the inclusive reaction.

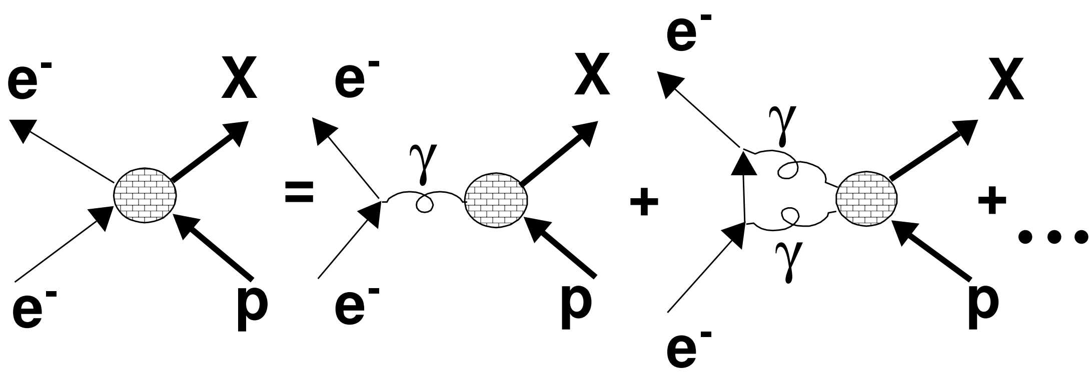

Figure 1-1: Inclusive electron scattering from a nucleon.

1.3.1 Formalism

We consider polarized inclusive electron scattering in the laboratory frame with a stationary target of polarized nucleons. We work in leading order of the electromagnetic interaction but in all orders of the strong interaction. The leading order of the electromagnetic interaction corresponds to the first diagram in the decomposition presented in the Fig. 1-1. Since the energies under consideration are of the order of GeV we will consistently neglect the electron mass $m_e = 0.5MeV$. The energy of the incident and scattered electrons we denote as E and E', respectively. The incident and scattered electron 4-momenta will be k and k':

$$k^{\nu} = (E, \overrightarrow{k}), \tag{1.3}$$

$$k'^{\nu} = (E', \overrightarrow{k}'). \tag{1.4}$$

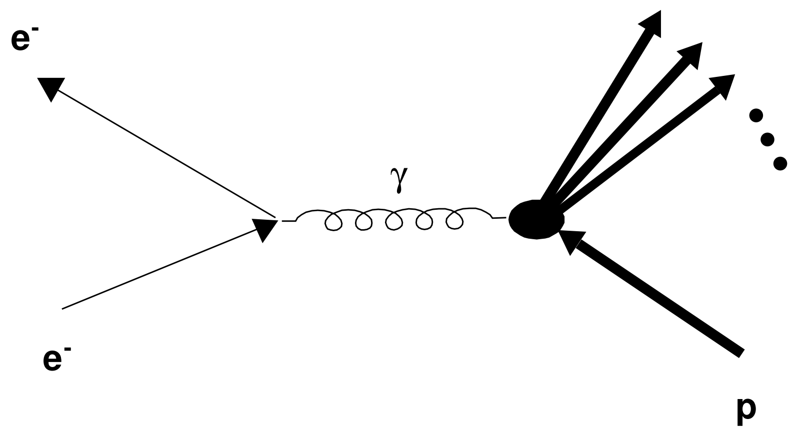

Figure 1-2: Inclusive electron scattering from a nucleon. First order diagram of the electromagnetic interaction.

We use the convention of writing 4 vectors as letters with Greek subscripts and superscripts (k^ν, k_μ and etc.). The energy transfer we denote as ω

$$\omega = E - E'. \tag{1.5}$$

Because we are working in the first order of QED, ω is the energy of the intermediate virtual photon. The 4-momentum of the virtual photon is

$$q^\nu = k^\nu - k'^\nu = (\omega, \overrightarrow{k} - \overrightarrow{k'}). \tag{1.6}$$

where the first component of a 4-momentum is energy and the last three components are the three space parts of the momentum.

As we can see from the equation below, the virtuality of the photon, q^2 is always negative for electro-production. Therefore, we will introduce a notation $Q^2 = -q^2$:

$$Q^2 = -q^2 = 2EE'(1 - cos\Theta_e) = 4EE'sin^2\frac{\Theta_e}{2}, \tag{1.7}$$

where Θ_e is the polar scattering angle of the electron. For a real photon, $q^2 = 0$.

The initial 4-momentum of the nucleon we denote by p with

$$p^\nu = (M, \overrightarrow{0}). \tag{1.8}$$

In the inclusive electro-production (Fig. 1-2) we detect only the scattered electron. Its scattering polar angle Θ_e, azimuthal angle ϕ_e and energy E' are the only experimental observables coming from the final state. The polarization of the scattered electron is not detected. The polarization of the incident electron as well as the polarization of the target nucleon are presumed to be known for the double polarization measurements that we discuss here.

The double polarized cross section is a product of the electron and hadron tensors. The electron tensor can be calculated directly from the first principles of QED. The hadron tensor, on the other hand, cannot be calculated directly, because of our lack of knowledge about strong interactions. But a general form of the hadron tensor can be constructed. The tensor has to be built from two available independent 4-vectors p^ν and q^ν and has to have only terms obeying necessary symmetries, one being time reversal invariance. Four such terms can be constructed with arbitrary scalar coefficients in front of them. These coefficients are called structure functions and are functions of the available independent scalars in the problem. Out of two independent 4-vectors p^ν and q^ν we can construct only two independent scalars: q^2 and $p^\nu q_\nu = M_n\omega$, since $p^2 = M_n$ is just a well known constant. By convention, we choose Q^2 and ω as independent variables so that the four structure functions are functions of them: $F_1(\omega, Q^2), F_2(\omega, Q^2), G_1(\omega, Q^2), G_2(\omega, Q^2)$. These four structure functions are independent. $G_1(\omega, Q^2), G_2(\omega, Q^2)$ describe polarized and $F_1(\omega, Q^2), F_2(\omega, Q^2)$ describe unpolarized degrees of freedom.

We adopt the convention of Raskin and Donnelly [5] and define nucleon polarization as longitudinal if the nucleon is polarized along the three-momentum q of the virtual photon in the lab-frame. Nucleon polarization is defined as sideways if it lies in the scattering plane and is perpendicular to the three-momentum q of the virtual photon.

Subtracting cross sections for the positive and negative electron helicities [5]:

$$\left[\frac{d\sigma_{-1/2}}{dE' d\Omega_e} - \frac{d\sigma_{+1/2}}{dE' d\Omega_e}\right] = \frac{2\alpha^2}{MQ^4}\frac{E'}{E} L^A_{\mu\nu} W^{\mu\nu}_A, \tag{1.9}$$

where $L^A_{\mu\nu}$ and $W^{\mu\nu}_A$ are the antisymmetric parts of the leptonic and hadronic tensors.

$$L^A_{\mu\nu} = -2i\epsilon_{\mu\nu\alpha\beta} k^\alpha (k - k')^\beta, \tag{1.10}$$

where k, k' are the initial and the final electron momenta. The general form of the hadronic tensor is

$$W^{\mu\nu}_A = -\frac{i}{M}\epsilon^{\mu\nu\rho\sigma}(p - p')_\rho s_\sigma G_1(\omega, Q^2) - \frac{i}{M}\epsilon^{\mu\nu\rho\sigma}(p - p')_\rho (M\omega s_\sigma - ((ps) - (p's))p_\sigma) G_2(\omega, Q^2), \tag{1.11}$$

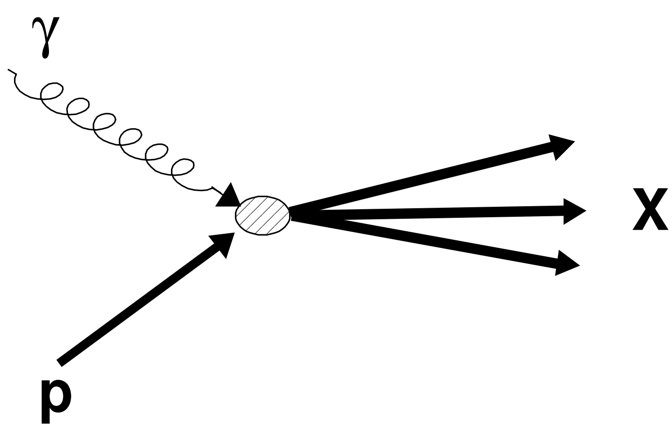

Figure 1-3: Virtual photo-absorption.

where p and p' are the initial and the final nucleon momenta. M and s are nucleon mass and spin.

Subtracting cross sections for the positive and negative electron helicities with the nucleon spin along the direction of the virtual photon and perpendicular to it:

$$\left[\frac{d\sigma_{-1/2}}{dE'd\Omega_e} - \frac{d\sigma_{+1/2}}{dE'd\Omega_e}\right]_{long} = \frac{4\alpha^2}{M^3Q^2}\frac{E'}{E}\frac{E+E'}{\sqrt{\omega^2+Q^2}}[M\omega G_1(\omega,Q^2) - Q^2G_2(\omega,Q^2)], \tag{1.12}$$

$$\left[\frac{d\sigma_{-1/2}}{dE'd\Omega_e} - \frac{d\sigma_{+1/2}}{dE'd\Omega_e}\right]_{side} = \frac{8\alpha^2}{M^3Q^2}\frac{E'}{E}\frac{EE'sin\Theta_e}{\sqrt{\omega^2+Q^2}}[MG_1(\omega,Q^2) + \omega G_2(\omega,Q^2)]. \tag{1.13}$$

1.3.2 Virtual Photo-absorption

In this and following sections we use conventions adopted in the Ph.D. Thesis of R. Pantforder [44]. We can express the inclusive electro-production cross section in terms of the cross section of the absorption of virtual photons (Fig. 1-3). The latter is defined through analogy with real photo-absorption

$$\sigma(\omega, Q^2) = \frac{4\pi^2\alpha}{MK}\epsilon^{*\mu}\epsilon^{\nu}W_{\mu\nu}, \tag{1.14}$$

where

$$K = \sqrt{\omega^2 + Q^2}. \tag{1.15}$$

$W_{\mu\nu}$ is a tensor of the nucleon [5]:

$$W^{\mu\nu} = \frac{1}{4\pi}\int d^4x e^{iqx} < p, s|[J^{\mu}(x), J^{\nu}(0)]|p, s >, \tag{1.16}$$

where s,p are the nucleon spin and momentum. $J(x)$ is the nucleon current at space point x.

We describe virtual photon polarization in the lab-frame. The first axis e_1 is in the electron scattering plane and is perpendicular to the direction of the virtual photon. The third axis e_3 is along the direction of the virtual photon. The second axis is constructed to make (e_1,e_2,e_3) a right-handed orthogonal coordinate system (Fig. 1-4). A four-dimensional polarization vector has the form:

$$\epsilon^{\nu} = (\epsilon_0, \epsilon_x, \epsilon_y, \epsilon_z) = \epsilon_0 e_0 + \epsilon_x e_1 + \epsilon_y e_2 + \epsilon_z e_3, \tag{1.17}$$

where (e_1,e_2,e_3) is a right-handed orthogonal coordinate system introduced in the beginning of the section and e_0 is a unit vector in the time direction. A virtual photon linearly polarized along e_1 axis has polarization vector

$$\epsilon^{\nu}_{\parallel} = (0, 1, 0, 0). \tag{1.18}$$

Virtual photon linearly polarized along e_2 axis has polarization vector

$$\epsilon^{\nu}_{\perp} = (0, 0, 1, 0). \tag{1.19}$$

Subscripts $\|, \perp$ show that the first polarization is coplanar with the scattering plane and the second is perpendicular to it.

Two circular polarizations can be constructed from these linear polarizations, left-handed

$$\epsilon_{-}^{\nu} = \frac{1}{\sqrt{2}}(0, 1, -i, 0), \tag{1.20}$$

and right-handed

$$\epsilon_{+}^{\nu} = \frac{1}{\sqrt{2}}(0, -1, -i, 0). \tag{1.21}$$

These polarizations are transverse to the direction of the virtual-photons and have the same analogue as for real photons. A distinctive property of the virtual photons is the ability to have longitudinal polarization

$$\epsilon_{0}^{\nu} = (\sqrt{\frac{\omega^2}{Q^2} + 1}, 0, 0, \frac{\omega}{Q}). \tag{1.22}$$

Consider scattering of the transversely polarized virtual photon with a longitudinally polarized nucleon. Define the cross section as

$$\sigma_{1/2}^{T}(\omega, Q^2) = \frac{4\pi^2\alpha}{M\sqrt{\omega^2 + Q^2}}[\epsilon_{-}^{*\mu}\epsilon_{-}^{\nu}]W_{\mu\nu}^{long}, \tag{1.23}$$

$$\sigma_{3/2}^{T}(\omega, Q^2) = \frac{4\pi^2\alpha}{M\sqrt{\omega^2 + Q^2}}[\epsilon_{+}^{*\mu}\epsilon_{+}^{\nu}]W_{\mu\nu}^{long}. \tag{1.24}$$

where 1/2 and 3/2 are the total helicities of the photon-nucleon system in its center of mass frame. $W_{\mu\nu}^{long}$ is a tensor of the nucleon polarized longitudinally (along the momentum of the virtual photon) (Eq. 1.11) [44], [5]. The vector product $[\epsilon_{-}^{*\mu}\epsilon_{-}^{\nu}]$ corresponds to a left-handed photon and vector product $[\epsilon_{+}^{*\mu}\epsilon_{+}^{\nu}]$ to a right-handed photon. Thus $\sigma_{1/2}^{T}(\omega, Q^2)$ and $\sigma_{3/2}^{T}(\omega, Q^2)$ are the cross sections for the interaction of a longitudinally polarized nucleon with left-handed and right-handed photons re-

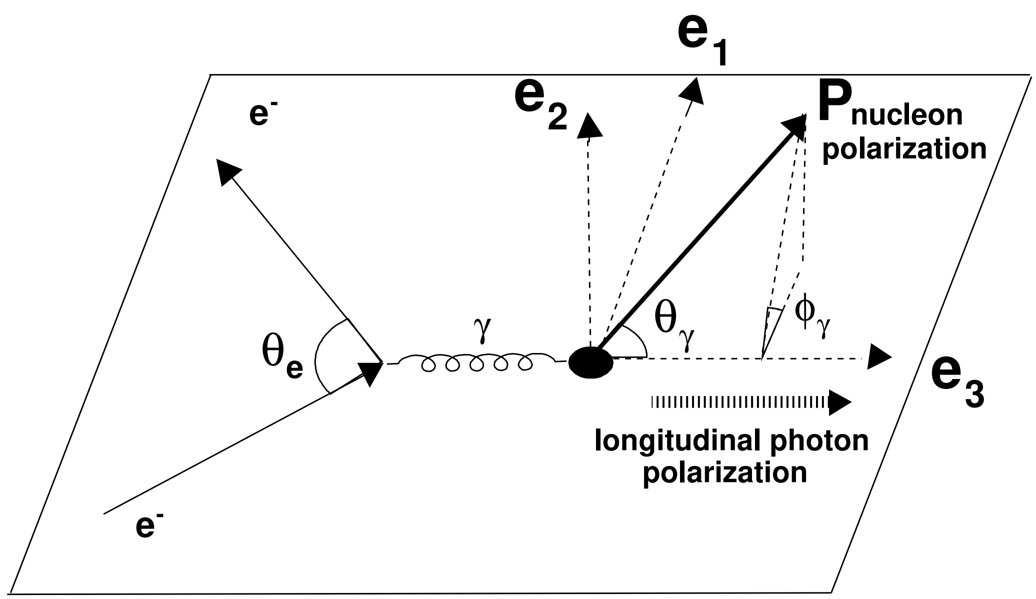

Figure 1-4: Polarized electron scattering from a polarized nucleon. Axis e_1 is in the electron scattering plane and is perpendicular to the direction of the virtual photon. Axis e_3 is along the direction of the virtual photon.

spectively.

Consider a transversely polarized nucleon and the interference of a longitudinal and a transverse (linearly polarized) photon. Define the cross section

$$\sigma_{LT}(\omega, Q^2) = \frac{4\pi^2\alpha}{M\sqrt{\omega^2 + Q^2}} Im[\epsilon_0^{*\mu}\epsilon_\perp^\nu]W_{\mu\nu}^{side}. \tag{1.25}$$

$W_{\mu\nu}^{side}$ is the tensor of the nucleon polarized sideways, where "sideways" means that nucleon polarization lies in the electron scattering plane and is perpendicular to the three-momentum q of the virtual photon as defined in the previous section.

Now comparing Equations (1.23-1.25) with the expressions for electro-production (1.9-1.13), we can identify

$$\sigma_{1/2}^T(\omega, Q^2) - \sigma_{3/2}^T(\omega, Q^2) = \frac{8\pi^2\alpha}{M^2}\frac{\omega}{\sqrt{\omega^2 + Q^2}}\left[G_1(\omega, Q^2) - \frac{Q^2}{M\omega}G_2(\omega, Q^2)\right], \tag{1.26}$$

$$\sigma_{LT}(\omega, Q^2) = \frac{4\pi^2\alpha}{M^2}\frac{Q}{\sqrt{\omega^2+Q^2}}\left[G_1(\omega, Q^2) + \frac{\omega}{M}G_2(\omega, Q^2)\right]. \tag{1.27}$$

Substituting the spin structure functions with the virtual photon photo-absorption cross sections

$$\left[\frac{d\sigma_{-1/2}}{dE'd\Omega_e} - \frac{d\sigma_{+1/2}}{dE'd\Omega_e}\right]_{long} = \Gamma\sqrt{1-\epsilon^2}(\sigma^T_{1/2}(\omega, Q^2) - \sigma^T_{3/2}(\omega, Q^2)), \tag{1.28}$$

$$\left[\frac{d\sigma_{-1/2}}{dE'd\Omega_e} - \frac{d\sigma_{+1/2}}{dE'd\Omega_e}\right]_{side} = 2\Gamma\sqrt{2\epsilon(1-\epsilon)}\sigma_{LT}(\omega, Q^2), \tag{1.29}$$

where

$$\Gamma = \frac{\alpha}{2\pi^2}\frac{E'}{E}\frac{\sqrt{\omega^2+Q^2}}{Q^2}\frac{1}{1-\epsilon} \tag{1.30}$$

is the virtual photon flux per electron, and

$$\epsilon = \left[1 + 2\left(1 + \frac{\omega^2}{Q^2}\right) tan^2\frac{\Theta_e}{2}\right]^{-1} \tag{1.31}$$

is a polarization parameter of the virtual photon. Subscripts "long" and "side" denote longitudinal and sideways nucleon polarization as defined at the end of the previous section.

Instead of the $G_1(\omega, Q^2)$ and $G_2(\omega, Q^2)$, slightly different functions can be used

$$g_1(x, Q^2) = \frac{\omega}{M}G_1(\omega, Q^2), \tag{1.32}$$

$$g_2(x, Q^2) = \frac{\omega^2}{M^2}G_2(\omega, Q^2), \tag{1.33}$$

where Bjorken x is $\frac{Q^2}{2M\omega}$. In the Deep Inelastic Scattering regime we have scaling: $g_i(x, Q^2) \rightarrow g_i(x)$ where the limit $Q^2 \rightarrow \infty$ is taken in such a way that x is constant.

1.3.3 Polarized and Unpolarized Inclusive Electron Cross Section

The inclusive unpolarized electron cross section can be written in terms of unpolarized structure functions $F_1(x,Q^2)$ and $F_2(x,Q^2)$ [42]:

$$\frac{d\sigma}{d\Omega dQ^2} = \frac{4\pi\alpha^2(\hbar c)^2 E' cos^2(\frac{\Theta}{2})}{Q^4 E}\left(\frac{1}{\omega}F_2(x,Q^2) + 2tan^2(\frac{\Theta}{2})\frac{1}{M}F_1(x,Q^2)\right). \quad (1.34)$$

This cross section can also be written as the sum of a transverse photon part and a longitudinal photon part [42]:

$$\frac{d\sigma}{d\Omega dE'} = \Gamma(\sigma_T(\gamma*) + \epsilon\sigma_L(\gamma*)) \quad (1.35)$$

where the photon flux Γ is defined in Eq. (1.30).

The ratio of longitudinal to transverse cross section is usually denoted as R

$$R = \frac{\sigma_L}{\sigma_T}. \quad (1.36)$$

The cross section difference for the electron scattering experiment can be written in the form

$$\frac{d\sigma^{\downarrow\uparrow}}{d\Omega dE'} - \frac{d\sigma^{\uparrow\uparrow}}{d\Omega dE'} = \frac{16\alpha^2(\hbar c)^2 E'^2 sin^2(\frac{\Theta}{2})}{Q^4}\left(\frac{E + E' cos\Theta}{M\omega}g_1(x,Q^2) - \frac{1}{\tau M}g_2(x,Q^2)\right)P_t P_b, \quad (1.37)$$

where $\sigma^{\uparrow\uparrow}(\sigma^{\downarrow\uparrow})$ is the cross section for the electron beam and nucleon polarized in the same (opposite) directions along the beam. P_t and P_b are the polarizations of the target and the beam respectively, $\tau = \frac{\omega^2}{Q^2}$ [42], [5].

Instead of the spin structure functions $g_1(x,Q^2)$ and $g_2(x,Q^2)$ electron asymmetries A_1 and A_2 can be used [42], [5]:

$$g_1(x,Q^2) = \frac{\tau}{1+\tau}(A_1(x,Q^2) + \frac{1}{\sqrt{\tau}}A_2(x,Q^2))F_1(x,Q^2), \quad (1.38)$$

$$g_2(x,Q^2) = \frac{\tau}{1+\tau}(\sqrt{\tau}A_2(x,Q^2) - A_1(x,Q^2))F_1(x,Q^2). \quad (1.39)$$

1.4 The GDH Sum Rule for Real Photons

The Gerasimov sum rule connects the nucleon photo-absorption cross section with global properties of the nucleon. It was derived by Gerasimov and published in the 1965 issue of *Yadernaya Fizika* and April 1966 issue of *Soviet Journal of Nuclear Physics.* After that a number of people independently re-derived it. Hosoda and Yamamoto published a paper in *Progress of Theoretical Physics* in May of 1966. Drell and Hearn published a paper in *Physics Review Letters* also in May 1966. The approach of Hosoda and Yamamoto was different from that of Gerasimov and used current algebra. There are a number of different naming conventions for the Gerasimov sum rule: GDH, DH, DHG. We adopt the often-used convention GDH (Gerasimov-Drell-Hearn).

The Gerasimov sum rule connects static properties of the nucleon with the integral that runs over all energies:

$$\int_{\omega_0}^{\infty} \frac{(\sigma_{\frac{1}{2}}(\omega') - \sigma_{\frac{3}{2}}(\omega'))d\omega'}{\omega'} = -\frac{2\pi^2\alpha\mu_a^2}{M^2}, \quad (1.40)$$

where μ_a, M are the anomalous magnetic moment and the mass of the nucleon. ω_0 is the energy threshold for pion-production. $\sigma_{\frac{1}{2}}(\omega)$ and $\sigma_{\frac{3}{2}}(\omega)$ are the photo-absorption cross sections for the total helicity of the photon-nucleon system in the center of mass system being $\frac{3}{2}$ and $\frac{1}{2}$ respectively. The integral runs over photon energies starting from pion threshold up to infinity.

The integral on the left side of the above equation is called the GDH integral. The GDH integral can be naturally extended to the domain of virtual photons and can be studied with the help of inclusive electro-production reactions. To understand the weak points of this formalism for virtual photons we have to start our discussion with the case of real photons and the real-photon GDH sum rule.

For the sake of understanding the limitations of and possible ways of breaking the

GDH sum rule, we examine its derivation in Appendix A. We generalize the integral on the left of the above equation to the domain of electro-production and virtual photons, and we examine its limit when Q^2 goes to infinity.

1.5 Generalized GDH Integral

The integral in the GDH sum rule can be naturally generalized to virtual photons with 4-momentum $q^2 = -Q^2$ not equal to zero:

$$I_{GDH_a}(Q^2) = \int_{\omega_0}^{\infty} \frac{(\sigma^T_{\frac{1}{2}}(\omega, Q^2) - \sigma^T_{\frac{3}{2}}(\omega, Q^2))d\omega}{\omega}. \tag{1.41}$$

This generalized integral has the correct limit as $Q^2 \to 0$:

$$\lim_{Q^2 \to 0} I_{GDH_a}(Q^2) = I^{realphoton}_{GDH}. \tag{1.42}$$

We can rewrite the above integral in terms of the structure functions G_i or g_i using the results of Section 1.3.2 :

$$\begin{aligned} I_{GDH_a}(Q^2) &= \int_{\omega_0}^{\infty} \frac{(\sigma^T_{\frac{1}{2}}(\omega, Q^2) - \sigma^T_{\frac{3}{2}}(\omega, Q^2))d\omega}{\omega} \\ &= \frac{8\pi^2\alpha}{M^2} \int_{\omega_0}^{\infty} \frac{(G_1(\omega, Q^2) - \frac{Q^2}{M\omega} G_2(\omega, Q^2))d\omega}{\omega^2 + Q^2} \\ &= \frac{16\pi^2\alpha}{Q^2} \int_0^{x_0} \frac{(g_1(x, Q^2) - \frac{4M^2x^2}{Q^2} g_2(x, Q^2))dx}{\sqrt{1 + \frac{4M^2x^2}{Q^2}}}. \end{aligned} \tag{1.43}$$

In the last equation, we changed the variable of integration from photon energy ω to Bjorken $x = \frac{Q^2}{2M\omega}$. The respective threshold is changed from ω_0 to $x_0 = \frac{Q^2}{2M\omega_0}$.

The DIS limit of the last integral ($Q^2 \to \infty, x = const$) will be

$$I_{GDH_a}(Q^2) \to \frac{16\pi^2\alpha}{Q^2} \int_0^{x_0} g_1(x, Q^2)dx, \tag{1.44}$$

since in this limit the factor $\frac{x^2}{Q^2} \to 0$. We also can take a look at the upper limit of integration x_0:

$$x_0 = \frac{Q^2}{2M\omega_0} = \frac{Q^2}{2Mm_\pi + m_\pi^2 + Q^2}, \tag{1.45}$$

$$\lim_{Q^2\to\infty} x_0(Q^2) = 1. \tag{1.46}$$

Now we consider the relationship between the two integrals:

$$\lim_{Q^2\to\infty} \int_0^{x_0} g_1(x,Q^2)dx, \tag{1.47}$$

and

$$\int_0^1 g_1(x,Q^2)dx. \tag{1.48}$$

g_1 has elastic scattering as a delta function at $x = 1$. The second integral includes this delta function while the first integral does not, even having $x_0 \to 1$. However, the contribution of the elastic scattering to the total amplitude is negligible in the DIS regime. This allows us to conclude that the above two integrals are equal.

$$\lim_{Q^2\to\infty} \int_0^{x_0} g_1(x,Q^2)dx = \int_0^1 g_1(x,Q^2)dx. \tag{1.49}$$

The detailed analysis of this subject can be found in a paper by X.Ji [52].

Finally we have found the DIS limit of the generalized GDH integral

$$\lim_{Q^2\to\infty} I_{GDH_a}(Q^2) = \frac{16\pi^2\alpha}{Q^2}\int_0^1 g_1(x,Q^2)dx. \tag{1.50}$$

1.6 Bjorken Sum Rule

Let us introduce the integral

$$\Gamma(Q^2) = \int_0^1 g_1(x,Q^2)dx. \tag{1.51}$$

This integral often referred to as the first moment of $g_1(x, Q^2)$. Consider Deep Inelastic Scattering and the scaling limit $g_i(x, Q^2) \to g_i(x)$ as $Q^2 \to \infty$:

$$\Gamma(Q^2) \to I_1' = \int_0^1 g_1(x)dx. \tag{1.52}$$

It was shown by Bjorken [4] that a difference of the integrals I_1' for the proton and the neutron is related to the neutron beta-decay constant.

$$I'^p_1 - I'^n_1 = \frac{g_A}{6}, \tag{1.53}$$

where $g_A = 1.26$ is the neutron beta-decay constant.

$\Gamma(Q^2)$ has a form similar to the GDH integral.

$$\lim_{Q^2 \to \infty} I_{GDH_a}(Q^2) = \frac{16\pi^2\alpha}{Q^2}\Gamma(Q^2). \tag{1.54}$$

Thus an important limit of the GDH integral can be established:

$$\lim_{Q^2 \to \infty} (I^p_{GDH_a}(Q^2) - I^n_{GDH_a}(Q^2)) = \frac{16\pi^2\alpha}{Q^2}\frac{g_A}{6}. \tag{1.55}$$

Together with the photon limit $Q^2 = 0$, the Bjorken sum rule provides important information about the behavior of the GDH integral. Unfortunately, the behavior at the intermediate Q^2 is much less understood.

1.7 Different Generalizations of the GDH Integral

The generalized GDH integral introduced in the previous sections has two properties of interest. It reduces to the GDH integral for real photons at $Q^2 = 0$ and it provides an easy connection with the Bjorken sum rule at high Q^2. It can be shown that the construction of the GDH integral with such properties is actually not unique.

Consider the integral

$$
\begin{aligned}
I_{GDH_b}(Q^2) &= \int_{\omega_0}^{\infty} \frac{\sqrt{\omega^2+Q^2}}{\omega} \frac{(\sigma^T_{\frac{1}{2}}(\omega,Q^2)-\sigma^T_{\frac{3}{2}}(\omega,Q^2))d\omega}{\omega} \\
&= \frac{16\pi^2\alpha}{Q^2}\int_0^{x_0} dx \left(g_1(x,Q^2) - \frac{4M^2x^2}{Q^2} g_2(x,Q^2) \right).
\end{aligned} \tag{1.56}
$$

The factor $\frac{\sqrt{\omega^2+Q^2}}{\omega}$ is equal to 1 for real photons. This proves that $I_{GDH_b}(0) = I_{GDH_a}(0)$. The factor with $\frac{x^2}{Q^2} \to 0$ if $Q^2 \to \infty$, proving that $I_{GDH_b}(\infty) = I_{GDH_a}(\infty)$. We can also consider the integral

$$
\begin{aligned}
I_{GDH_c}(Q^2) &= \int_{\omega_0}^{\infty} \frac{\sqrt{\omega^2+Q^2}}{\omega} \frac{((\sigma_{\frac{1}{2}}(\omega',Q^2)-\sigma_{\frac{3}{2}}(\omega',Q^2)) + \sigma_{LT}(\omega',Q^2)\frac{2Q}{\omega'})d\omega'}{\omega'} \\
&= \frac{16\pi^2\alpha}{Q^2}\int_0^{x_0} g_1(x,Q^2)dx.
\end{aligned} \tag{1.57}
$$

All three integrals are possible ways of generalizing the original GDH integral, since

$$
I_{GDH_a}(0) = I_{GDH_b}(0) = I_{GDH_c}(0), \tag{1.58}
$$

$$
I_{GDH_a}(\infty) = I_{GDH_b}(\infty) = I_{GDH_c}(\infty). \tag{1.59}
$$

Many other integrals that satisfy the above properties can be constructed. This makes it important to specify the particular definition that is used in the discussion of the GDH integral. These integrals can differ substantially in the region of intermediate Q^2.

The choice of the generalized integral is dictated by different factors. From the experimentalist's point of view, two factors are most important. First is the relationship of the quantities under the integral to the quantities directly measured in the experiment. In the electro-production experiment we never directly measure g_1 or g_2, but rather combinations of them. The same is true for $(\sigma_{\frac{1}{2}}(\omega',Q^2) - \sigma_{\frac{3}{2}}(\omega',Q^2))$ and $\sigma_{LT}(\omega',Q^2)$. We only measure linear combination of them. Unfortunately, neither combination is the same as that in the GDH integrals. None of the GDH integrals considered above provides an advantage in this respect.

The other important factor is the other data with which the results of the present experiment will be compared. Since practically all the data in the intermediate Q^2 region come from SLAC experiments [7] we will adopt their convention, and use the third definition (1.57) of the GDH integral, $I_{GDH}(Q^2) \equiv I_{GDH_c}(Q^2)$.

1.8 Existing Data

The most interesting Q^2 region is the region where the GDH integral is predicted to dramatically change its behavior and go from a negative quantity to a positive one (Fig. 1-5, 1-6). The nucleon spin structure functions have been studied via deep-inelastic lepton scattering [62], [54], [55], [10]; however, data are practically non-existent in the resonance region.

The two most important measurements of the generalized GDH integral have been done at DESY by the HERMES collaboration [56], [57], [58] and at SLAC by the E143 collaboration [7].

1.8.1 HERMES Measurement

The experiment was conducted in 1997 [56], [57], [58]. The measurement was done using an incident positron beam and a hydrogen target internal to the HERA storage ring. A beam of longitudinally polarized positrons of $28GeV$ had an average polarization of 0.6. A longitudinally polarized hydrogen gas target had a polarization of about 0.9. The GDH integral was measured in the range $1.2GeV^2 < Q^2 < 12GeV^2$. Figure 1-5 shows that only two HERMES points are below $Q^2 = 2.5GeV^2$, one at $Q^2 = 1.5GeV^2$ and the other at $Q^2 = 2GeV^2$. The data was taken in the W^2 range $1GeV^2 < W^2 < 45GeV^2$. The unmeasured contribution to the GDH integral for $W^2 > 45GeV^2$ was calculated using a multiple-Reggeon exchange parameterization [59]. Analysis shows that the contribution of the resonance region ($W^2 < 4.2GeV^2$) to the full GDH integral is small for Q^2 values above 3 GeV^2 but becomes very important for $Q^2 < 2GeV$

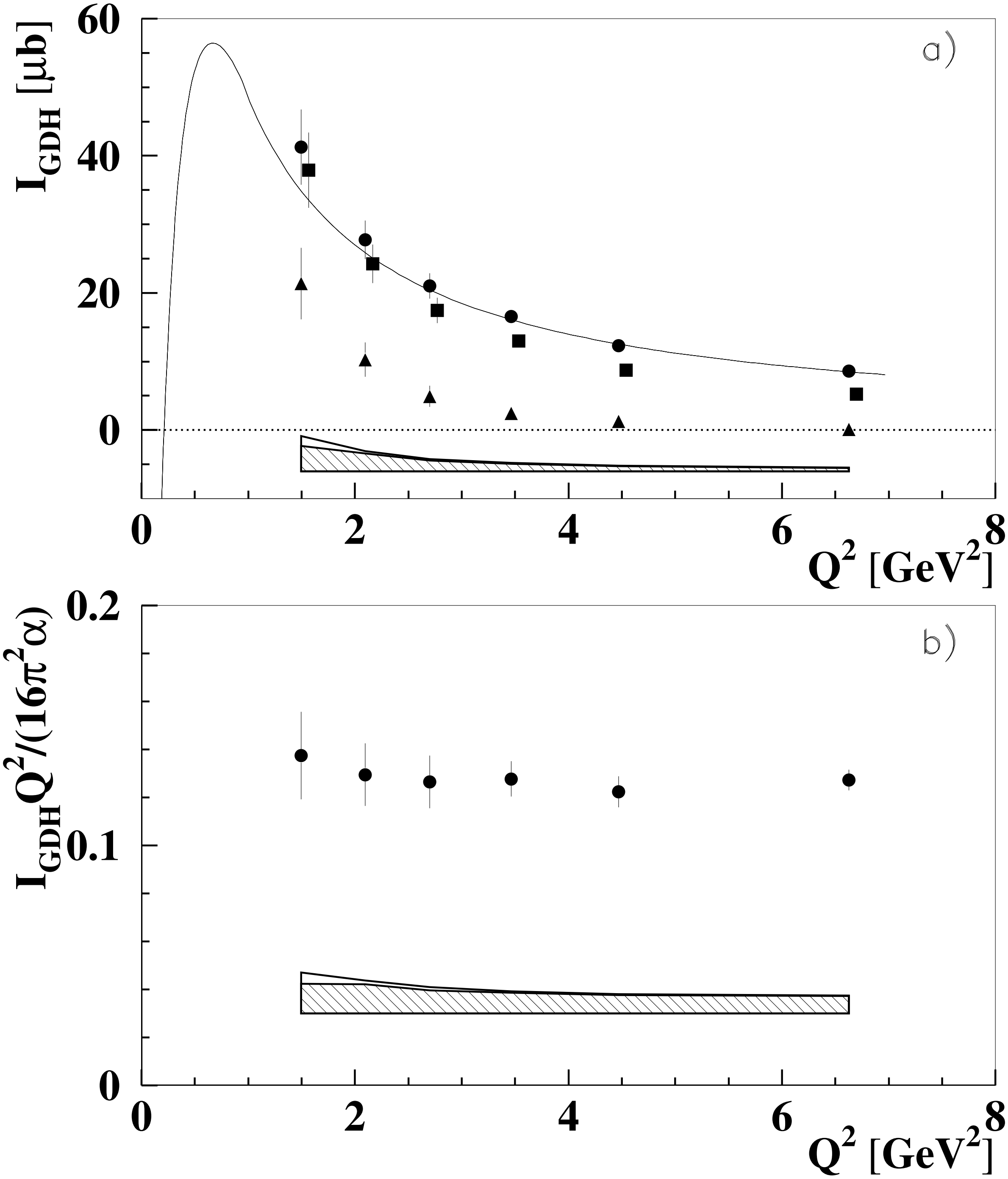

Figure 1-5: HERMES data [56] a) I_{GDH} integral as a function of Q^2 for various upper limits of integration: $W^2 < 4.2GeV^2$ (triangles), $W^2 < 45GeV^2$ (squares), and the total integral I_{GDH} (circles). The squares have been slightly shifted to make them more visible. The curve is the Soffer-Teryaev model [28] for the total integral. b) $I_{GDH}Q^2/16\pi^2\alpha$ as a function of Q^2.

1.8.2 SLAC Measurement

The E143 collaboration has measured the proton structure function g_1^p in the region of the nucleon resonances for $W^2 < 5GeV^2$ and $Q^2 = 0.5$ and $Q^2 = 1.2GeV^2$ [8], [7]. A polarized electron beam with energy 9.7 GeV and a polarized cryogenic NH_3 target were used for the experiment. The average polarizations of the beam and the target were 0.85 and 0.65 respectively. Data were taken with longitudinal target polarization only. As an assumption, the A_2 asymmetry was set to zero. The error introduced by this assumption was estimated to be small compared to the statistical errors. The integral over g_1 was taken from pion threshold up to $W^2 = 4GeV^2$. The contribution from $W^2 > 4$ was calculated on the basis of the fit to the world's deep-inelastic g_1 data [8]. The results are shown in Figure 1-6. The experiment demonstrated the important evolution of the GDH integral in the resonance region but lacked the ability to reach the region of the small values of Q^2 where the integral has to change sign.

1.8.3 Mainz Measurement

The very first measurement of the GDH integral for real photons was carried out at MAMI (Mainz) [63]. The photon energy range covered by experiment was $200 < E_\gamma < 800MeV$ (Fig. 1-7). The measured contribution to the GDH sum rule from this region was found to be $-226 \pm 5(stat) \pm 12(sys)\mu b$. Using a model for the unmeasured part of the GDH integral the total GDH sum was estimated to be $210\mu b$. This value is within experimental error of the GDH sum rule $205\mu b$ (Eq. A.1). An experiment is underway at ELSA (Bonn) with photon energy from $E_\gamma = 0.7GeV$ up to $E_\gamma = 3GeV$. It should complement the Mainz measurement.

1.9 Summary

The study of the strong interactions at intermediate values of Q^2 is important because experimentally this is the least understood region. We have stressed the importance of tools that can be applicable to a broad range of Q^2, such as the generalized GDH

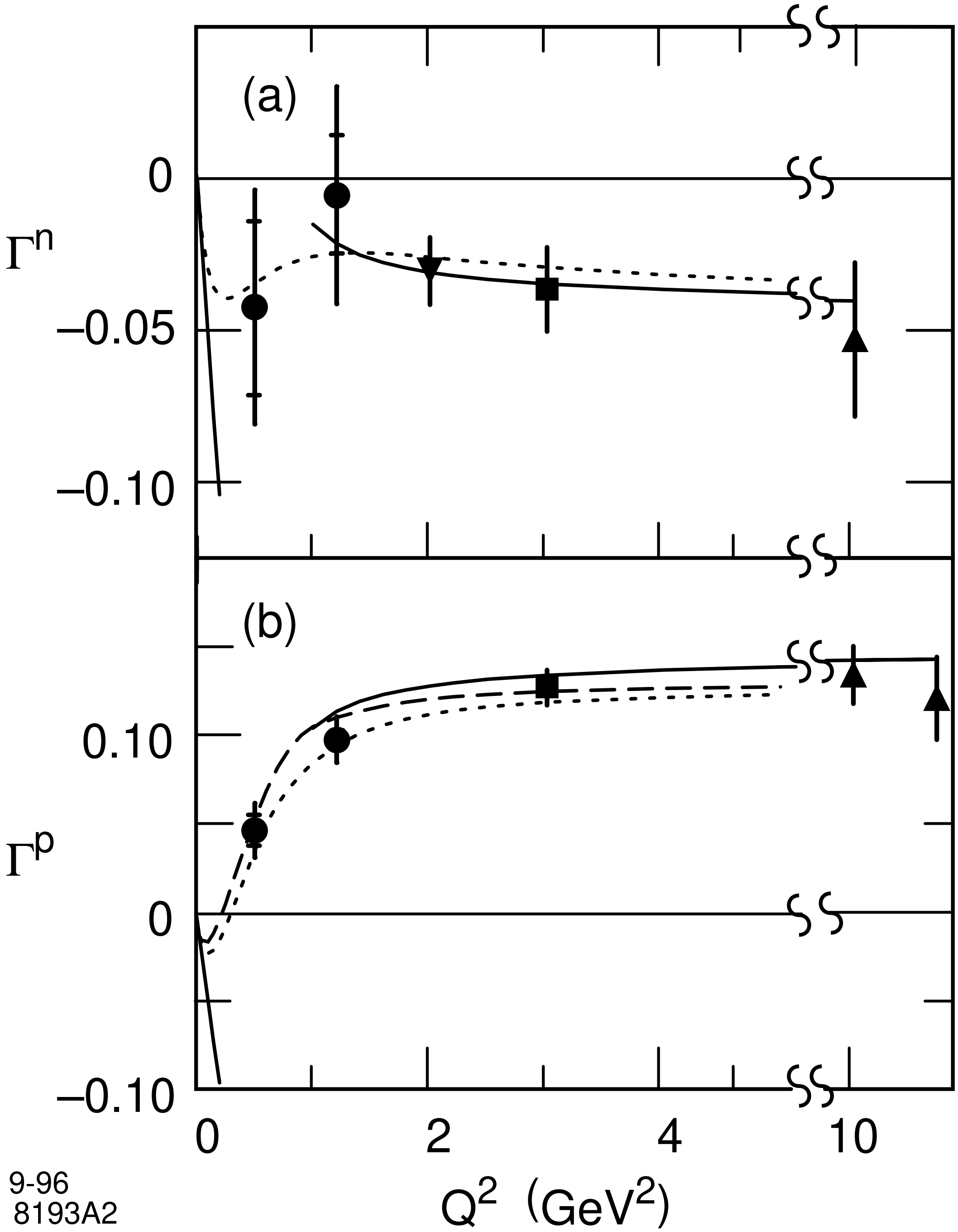

Figure 1-6: SLAC data [7]. Integrals of g_1 at several fixed values of Q^2 for (a) the neutron and (b) the proton. E143 data (circles) are plotted together with data from CERN [60] (triangles), E143 deep-inelastic [8] (squares), and E142 [10] (inverted triangle). The curves correspond to the evolution[61] of the deep-inelastic results due to changing α_s (solid line), the predictions of Burkert and Ioffe [33] (dotted line), the model of Soffer [29] (dashed line), and the GDH approach to $Q^2 = 0$ (solid line).

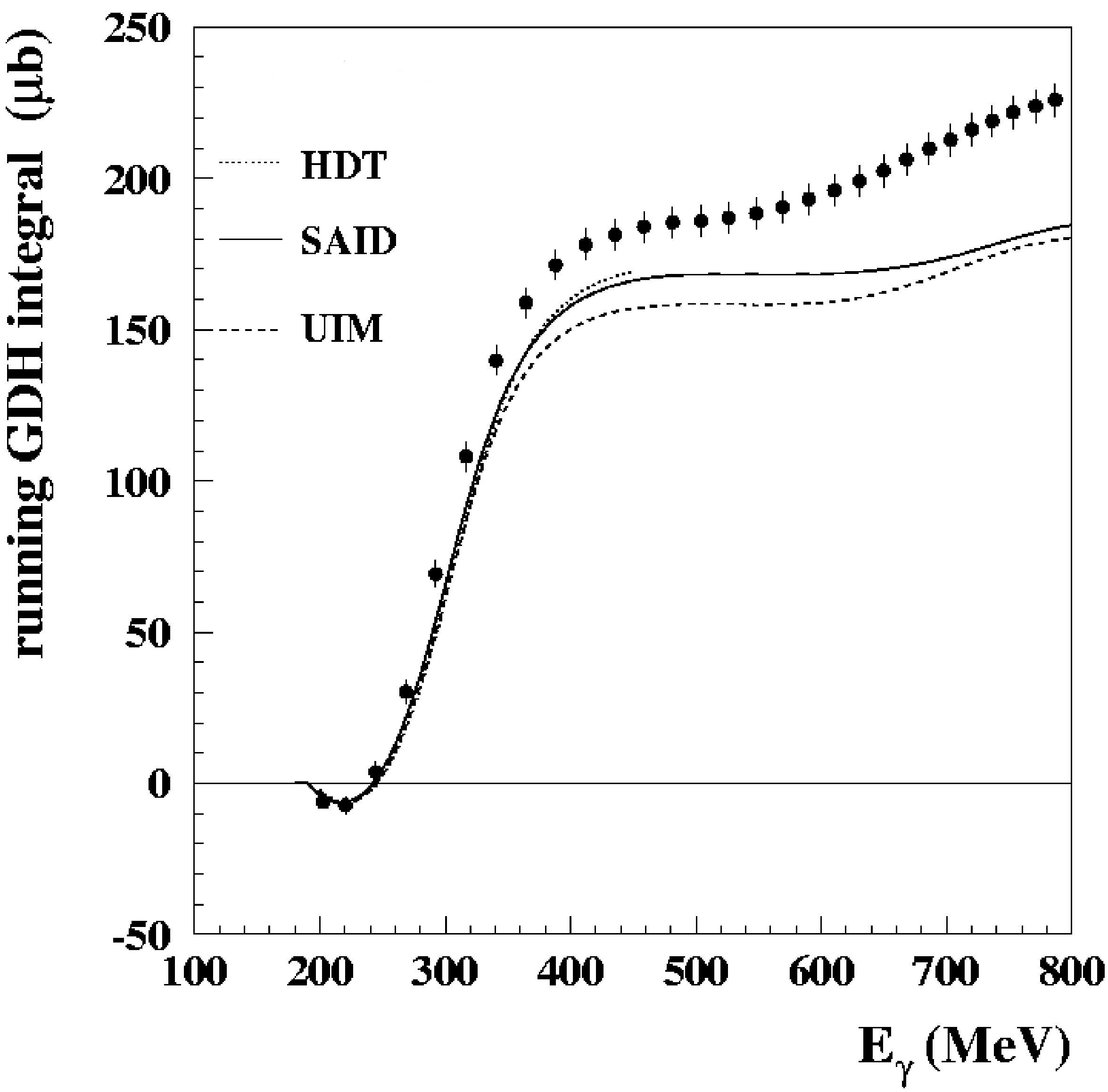

Figure 1-7: The running GDH integral ($Q^2 = 0$) obtained at Mainz [63] starting at 200 MeV is compared to the model predictions HDT [64], SAID [65], UIM [66]. Only statistical errors are shown. The integration starts at $E_\gamma = 200$ MeV and the upper integration limit is taken as the running variable.

integral.

We have presented a derivation of the GDH sum rule for real photons with $Q^2 = 0$ and showed the fundamental nature of this quantity (Appendix A). The energy weighted integral of the difference $\sigma_{\frac{1}{2}}(\omega') - \sigma_{\frac{3}{2}}(\omega')$ of the nucleon's polarized total photo-absorption cross sections is related to the nucleon's anomalous magnetic moment:

$$\int_{\omega_0}^{\infty} \frac{(\sigma_{\frac{1}{2}}(\omega') - \sigma_{\frac{3}{2}}(\omega'))d\omega'}{\omega'} = -\frac{2\pi^2\alpha\mu_a^2}{M^2}. \tag{1.60}$$

The GDH sum rule is based on the general principles of causality and gauge invariance of the electromagnetic interaction. The only real assumption is the assumption of the convergence of the GDH integral which depends solely on the asymptotic behavior of the cross section difference $(\sigma_{\frac{1}{2}}(\omega') - \sigma_{\frac{3}{2}}(\omega'))$ at high ω. We also showed that the GDH sum rule is a statement to first order in the electromagnetic coupling constant α. The treatment of the possible modifications of the Gerasimov-Drell-Hearn Sum Rule can be found in the Ph.D. thesis of R. Pantforder [44].

The GDH integral can be generalized to include virtual photons with $Q^2 > 0$ and we made a connection between electro-production and virtual photo-absorption.

We established a link between the generalized GDH integral and the Bjorken sum rule:

$$\lim_{Q^2 \to \infty} (I_{GDH}^p(Q^2) - I_{GDH}^n(Q^2)) = \frac{16\pi^2\alpha}{Q^2}\frac{g_A}{6}. \tag{1.61}$$

Generalization of the GDH integral to $Q^2 \neq 0$ is not a unique procedure and we discussed several choices, such as $I_{GDH_a}(Q^2)$, $I_{GDH_b}(Q^2)$ and $I_{GDH_c}(Q^2)$ (Eq. 1.57).

At the end we showed that the spectrum of the theoretical efforts in this field is a broad one and that the experimental task of measuring the Q^2 evolution of the GDH sum rule is a challenging one.

Chapter 2

Experimental Setup

2.1 Thomas Jefferson National Accelerator Facility

The Thomas Jefferson National Accelerator Facility (JLab) is located in the city of Newport News, Virginia. The laboratory has an electron accelerator with energy up to almost $6 GeV$. The accelerator design uses superconducting radio-frequency technology to accelerate electrons. The $45 MeV$ injector linac delivers unpolarized electrons from a conventional thermionic gun or polarized electrons from a laser-driven photocathode source. Electrons are generated continuously with a $1.497 GHz$ microbunch beam structure. Two anti-parallel superconducting linacs of $\sim 550 MeV$, connected in a "racetrack" configuration by recirculation arcs, accelerate the electrons in five passes to a final energy of $4 GeV$. Each linac consists of twenty cryomodules, and each cryomodule contains four pairs of five-cell, $1497 MHz$ niobium accelerating cavities. Cavities cooled to $2K$ by a superfluid helium plant accelerate electrons along the linear accelerator section in a continuous wave mode. The maximum field gradient produced by the cavities is about 5 MeV per meter. The energy spread of the beam is $\Delta E/E < 10^{-4}$.

The second recirculation arc of the accelerator uses RF separators as extraction elements. The design provides the capability of delivering three simultaneous $499 MHz$, cw electron beams into three experimental areas (Hall A, B, C). The energies of the three beams are correlated as multiples of the energy gain per pass through the two linacs. The beams are structured in microbunches separated by approximately $2ns$. These micro-bunches can be loaded with different electron densities, providing the capability of delivering three beams of independent currents into the different halls.

The three experimental halls A, B and C have complementary physics programs. Hall A has two High Resolution Spectrometers(HRS), one for electron and the other for hadron detection. The spectrometers have a momentum range of $0.3 - 4.0\ GeV/c$ with a momentum acceptance of 4.5% and a momentum resolution of $\frac{\Delta p}{p} \simeq 3 * 10^{-4}$. The system covers a solid angle of about 5-7 msr and has a $0.3mr$ angle determination accuracy. The Hall-A program is oriented towards experiments that require high precision measurements.

Hall C, on the other hand, has the primary goal of studying high momentum final states. Its High Momentum Spectrometer (HMS) can detect particles with momenta from 0.5 to up to 7.5 GeV/c while its Short Orbit Spectrometer (SOS) has a momentum range of 0.1 to 1.8 GeV/c. Both Hall-C spectrometers have moderate momentum resolution$\frac{\Delta p}{p} = 10^{-3}$. The angular acceptance is about 6 msr for HMS and 9 msr for SOS. The angular measurement precision is in the range of 0.4 -0.9 mr.

Hall B is the home of the CEBAF Large Acceptance Spectrometer (CLAS). Near 4π acceptance of the detector makes it an ideal place to study exclusive multi-particle final states. It also allows simultaneous measurement of different channels in a broad range of kinematic variables.

2.2 CEBAF Large Acceptance Spectrometer (CLAS), Hall B

Hall B of Jefferson Laboratory hosts the CEBAF Large Acceptance Spectrometer(CLAS), which is almost a 4π detector. The experimental program is geared towards simultaneous measurement of different channels in broad ranges of momenta and angles for final state particles. The detector (see Figures 2-1, 2-2) is divided into 6 sectors making an “orange like” configuration with the beamline as its symmetry axis. Each sector essentially acts like an independent spectrometer. Six 5 meter long superconducting coils separate sectors and form an approximate toroidal magnetic field. The magnetic field generated by the coils has a maximum intensity of about 2 Tesla. It is oriented primarily in the azimuthal direction about the beam line.

The detection devices form different layers around a fixed target in the middle of the CLAS. The detector has three layers of Drift Chambers (DC). The first layer around the target is called Region 1, the second Region 2 etc. The magnetic coils are located in Region 2 and produce a magnetic field inside the Region 2 Drift Chambers. The DC system determines the trajectories of charged particles and allows us to measure particle momentum. A Cherenkov Counter (CC) and an Electromagnetic Calorimeter (EC) are located in the forward direction and are used for electron identification. The Scintillation Counters (SC) have a very large angle of coverage and are used for the Time-of-Flight (TOF) measurement of charged particles. The SC also have 5% efficiency for neutron detection and can be used for neutron detection at large angles while the EC identifies neutral particles such as neutrons and photons in the forward direction. The EC system coverage is extended by the Large Angle Calorimeters (LAC) to 80° in some sectors, but the LAC system is not used in our experiment.

To summarize the angle coverage of various detectors, we have to mention that the DC covers from 8° to 140° (polar angle), the TOF(SC) from 9° to 140°, and the EC and CC from 8° to 45°. Because of the important role that EC and CC play in the electron identification, electron detection is possible only at forward angles. The azimuthal coverage of the detectors is practically complete with the exception of the 10° gaps produced by the magnetic coils that separate the sectors.

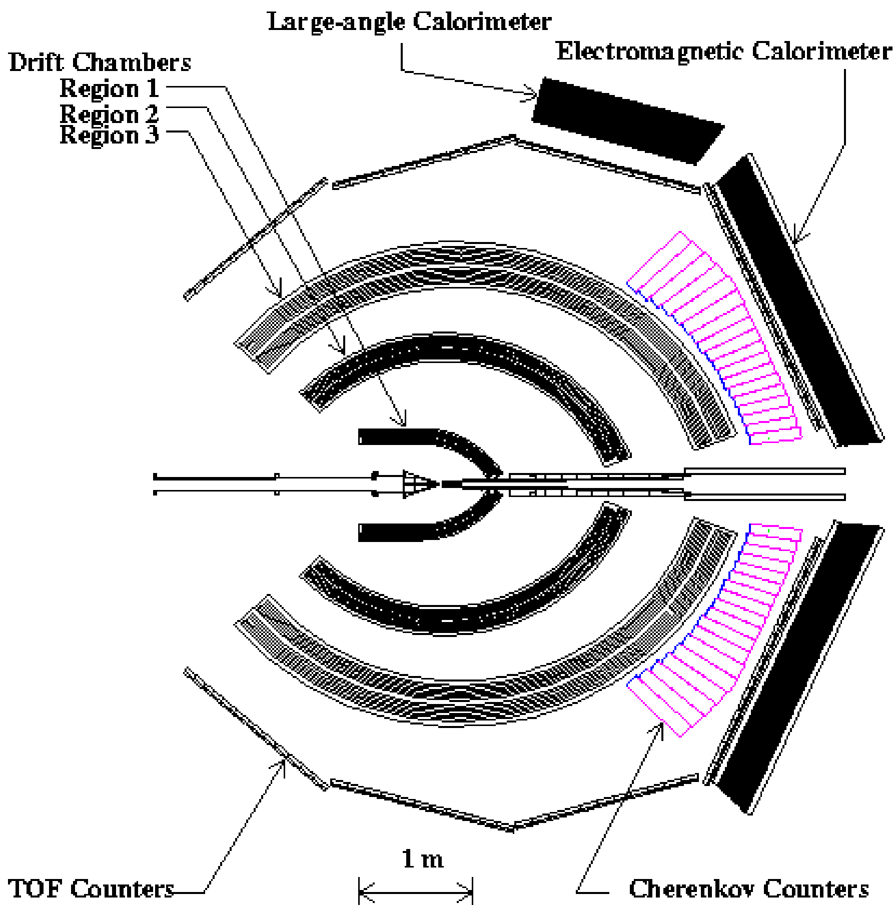

Figure 2-1: Slice through the CLAS detector containing the beam axis and showing two opposing drift chamber sectors [24].

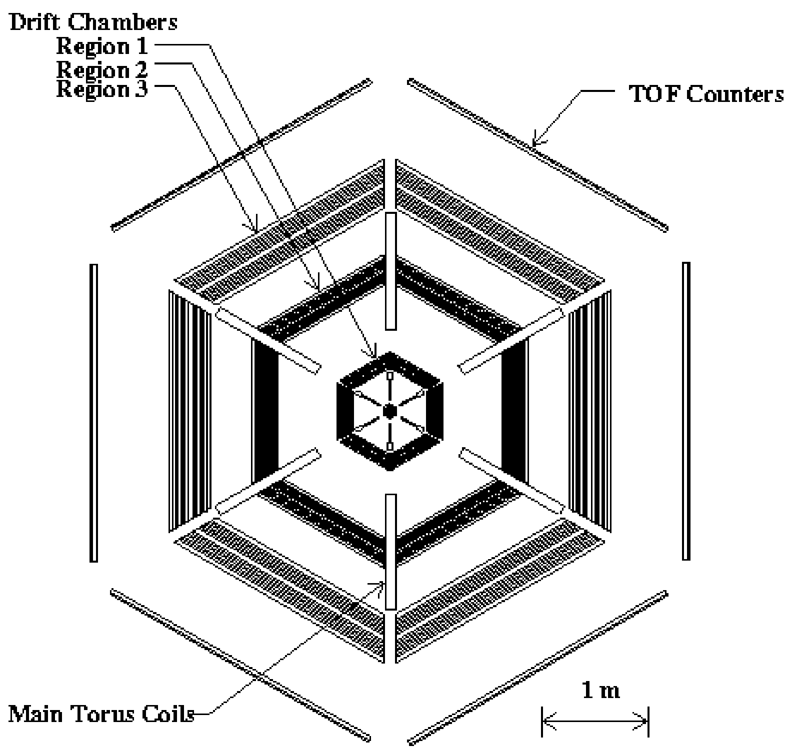

Figure 2-2: CLAS detector sliced perpendicular to the beam mid-way through the system [24].

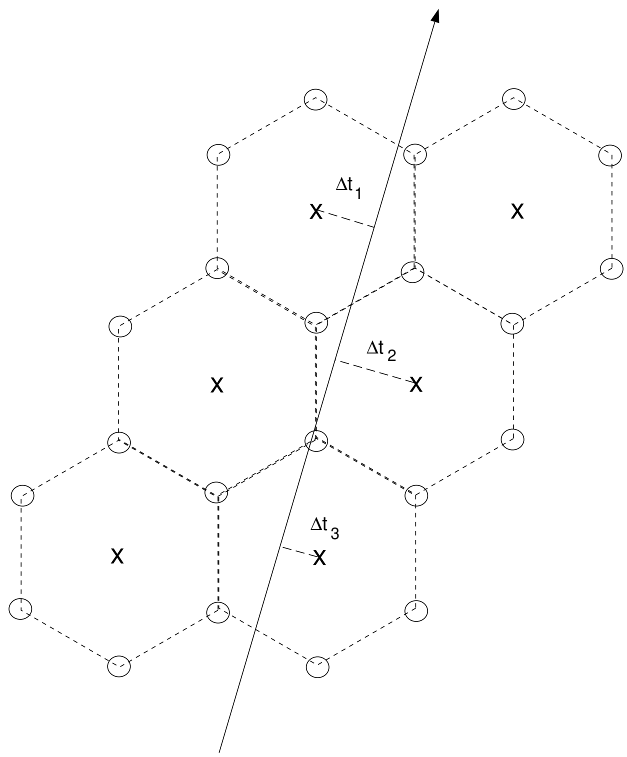

Figure 2-3: Schematic diagram showing a charged particle track passing through some portion of the Drift Chamber. The individual hexagonal drift cells are identified by the dashed line around the perimeter of each. The field wires are represented by circles, and the sense wires are represented by crosses. The measured drift time in each drift cell is associated with the shortest time for the electron drifting between the sense wire and the track. Actual drift paths can differ from the straight line if a magnetic field is present inside the DC. [22].

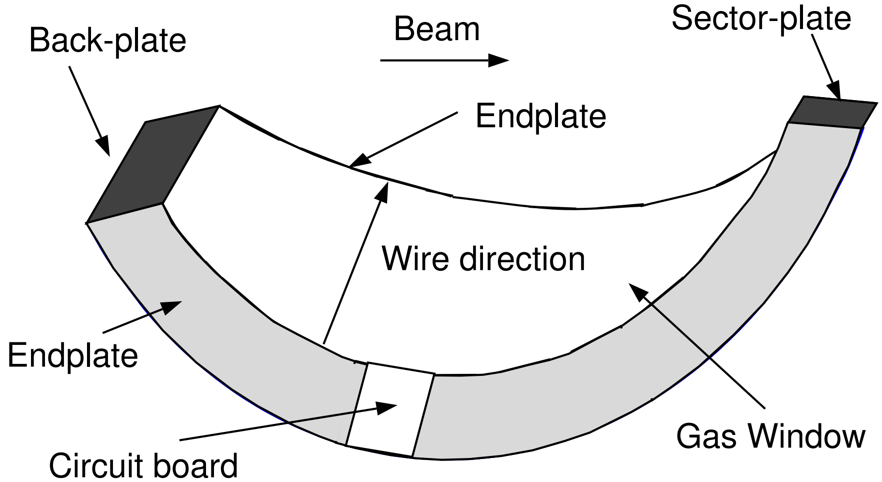

Figure 2-4: The CLAS Drift Chamber[12].

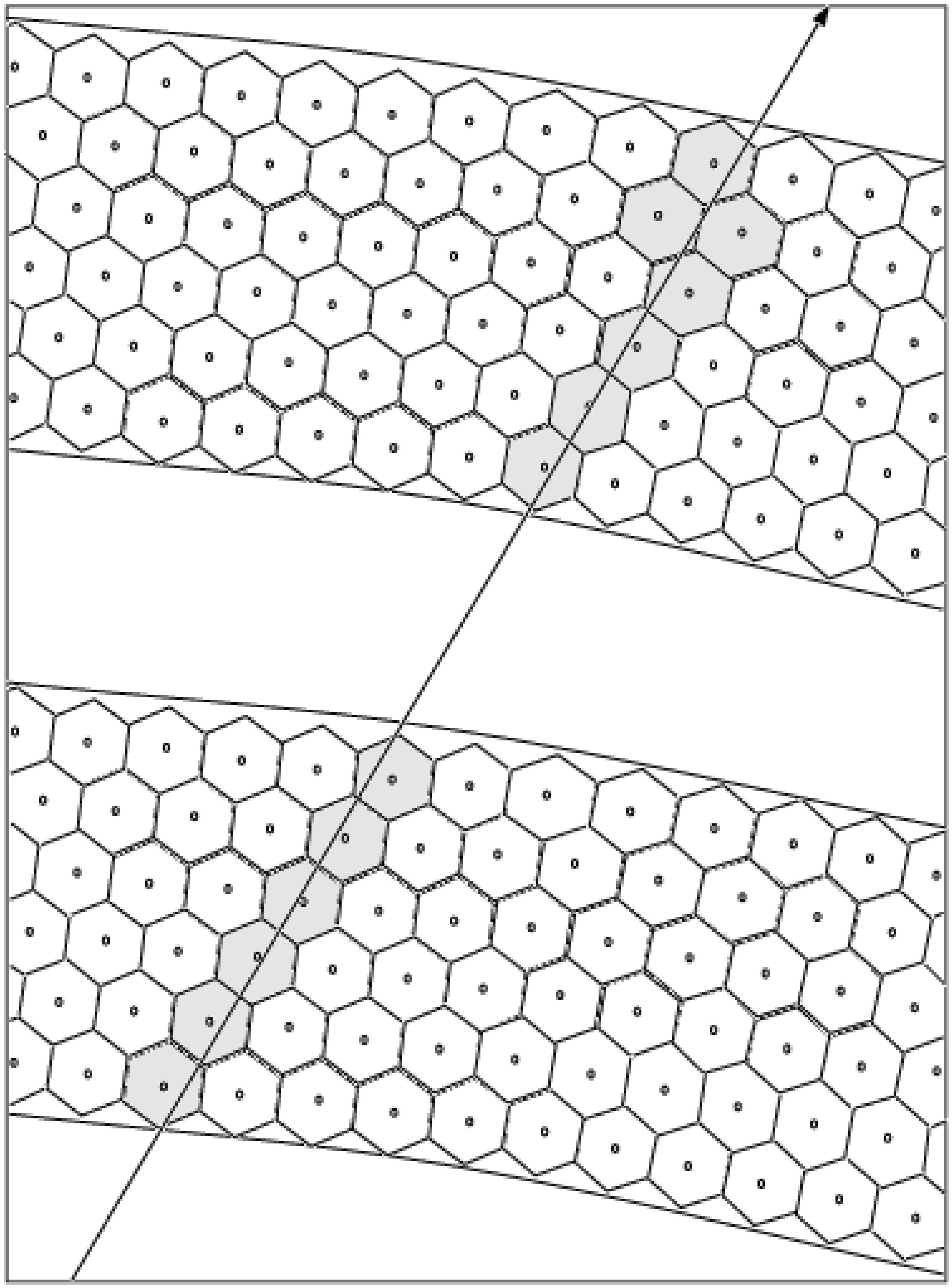

Figure 2-5: The wire layers inside each Drift Chamber are grouped into axial superlayer (bottom half of the plot) and stereo superlayer (top half of the plot). A particle track passing through both superlayers is shown.

2.2.1 Drift Chambers

Information about charged particle trajectories in CLAS is obtained by using the drift chambers. Drift chambers work in the following way. A charged particle traveling through the DC gas (Argon) produce ionization. The electric field inside the DC forces electrons and ions to drift to opposite directions. Electrons drift close to the sense wires where the electric field becomes very strong. In this region electrons collide with gas atoms and produce ionization, creating an amplification effect. An additional gas component such as CO_2 is usually required in order to absorb x-rays and prevent uncontrolled avalanches along the wire.

Drifting electrons from the avalanche reach sense wires and produce, together with the positive ions drifting into opposite direction, the electrical signal. The drift time reflects the shortest distance the electrons traveled, providing us with information about the position of the particle trajectory inside a DC cell (Fig. 2-3).

CLAS DC's are arranged in three regions. Region 1 is located closest to the target in a nearly magnetic field free region and is used to determine the initial direction of the track. Region 2 is located between magnetic coils, in the region of strong toroidal magnetic field, and is used to determine trajectory curvature. Region 3 is again in the field free region, and measures the final direction of a track. Each region consists of six separate sectors, each at different azimuthal angles.

Layers of wires are strung between the endplates of each chamber perpendicular to the beam (Fig. 2-4). Each drift chamber has its layers divided into two separate groups (Fig. 2-5). One is called the axial superlayer (that half of the wire layers that is closer to the beam) and the other is called stereo superlayer (that half of the wire layers that is farther from the beam). All superlayers consist of six wire layers except the axial superlayer of Region 1, which has only 4 layers. The mid-plane for each Drift Chamber is a plane that contains the beam line and passes through the middle of the Drift Chamber. The sense wires inside the axial superlayer are perpendicular to the beam and to the mid-plane. Sense wires inside the stereo superlayer are perpendicular to the beam but rotated by 6° with respect to wires in the axial superlayer. This rotation of the stereo wires in the plane, which is perpendicular both to the beam and to the drift chamber mid-plane, provides better resolution of the azimuthal angle of the track.

The drift cells have hexagonal form with sense wires surrounded by field wires to improve the electric field configuration. A high-purity gas mixture is delivered to the chambers by a gas-handling system. The gas mixture consists of 90% argon and 10% CO_2. Track position is measured with an accuracy of about 300 μm. The resulting resolution for charged particles is about $\frac{\delta p}{p} = 1\%$ for reconstructed momentum and about several mrad for reconstructed angles ϕ, θ.

2.2.2 Cherenkov Detector

The operation of the Cherenkov detector (CC) is based on the physical effect first discovered by Cherenkov. A particle traveling through the medium with a speed exceeding the velocity of light in this medium emits electromagnetic radiation. Because the velocity of light in the medium is $u = \frac{c}{n}$ where c is speed of light in the vacuum and n is index of refraction:

$$\beta = \frac{u}{c} = \frac{1}{n} \tag{2.1}$$

is the threshold for Cherenkov light emission. CLAS uses a Cherenkov gas detector with perfluorbutane, C_4F_{10}, as a medium. The perfluorbutane index of refraction of $n = 1.00153$ corresponds to a threshold in particle energy equal to

$$E = \frac{m}{\sqrt{1-\beta^2}} = \sqrt{\frac{n}{n-1}}m = 18.09m, \tag{2.2}$$

where m is the mass of the particle. The Cherenkov detector was constructed so that for the most part only electrons can have energy higher than the threshold. Thus, Cherenkov light emitted by electrons provides the signal that identifies them.

The Cherenkov detector is composed of six identical sectors. Two sidewalls of each sector sit in the planes of the CLAS magnetic coils. The detectors were gas

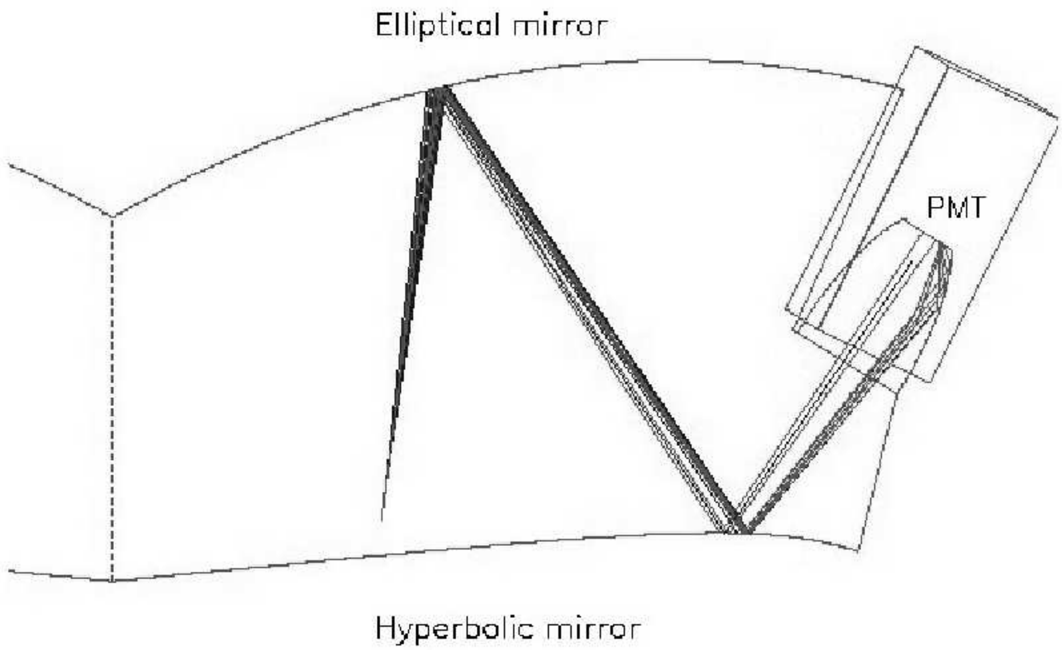

Figure 2-6: Cherenkov detector segment. In this figure, a particle moving upwards emits light inside the CC. The light is focused by the elliptical mirror into the hyperbolic mirror, which reflects the light into cylindrical mirror [23]. The light is collected by the MPT after reflection from the cylindrical mirror.

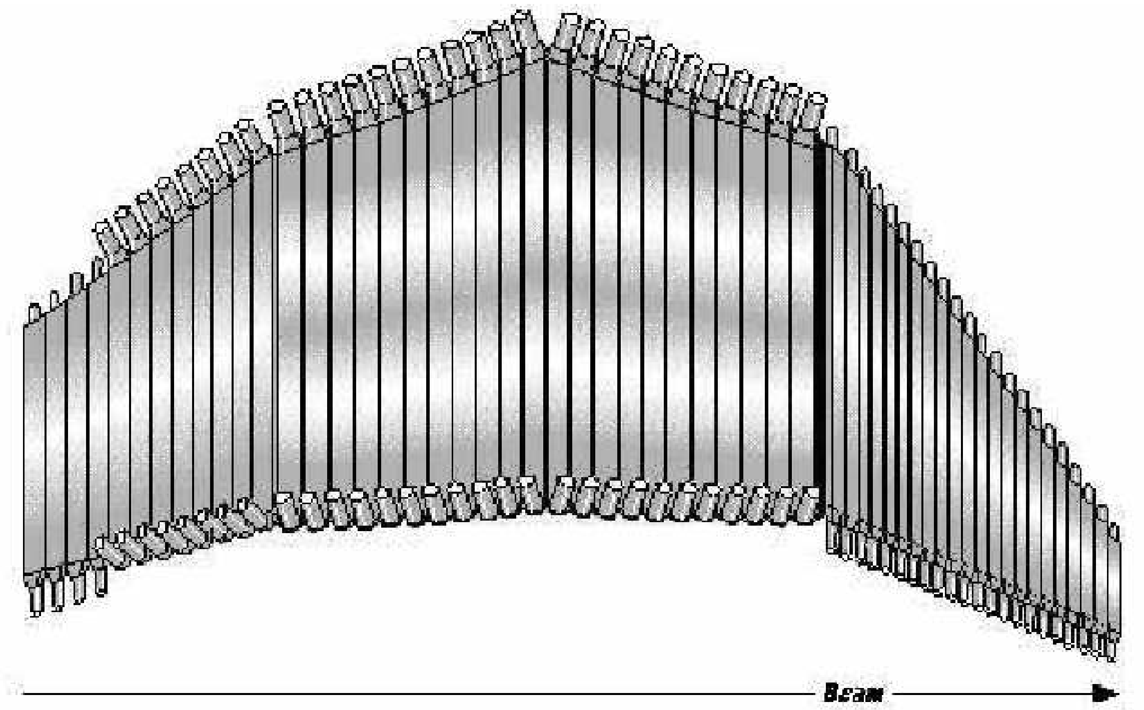

Figure 2-7: View of TOF counters in one sector showing the grouping into four panels. The forward-angle scintillators (panel 1 which is the rightmost section in the figure) have short stubby light guides and 2-inch PMTs. The large-angle system (the panels 2, 3, 4), except for the last four counters, has bent light guides coupled to 3-inch PMTs [24]

sealed and hold C_4F_{10} at 0.2% above atmosphere pressure. Each sector of the CC has a volume of about 6 cubic meters. Windows are made of 10 mil mylar surrounded on either side by 2 mil Tedlar [23]. Tedlar is a trademark of the DuPont corporation.

There are three different types of mirrors in the Cherenkov detector. Mirrors are aligned precisely, so that the Cherenkov light is focussed onto the photomultiplier tubes (PMTs). Light hits first an elliptical then a hyperbolic, and finally a cylindrical mirror before being collected at PMT as shown in Figure 2-6.

2.2.3 Time of Flight System (SC)

The time of flight system measures the time for a particle to travel from the point of interaction inside the target to the outer part of the detector where the TOF(SC) system is physically located. Knowledge of the particle trajectory from the DC system allows us to determine the particle velocity $\beta = \frac{l}{ct}$ where l is the path length. The path length is determined from the known positions of the target and the TOF counters and taking into account the trajectory curvature in the magnetic field inside the drift chambers. The time of flight t is determined from the knowledge of the trigger time t_{TR} and the time when the particle hits the SC, t_{SC}.

$$t = t_{SC} - t_{TR}. \tag{2.3}$$

Our experiment had an electron trigger, so

$$t_{TR} = \frac{L_{TR}}{\beta_{TR}}, \tag{2.4}$$

where L_{TR} is the electron path length and $\beta_{TR} = \frac{V_{el}}{c} = 1$ since the mass of the electron is very small. The calculated trigger time t_{TR} should not be used for the electron identification since the electron itself was used to calculate it. t_{TR} becomes important for identification of the other particles in the same reaction. Figures 3-3 and 3-4 show the quality of the CLAS particle identification and provide confidence that electrons are well reconstructed.

The curvature of the trajectory in the magnetic field inside the drift chambers gives us the particle momentum. Combining this information, we can determine the mass of the particle:

$$m = \frac{p\sqrt{1-\beta^2}}{\beta}. \tag{2.5}$$

The TOF system is positioned between the Cherenkov counters and the calorimeter and covers the angular range from 9° to 140°. It consists of scintillation bars oriented in the azimuthal direction relative to the beam. Each bar is perpendicular to the beam and to the sector mid-plane. Each one subtends about 2° of the scattering angle. The scintillation counters are 5.08 cm thick (along the particle trajectory), 15 or 22 cm wide. There are made of Bicron BC-408 and have a length varying from 32 cm at forward angles to 4.5 m at larger angles. Each of the six sectors has 57 scintillators with a PMT at each end. The average time resolution is about 120 ps.

2.2.4 Electromagnetic Shower Calorimeter

The Electromagnetic Calorimeter(EC) aids particle identification by giving information about the particle's total energy. The EC stops charged particles and measures the energy deposited in the scintillator, as described below.

The CLAS Electromagnetic Calorimeter consists of alternating layers of scintillator strips and lead sheets, with a total thickness of 16 radiation lengths. A 10 mm thick BC-412 scintillator sheet is followed by a 2.2 mm thick lead sheet in each layer as shown in Figure 2-8. In each CLAS sector, layers are contained within a volume having the shape of an equilateral triangle with one tip truncated. A particle traveling through the EC produces a shower in the lead. The energy of the shower is converted into light by the scintillator strips. This light is finally detected by PMTs. There are 39 layers in each CLAS sector. These layers form a "sandwich" that has the shape of an equilateral triangle with the tip truncated. To provide position resolution, each scintillator layer is sliced into 36 strips parallel to one side of the triangle, with the slice orientation rotated by 120° in each consecutive layer, and thus there are three orientations labeled U,V,W containing 13 layers each. Each EC sector is further subdivided into an inner (15 layers) and outer (24 layers) stack, to provide longitudinal sampling of the shower. The inner stack is the one that particles enter first.

Bicron BC-98 optical fibers with diameters of 3 mm are coupled to the readout end of each scintillator. The fibers from the scintillators are fanned into photomultiplier tubes. A light guide was used to couple rectangularly shaped scintillator bundles to the circular PMT photocathode.

The total energy deposited in the scintillators, expressed as a fraction of the incident particle energy, is called the sampling fraction $f_s = \frac{E}{P}$. This ratio depends on the ratio of active to passive material, as well as the total thickness. For the CLAS Calorimeter $f_s = 0.256$.

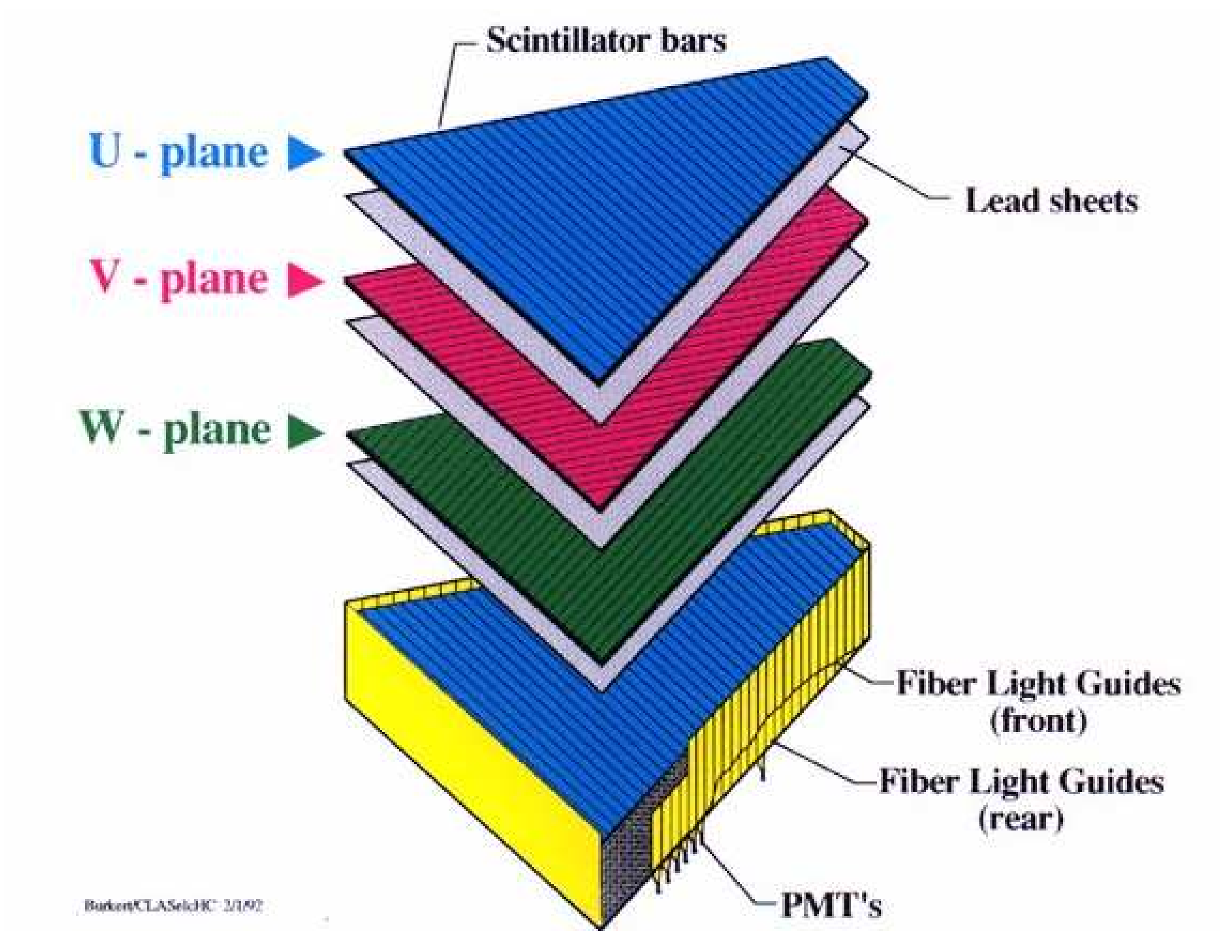

Figure 2-8: Electromagnetic Calorimeter [23]. In this figure, a particle is coming from above and passes through the alternating layers of scintillator bars and lead sheets. Each scintillator sheet is sliced into 36 bars parallel to one side of the triangle. Each slice orientation is rotated by 120° in each consecutive layer. U,V,W label 3 possible slice orientations. Only three layers, each consisting of lead sheet and scintillator bars, are shown in the picture. The actual EC has 39 such layers stacked on top of each other.

The EC energy resolution is about

$$\frac{\Delta E}{E} = \frac{0.1}{\sqrt{E(GeV)}}. \tag{2.6}$$

The overall EC position resolution is $\sigma = 2.3$ cm. The time resolution of the calorimeter is about $\tau = 3$ ns. This results from a combination of fluctuations in the length of the light path in the scintillators, photoelectron statistics and the timing characteristics of the PMT used.

The EC is included in the CLAS hardware trigger. The electron trigger is always configured so that it accepts mostly electrons but not pions. If a good electron candidate makes a trigger, information is recorded about all the particles in the reaction. If the reaction does not have a good electron candidate, the reaction is completely ignored and is not written to the data-stream.

2.2.5 Cryogenic Target

The target material for our experiment was contained in target cells that were fixed to an aluminum stick. During the experiment, the stick with the target cells was submerged in liquid helium to prevent de-polarization of the target. A motor was used to move the target stick so that different target cells could be positioned on the beam axis at different times.

The target stick supports four different cells as shown in Figure 2-9. The cells have the following dimensions: $1.5cm$ diameter, $1cm$ length. The entrance to each target cell was covered by a $25\mu m$ aluminum foil and the exit windows were made of $50\mu m$ kapton foil. One cell was used for the polarized NH_3 target, and another one for the polarized ND_3 target, while the other two cells were used for carbon and the empty target. The empty target as usual allowed us to perform background measurements. Each cell has cylindrical form. Coils for the NMR polarization measurement are located outside the NH_3 and the ND_3 cells (wrapped on the external surfaces of the cylinders). The NH_3 and ND_3 targets are polarized dynamically by microwave radiation. The microwave irradiation is supplied by a trumpet positioned at 10 mm

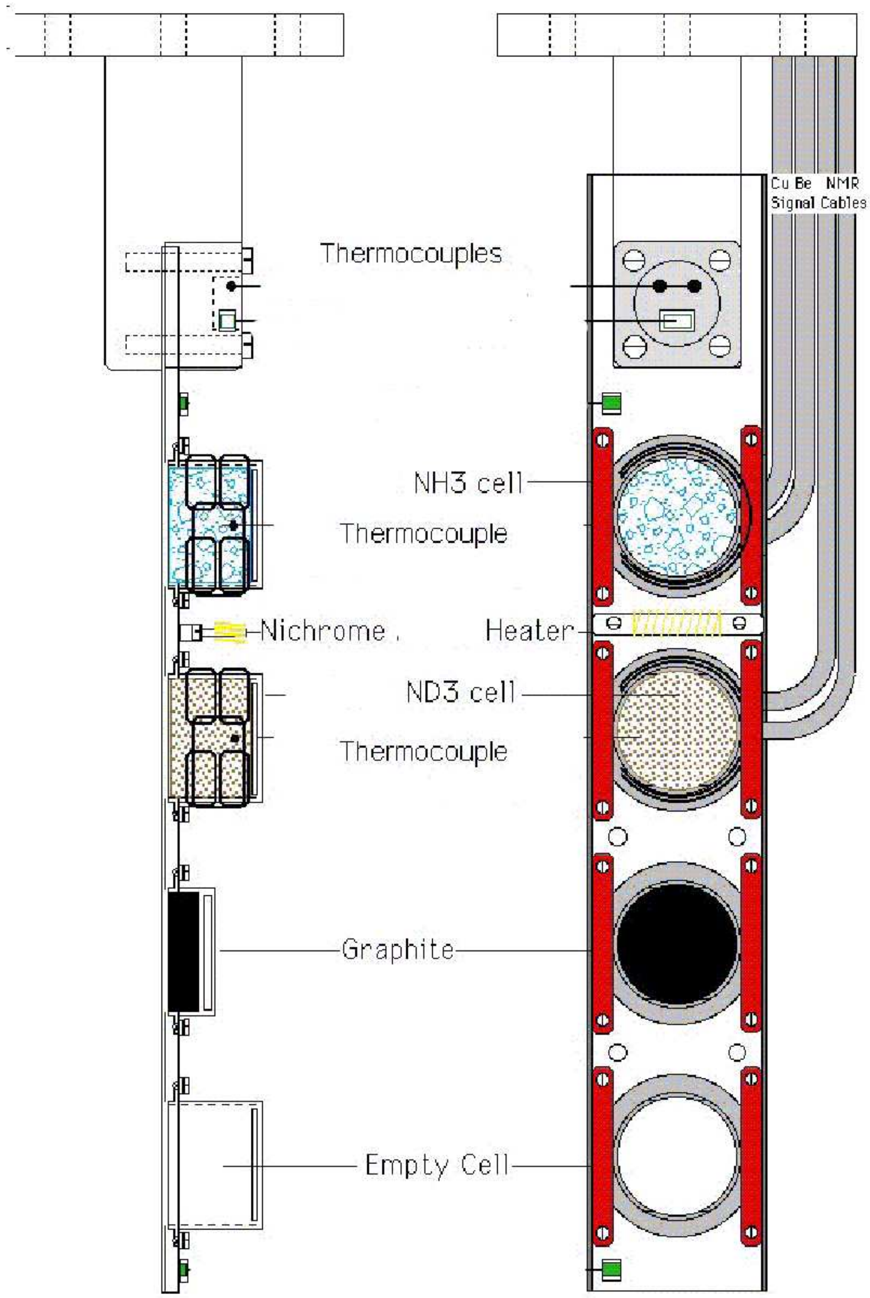

Figure 2-9: Target Stick [27]. The left part of the figure shows the stick sidewise, perpendicular to the beam that is directed from left to right. The right part of the figure shows the front view of the stick.

distance on the side of the cell.

To cancel the effects of radiation on the polarized targets we have used annealing (heating of the material to 70-80 K). The annealing resistor has been located between the first (NH_3) and the second (ND_3) cells. It is labeled as "Nichrome Heater" in Figure 2-9.

The target temperature was controlled through thermocouples positioned inside the cells. The liquid helium level was monitored by a helium level gauge. A stepping motor was controlled from outside the target chamber to allow the up and down movement of the central rod of the target to place the different target containers on the beam axis.

The target stick is inserted in the target chamber, called the "banjo," through the stainless steel pipe that is attached to the chamber's top. The banjo has a cylindrical form. Its diameter and length are $20cm$ and $1.5cm$ respectively. The banjo entrance and exit windows are made of $71\mu m$ aluminum. The target chamber is connected to a refrigerator which fills the banjo with $1^{\circ}K$ liquid helium. The entire target is contained in the outer vacuum can (OVC) which provides a vacuum of $10^{-7}Torr$. The OVC has a $71\mu m$ aluminum entrance window $65cm$ downstream from the target material and a $71\mu m$ aluminum exit window $24.9cm$ upstream the target material.

The NH_3 polarized target has ^{15}N nuclei. Ideally ^{15}N should have been used as a background target but ^{15}N boils around 77K and is liquid below that, which makes it very difficult to handle. Because of that, ^{12}C has been used instead. ^{12}C is very easy to handle and its properties are not too different from ^{15}N. Its binding energy per nucleon is the same to better than 10 keV and its first excited states are relatively close (4.4 MeV instead of 5.3 MeV). The difference in separation energy for a proton (6 MeV) should not matter at our energy transfers. The Fermi momenta are also comparable.

2.3 Calibrations

The CLAS system has many elements that require careful calibration in order to make reliable measurement of cross sections. The results of all of these calibrations and the techniques used in making the calibrations are available from the Hall B collaboration in the form of written notes called "CLAS notes." These are very general calibrations that pertain to all the experiments performed at CLAS, and are used by all the collaborators for analysis of their specific data. The CLAS notes are available on the CLAS web page at $www.jlab.org/Hall-B$. Among the calibrations are the following:

1) time offsets for each paddle of the Time of Flight detector,

2) energy deposition in the Electromagnetic Calorimeter,

4) time-to-distance function for Drift Chambers,

5) left-right PMTs time alignment,

3) energy deposition in the scintillation counters,

6) target alignment with the beam.

We select the last three items for more detailed discussion below as an example.

2.3.1 Left-Right PMTs Time Alignment

Each TOF counter has photomultiplier tubes on opposite ends. The time measurement, t, of the leading-edge of the pulse generated by the PMT allows one to determine the time when a particle hit the scintillation bar. The leading edge corresponds to the light which arrives at the PMT directly (without additional reflections from the scintillator walls). Thus the distance traveled by such light is directly related to the position of the hit along the scintillation bar. The difference between the time reported by the left and the time reported by the right PMT can be used to infer the position of the particle hit along the length of the scintillation bar. The location of the hit, x (0 is in the middle of the bar), is

$$x = \frac{V\Delta t}{2}, \tag{2.7}$$

where V is the velocity of light in the scintillator. V is approximately equal to 16 cm/ns.

Ideally the time reported from the left and right PMTs should be the same for a hit in the middle of the scintillation bar. In practice it is not always the case, for example, because of the different cable length leading to the left and right PMTs. Calibration of the timing offsets is required. Left-right offsets can be found by examining the distribution of the hit position for each counter. The distribution should start from the x value equal to the position of the left edge of the scintillation bar, P_L, and end at the value of x equal to the position of the right edge of the scintillation bar, P_R. The edges of the distribution should be symmetric with respect to zero. The left-right offset constants for each scintillation bar can be easily found as

$$\Delta t = \frac{P_L + P_R}{V}. \tag{2.8}$$

Figure 2-10 shows the distribution of the hits in each of the counters in sector 1 after the left-right calibration. The properly aligned counters correspond to the picture being symmetric with respect to zero, as it is.

2.3.2 Energy Deposition in the Scintillation Counters

Minimum Ionizing Particles (MIPs) deposit about $10 MeV$ of energy in the scintillation counter. This can be used for calibration of the SC energy deposition. Fast pions ($p > 0.3 GeV/c$) were selected for calibration. The distributions of the TOF ADC values for each counter were examined and scaling coefficients that convert ADC channels to energy loss were found. Figure 2-11 shows typical distribution with MIP peak at approximately 550 ADC channels. For particles with angles greater than $45°$, there is no detector (CC or EC) for particle identification and the energy loss in the SC system is important for particle identification.

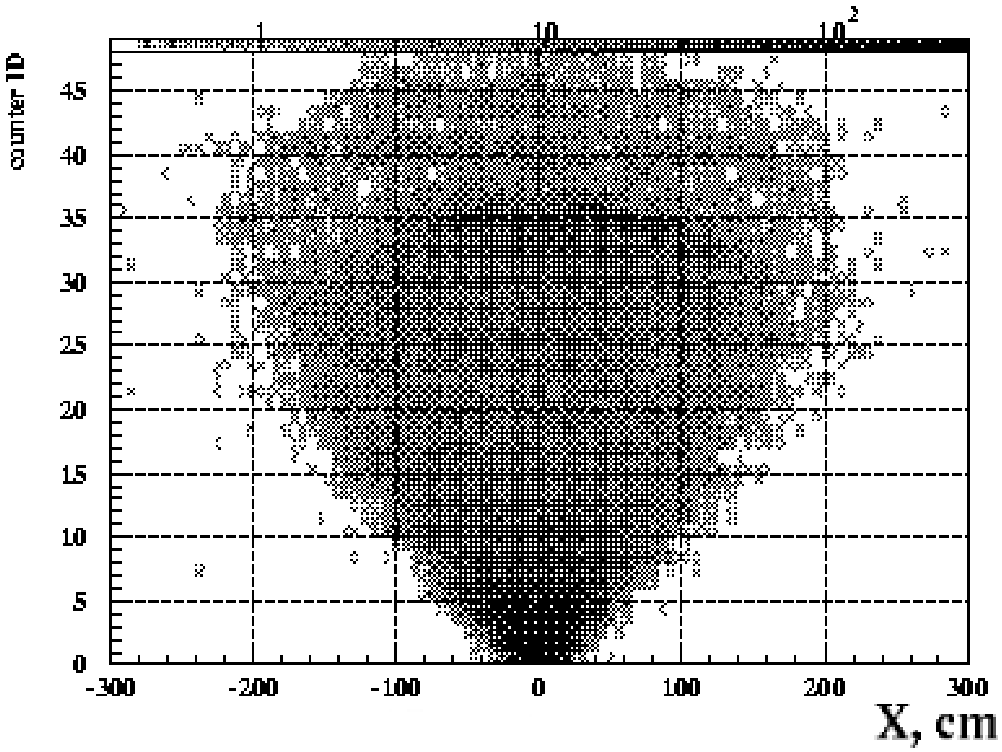

Figure 2-10: Position distribution of the hits in the counters after the left-right calibration. Counter number (ID) is shown vs x position of the hit. Aligned counters correspond to this picture being symmetric with respect to zero [26].

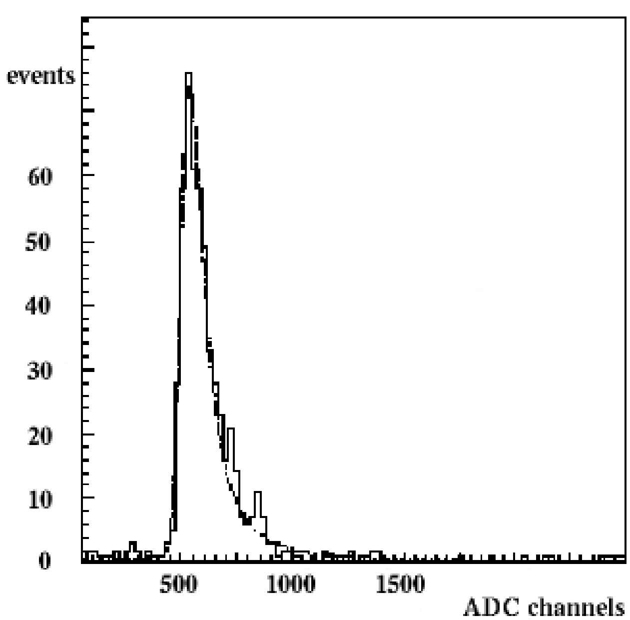

Figure 2-11: Typical pulse-height spectrum of MIP hits in a TOF counter. The spectrum is the geometric mean of right and left PMTs [26], [24].

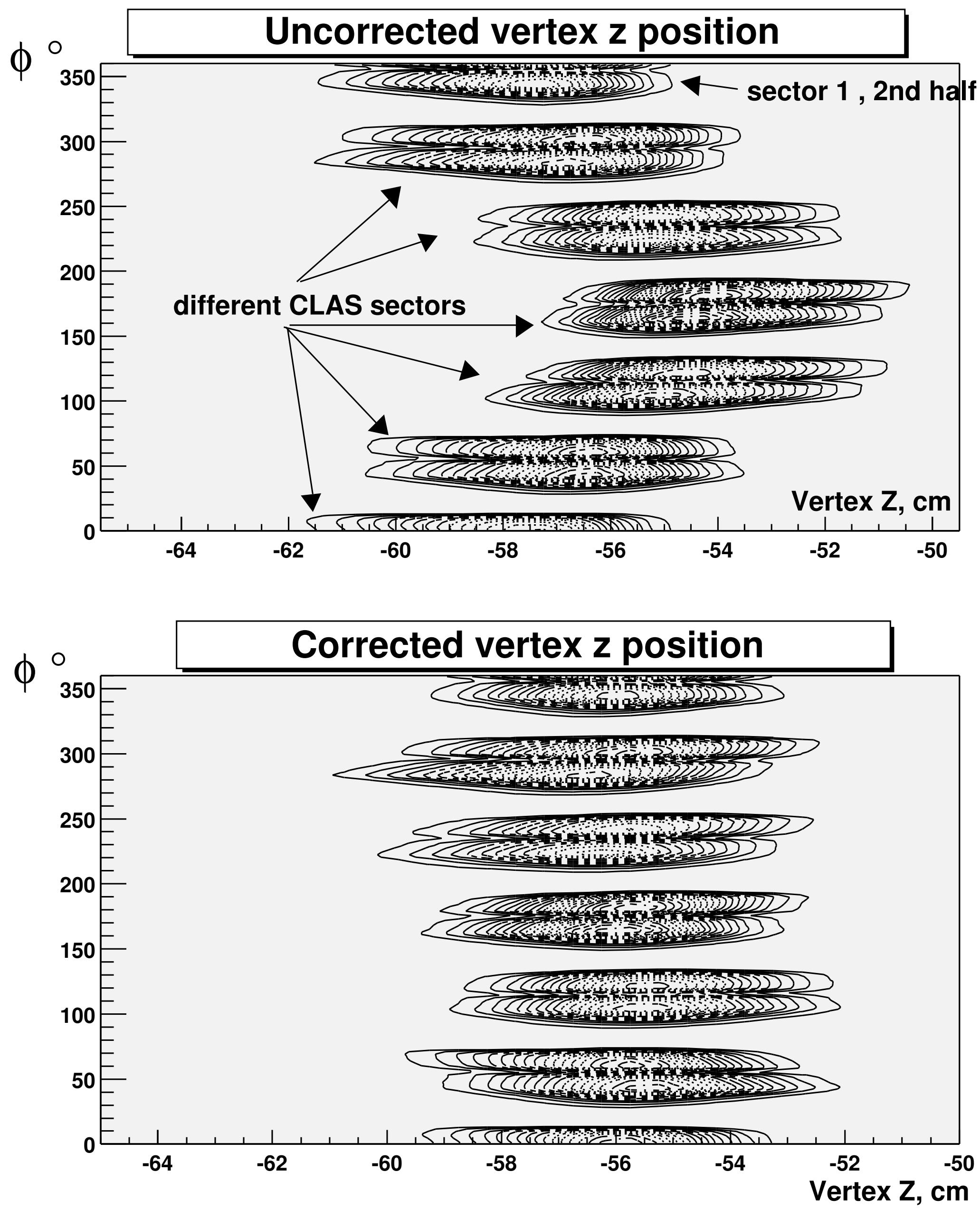

Figure 2-12: Misalignments of the CLAS produce misalignment of the reconstructed position of the target. The reconstructed target Z position (along beam line) varies from sector to sector and is a function of azimuthal angle ϕ. This variation can be corrected as described in Section 2.3.3. The top figure shows the reconstructed target Z position. The bottom figure shows the actual target position Z_0 obtained by applying the correction to Z.

2.3.3 Target Position Correction

Even a small misalignment between the electron beam, the symmetry axis of the Drift Chambers and the symmetry axis of the CLAS magnetic field can result in considerable error during reconstruction of the target position by means of projecting the particle track back to the point of origin. Variations in the reconstructed target Z position (along beam line) from sector to sector create problems during the application of any vertex cuts. Such cuts are needed because we want to isolate and remove the contribution to our data from the target windows. The correction to the reconstructed target Z position can be calculated and used to correct the data. A shift between the CLAS symmetry axis and the beam line will result in the shift of the reconstructed target position Z from the actual target position Z_0:

$$Z = Z_0 + D * ctan\Theta * sin(\phi - \phi_0), \tag{2.9}$$

where Z_0 is the real z coordinate of the target, Θ and ϕ are the particle scattering angles, D is the amount of the shift between the beam line and the CLAS symmetry axis and ϕ_0 is the angle between the direction of the shift and the beam line.

As can be seen, one has to apply a correction individually for each particle in order to calculate Z_0 from the reconstructed position Z. The amount of beam and CLAS misalignment D and its direction ϕ_0 can be obtained by fitting the experimental data with D and ϕ_0 as free parameters. D essentially is an amplitude of the "sine" wave in the plot "reconstructed target Z vs ϕ " and ϕ_0 is its phase. The result (Fig. 2-12) shows that D is less than 1 mm which is very reasonable since any larger misalignments could have been detected by surveyors.

Chapter 3

Data Analysis and Evaluation of Systematic Errors

3.1 Data Quality Monitoring

Only data runs that showed consistent data have been used for analysis. The ratio of electrons in different sectors and the number of electrons normalized to the Faraday Cup have been monitored to ensure the quality of the data. The ratio of the number of electrons in sector 3 to the number of electrons in sector 4 is shown in Figure 3-1 for several consecutive runs. The ratio of electrons N_r in different sectors of CLAS should be a constant number for each of the running periods.

Differences in the number of electrons in different sectors was not used by itself as a reason to discard runs because sectors have different inefficiencies. Malfunctioning of the drift chamber or any other hardware fault such as the loss of the voltage in the TOF system changes N_r dramatically. The DC malfunctioning in sector 3 during run number 50 has changed the ratio N_r considerably.

The asymmetry A_{el} of the elastic scattering rate was monitored.

$$A_{el} = \frac{N^+ - N^-}{N^+ - N^-}, \tag{3.1}$$

where N^+ and N^- are the number of events with positive and negative helicity. Each

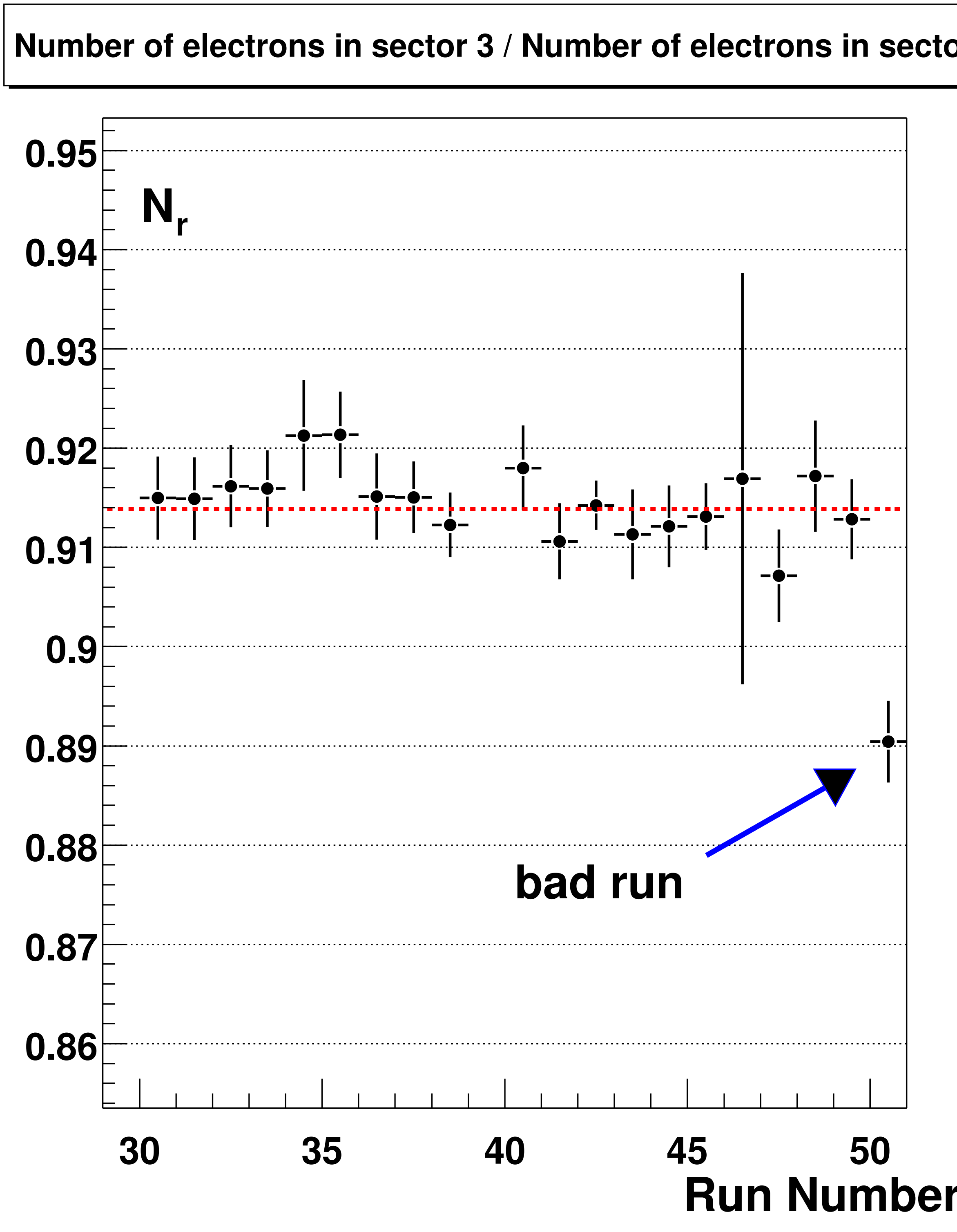

Figure 3-1: The ratio of the number of electrons in sector 3 to the number of electrons in sector 4 is shown. The ratio of electrons, N_r, in different sectors of CLAS should be a constant number for each of the running periods. The DC malfunctioning in sector 3 during the run number 50 changed the ratio N_r considerably.

run has very small asymmetry but its sign allowed us to check that all runs are correctly labeled with respect to the sign of the target polarization. The opposite target polarization reverses the sign of A_{el}. We did not use any asymmetry information to discard runs because of the possibility of introduction of bias into the physical asymmetry.

3.2 Data Analysis

3.2.1 Helicity Pairing

The helicity of the electron beam was changed with the frequency of $1Hz$. The beam helicity structure was tied to a synchronization signal, "sync". "Sync" consists of an array of zeroes and ones alternating every second. An additional signal, "increment," was recorded, which showed an integer value incremented by one every time helicity changes. The helicity of the beam, the "sync" and the "increment" signals were recorded for each event (information set A). The Faraday Cup information about each helicity pulse is necessary for proper normalization of the data. This information along with the helicity and the "sync" signals was written out to the data stream every 10 seconds (information set B). Data analysis requires precise matching of the information in set B to the information in set A since set B is not written for every event. This matching is a complicated task because it is not clear which helicity pulse from set B corresponds to which event from the set "A" without a careful analysis. This matching is essential for a quantitative analysis of any experiment with polarized beam.

Data acquisition dead time (see section 3.2.5) introduces irregularities into set A. One of them is that the electron beam was available (its properties was recorded in the set "B") but no information was written out to the set "A". Failures of the "increment" signal to increment and other hardware problems complicates the matching significantly.

The matching of the sets A and B was done on the bases of the helicity and the

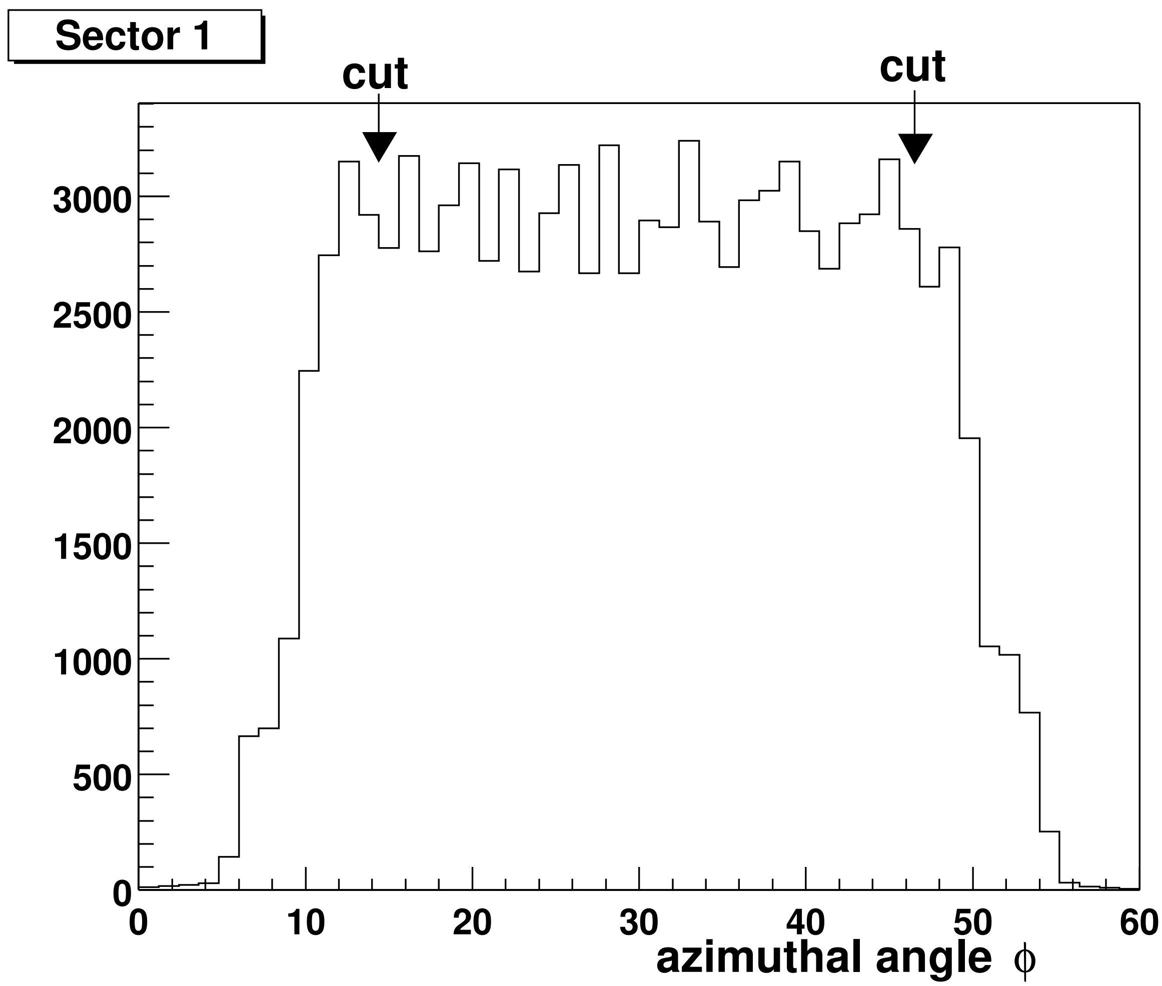

Figure 3-2: A distribution of the number of electrons in sector 1 as a function of azimuthal angle ϕ. The beam energy is 2.6 GeV. The edges of the detector are not efficient and are eliminated by the fiducial cut. The distribution in the middle of the sector ($\phi = 30°$) is flat.

"sync" signals that are present in both sets. This matching is a matter of pattern recognition. The errors are similar to Faraday Cup errors discussed in Section 3.3.5. The helicity matching is incorporated in HelP program that was used to produce compressed data storage tapes (DSTs) for our experiment. All final data analysis was done using DSTs.

3.2.2 Fiducial Cuts

The efficiency of CLAS is a very complicated function of particle momentum and scattering angles. Fortunately most of the inefficiency is concentrated along the edges of sectors while the middle portions of the sectors are nearly 100% efficient. A fiducial cut was designed to take into consideration only these efficient regions of CLAS. The cut eliminates sector edges as well as holes in different parts of the detector. These holes were created by malfunctioning SC counters or other hardware devices. The fiducial cut is potentially different for different particles and an acceptance calculation for exclusive reactions can be complicated, but for inclusive electron scattering the situation is simpler since we have only one type of particle and the cross section is independent of azimuthal angle ϕ. The electron acceptance A is a function of electron momentum p, its polar Θ and its azimuthal ϕ angle:

$$A = A(p, \Theta, \phi). \tag{3.2}$$

To derive the acceptance function, the data have been binned in small segments in momentum p and angle Θ. The resulting distribution of the number of events as a function of ϕ angle was studied. This distribution should be flat since the inclusive cross section is independent of ϕ . A fiducial cut was designed to select the ϕ-independent flat region in the middle of the sector as shown in Figure 3-2. To make the cuts more manageable, empirical acceptance functions were used to represent the collection of these cuts. The experiment used several magnetic field settings. The acceptance functions have been calculated separately for different CLAS magnetic field configurations.

3.2.3 Electron Identification

A very important step in the analysis is the identification of particles in the final state. In the inclusive analysis, we are mainly interested in the separation of electrons from all other particles. A number of different particles can be present in the final state, namely protons, neutrons, pions, kaons, photons, and electrons. Protons, neutrons, photons, π^0 and π^+ have electric charge different from the electron charge e. Separation of these particles from electrons is relatively easy, since particles of opposite charge produce tracks bent in the opposite direction in the CLAS magnetic field and neutral particles do not produce tracks in the drift chambers at all.

The mass of a charged particle can be determined from the knowledge of its momentum and velocity as described in Section 2.2.3 "Time of Flight System." This mass is one of the elements used for particle identification (Fig. 3-3, 3-4). It can be seen from Figures 3-3 and 3-4 that separation of electrons from pions becomes problematic for fast pions with momentum $p > 0.5$ GeV, while separation from other particles is straightforward.

Kaons are very rare and do not produce any sizable contamination. The dominant source of electron misidentification is the presence of negatively charged pions π^- in the final state. A relativistic pion can be misidentified as an electron when the pion mass becomes negligible in comparison with pion energy. A series of cuts described in the next section was developed to minimize pion contamination. CLAS has been designed in such a way that it produces different responses for different particles. We will use knowledge of the CLAS hardware and its calibration to make the electron-pion separation.

Initial Particle Identification

During initial preprocessing of the data ("cooking") the following cuts have been applied to select electron candidates [36]:

1) An event was recorded only if there was at least one negative track that geometrically matched hits in the Electromagnetic Calorimeter or in the Scintillation Counter.

2) If an event had only one negative track it was defined to be the scattered electron.

3) If an event had several negative tracks, the candidate that matched the electron characteristics the most (i.e. had hits in EC, CC and TOF) was defined as an electron.

4) After an electron has been found, time of flight and momentum analysis was

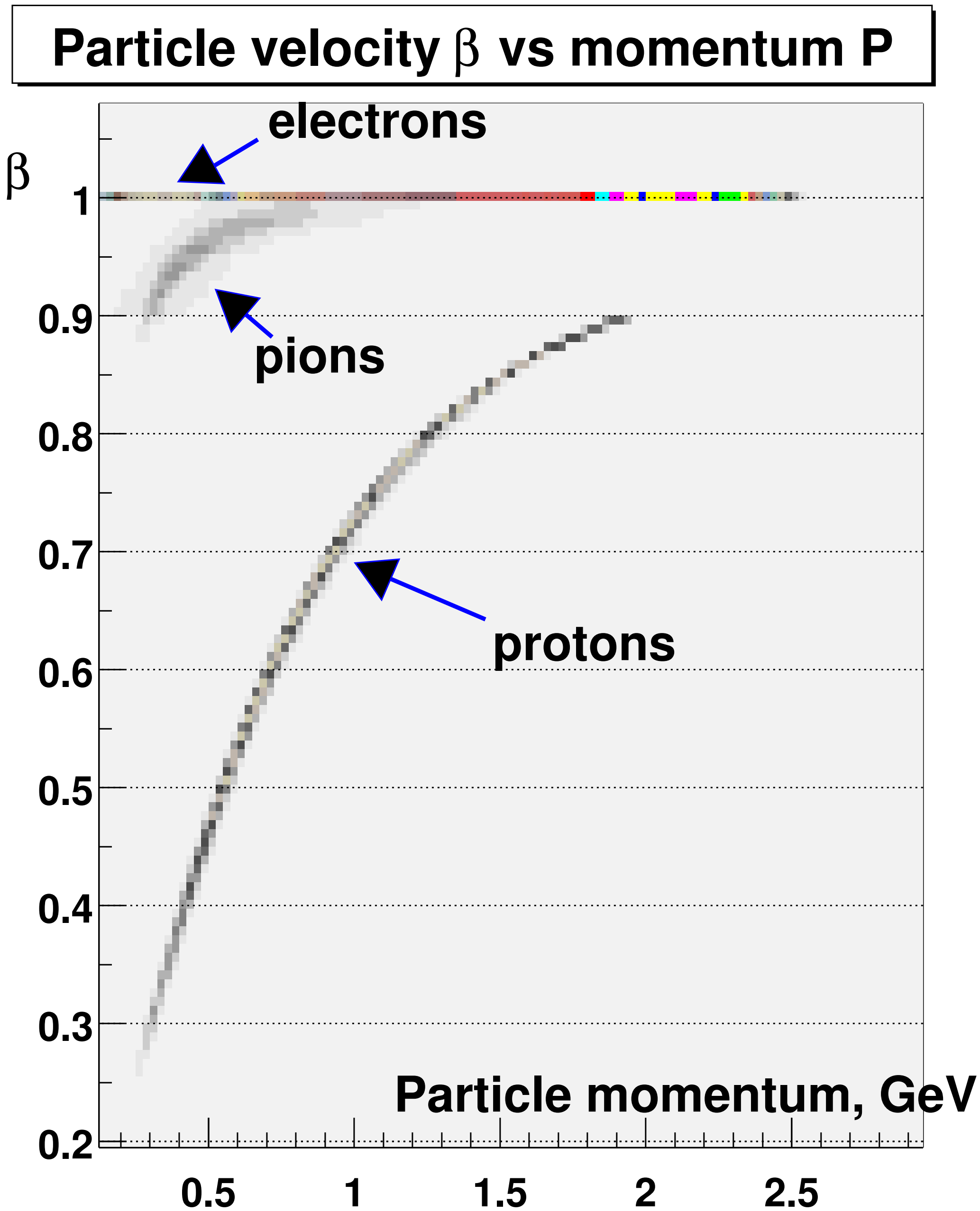

Figure 3-3: Charged particles detected by CLAS. Particle velocity $\beta = \frac{V}{c}$ is plotted vs particle momentum P. The beam energy is $2.56 GeV$. β is determined from the Time of Flight System. The momentum P is calculated from the curvature of the particle track in the magnetic field as determined by the Drift Chambers.

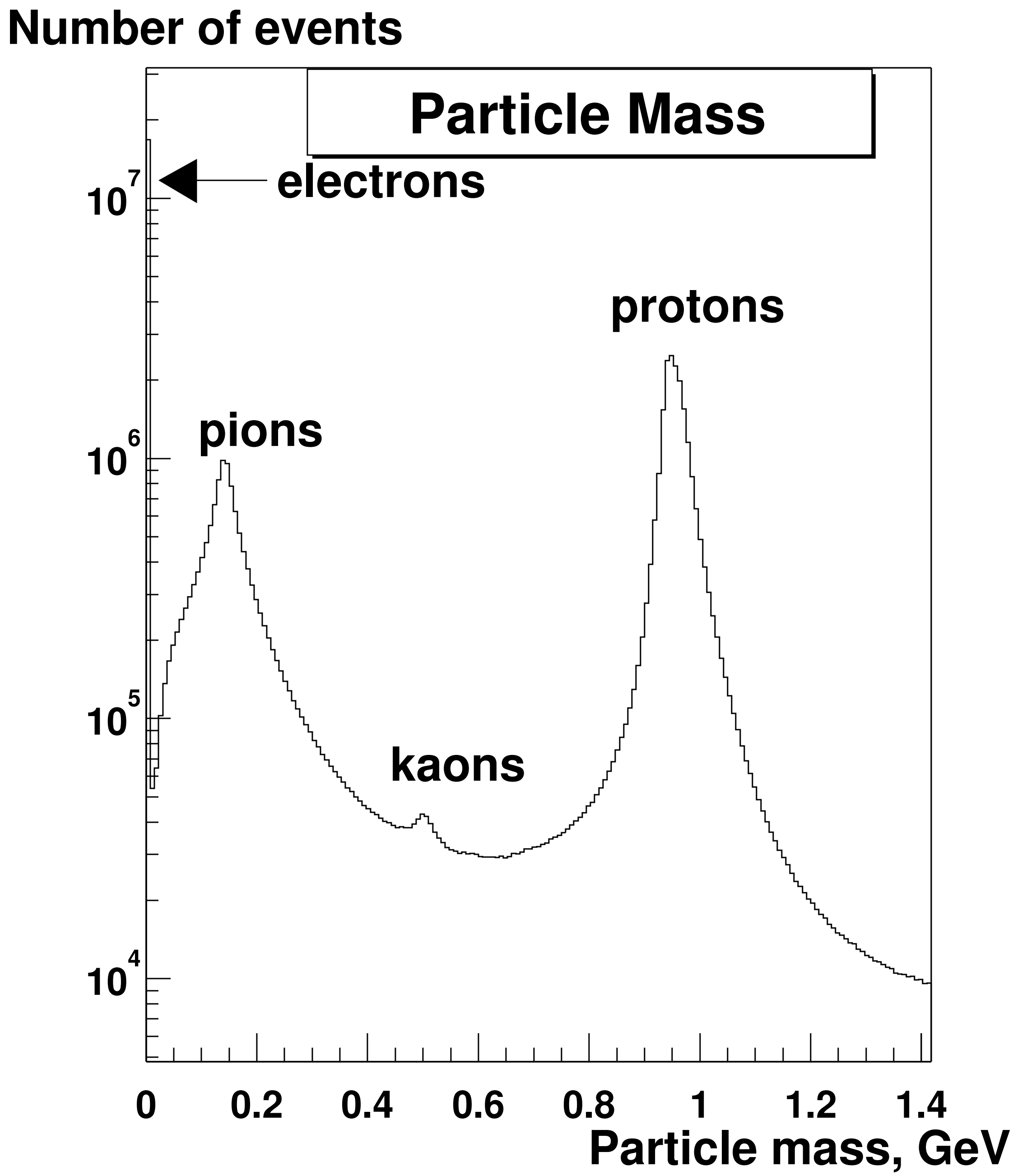

Figure 3-4: Charged particles detected by CLAS. The distribution of the particle mass as calculated from the particle velocity β and particle momentum P. The calculation is described in Section 2.2.3.

used for identifying other particles in the event.

The above cuts are very loose in terms of electron selection. Only extremely small number of electrons has been thrown out or misidentified as pions. After such a procedure, pions have much greater chance to be misidentified as electrons.

Final Electron Cuts

As we have shown above, after initial preprocessing of the data, we are left with a data sample that has very loose electron definition and as a consequence has possible π^- contamination. More restrictive cuts have to be designed to separate π^- contamination from electrons. The following sequence of cuts was used to achieve this goal.

1) Cut on the position of the electron vertex along the beam line. This cut allows separation of the events that originated in the target from the background events that originated in the cryostat widows and radiation shields. The cut does not allow separation of the target material from the banjo and target cell windows or liquid helium that fills the banjo due to the lack of resolution along the beam line.

2) Require a hit in the Cherenkov counter with more than 1.5 photoelectrons.

3) Require the energy deposition in the inner layer of the EC to be more than $0.05 GeV$.

4) Matching the total energy deposited in the EC to the particle momentum.

5) Require the total energy deposited in the EC to be not less than the energy deposition in the EC inner layer.

All of the above cuts are discussed below in detail.

Cut on Electron Vertex

Tracks in the Drift Chambers can be used to reconstruct the paths of the charged particles. The magnetic field from the CLAS main torus exists only in the second region of the Drift Chambers. A knowledge of the target magnetic field allows reconstruction of the track from the edge of the DC back to the target. For any track t we can construct a plane P_t which would contain the beamline and would have its

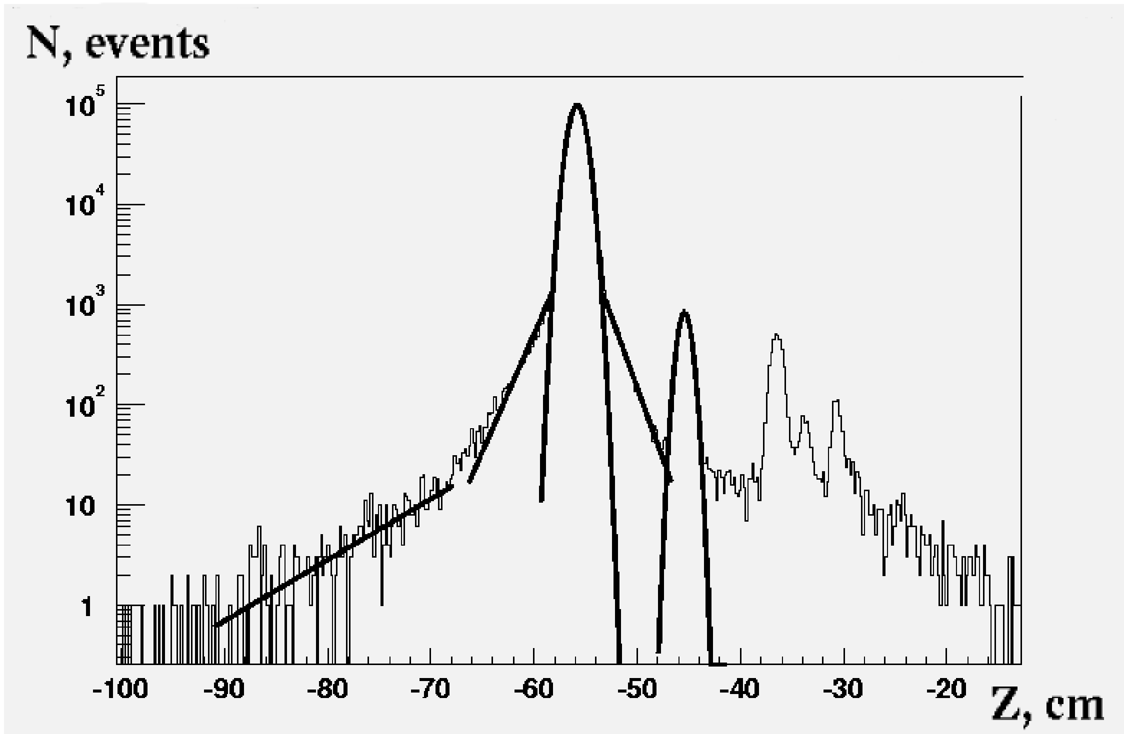

Figure 3-5: Distribution of the z position of the electron vertex along the beam line (cm). The central peak represents scattering from the target material, target cell and banjo windows as well as liquid helium that fills the banjo. The peaks to the right represent scattering from the radiation shields and the OVC exit window.

normal vector in the same plane as the beamline and the track. The intersection of the track with this plane is defined as the vertex position. This vertex position is our best estimate about the actual position of the interaction point inside the target.

Fig. 3-5 shows typical a distribution of the vertex position along the beam line. If we introduce a coordinate system with z axis along the beam line and with zero in the center of the CLAS detector, then the z vertex coordinates have to be in the vicinity of the actual target position: $z = -57cm$. To compensate for the effects of the slight misalignment of the beamline, the target and the CLAS symmetry axis, we have to apply a vertex correction first. The correction is discussed in Section 2.3.3.

In Fig 3-5 we can identify the main target area due to scattering from the NH_3 material and from the windows to the right of the target.

The central peak in Fig. 3-5 represents scattering from the target material, target cell and banjo windows as well as liquid helium that fills the banjo. We will call this region “the main target area.” The peaks to the right represent scattering from the radiation shields and the Outer Vacuum Can(OVC) exit window. We will call these peaks “windows.”

Several assumptions have been made about the shape of the distribution. The left slope of the target distribution can be fitted with a Gaussian and two exponential tails. The first half of the target right tail can be well fitted with an exponential tail symmetrical to the tail on the left side. We made an assumption that the second part of the right target tail is also symmetric to its counterpart on the left. We also assumed that the shapes of the windows to the right of the target are similar to the shape of the target distribution. The last assumption is justified because

1) all these distributions are formed by the particles of the same type (electrons)

2) the windows are not that far from the target so that the detector efficiency is about the same for electrons coming from the target or the target windows.

We are not sensitive to the exact shapes of the distribution tails because of the very limited number of events in them. As we will show below, a rough estimate is all we need. The above assumptions are good enough for that purpose. Under these assumptions, the first window from the right contributes about 1% of its events to the target area. It corresponds to 0.007% of all material in the target and is a completely negligible number. The contribution of the other windows that are even father away from the target is even less than that and can also be neglected.

The cut $-70cm < Vertex_Z < -48cm$ has been applied. The requirement $-70cm < Vertex_Z$ cuts out about 0.04% of the good events originating in the target. The similar requirement $Vertex_Z < -48cm$ cuts about 0.1% of the good events originated in target. The data with the combined cut $-70cm < Vertex_Z < -48cm$ lose about 0.1 % of the good electrons and have practically no window contamination.

We also have to estimate the error on the overall normalization factor that comes from the imperfections of this cut. The error in our estimate originates primarily from the assumption that the target and the window distributions are symmetrical with respect to their means and have similar shapes. A conservative estimate of this error is 50% of the corresponding loss of electrons:

$$Error_{Vertex_z} = \sqrt{0.02^2 + 0.05^2} = 0.05\%. \tag{3.3}$$

Cherenkov Cut

The Cherenkov detector has a gas such that pions do not generate light in it as described in Section 2.2.2. Nevertheless, some pions do generate a small number of photoelectrons. If we look at the distribution (Fig. 3-6) of the number of photoelectrons produced by electron candidates we will find a small peak at about 1 photoelectron associated with pions as well as a much broader electron peak centered at about 8 photoelectrons. The left side of the electron distribution can be well fitted by a function comprised of the sum of a straight line and a Gaussian. The linear dependence was used to describe the behavior of the tail of the electron distribution. A Gaussian was used to approximate the pion distribution. The CC cut has to be at about 1.5 photoelectrons in order to minimize pion contamination and minimize the loss of good electrons. We can estimate pion contamination as well as electron loss on the basis of the assumed shapes of the electron and pion distributions. The pion contamination is about 0.01%, while the electron loss is about 0.16% of the total data. We introduced an overall normalization correction $R_{CC} = 1.0016$ in order to compensate for the loss of good electrons due to this cut. The measured cross sections must be multiplied by R_{CC}:

$$\sigma^{corrected} = R_{CC} * \sigma^{raw}. \tag{3.4}$$

The assumption about the shapes of pion and electron distributions is the main contributor to the R_{CC} error. We can conservatively estimate the uncertainty in R_{CC} to be 30% of the quantity $(R_{CC} - 1)$.

$$Error_{CC} = 0.05\%. \tag{3.5}$$

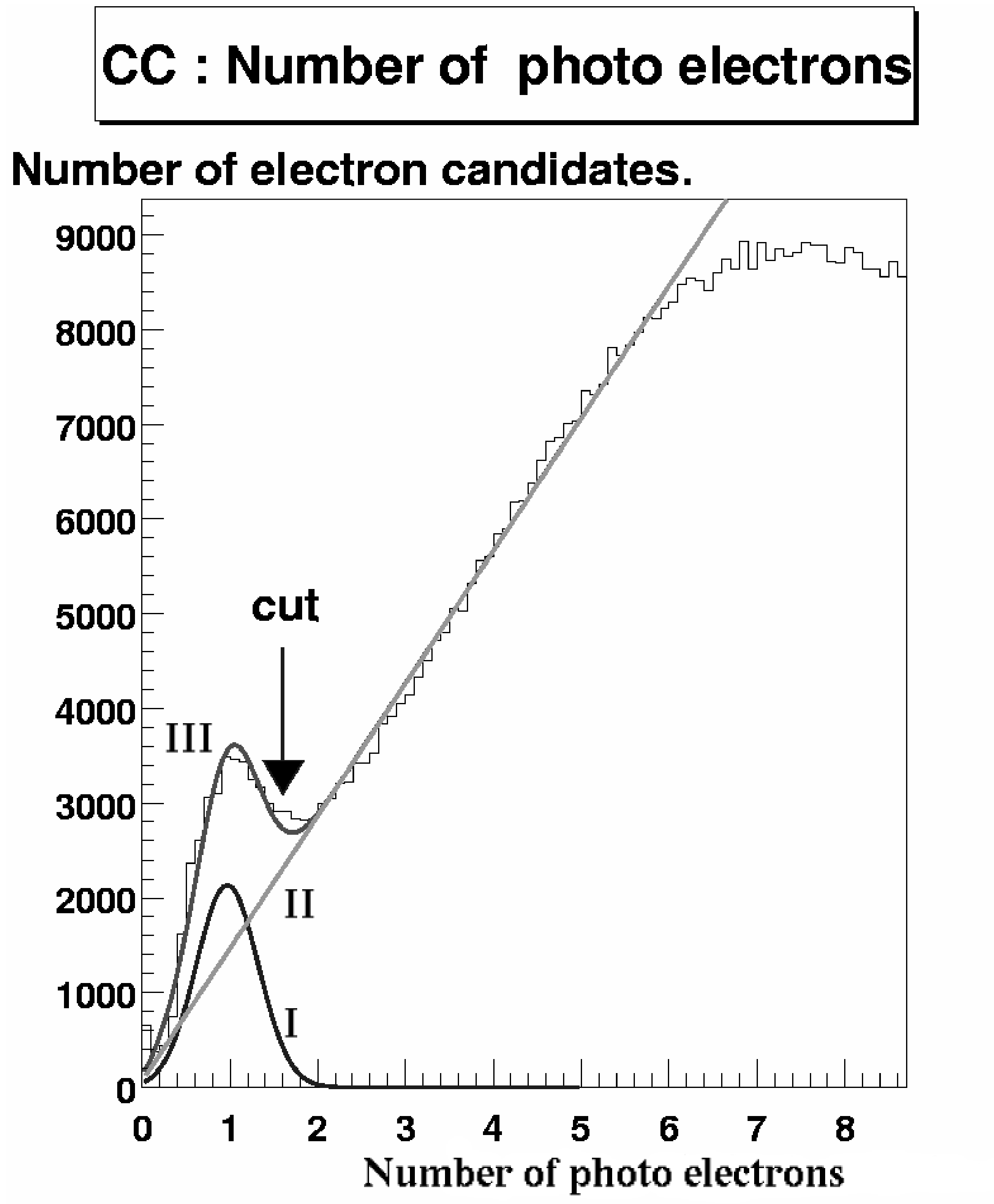

Figure 3-6: Distribution of the number of photoelectrons in the Cherenkov counter for electron candidates. The small peak on the left side of the plot is associated with pions which generate practically no light in the CC. The electrons have much broader distribution shifted to a higher number of photoelectrons. Line III is a fit to the data by a straight line plus a Gaussian. Line I is the pion contribution obtained from the fit. Line II is the electron contribution from the fit.

Electron Calorimeter Cut on Energy Deposited in the Inner Layer

The minimum ionizing pions passing through the inner layer of the calorimeter deposit energy practically independent of their momentum. The amount of the energy E_{in} deposited into the layer can be calculated from the knowledge of the layer thickness. An examination of the E_{in} distribution (Fig. 3-7) of the potential electron candidates reveals a small peak that corresponds to the above mentioned deposition energy. Naturally we have used a cut to separate electrons from the pions in that peak. We fitted the pion peak with a Gaussian and the electron tail with a second degree polynomial. The E_{in} cut value was taken to be 0.05. The pion contamination left after the cut can be estimated to be 0.05%. The estimated loss of electrons is 0.15% and the overall normalization correction is $R_{EC1} = 1.0015$. We can conservatively estimate the uncertainty in R_{EC1} to be 50% of the quantity $(R_{EC1} - 1)$.

$$Error_{EC1} = 0.07\%. \tag{3.6}$$

Cut on the EC Sampling Fraction

The plot (3-9) of the total energy deposited in the EC vs particle momentum shows two separate bands. The upper band corresponds to good electrons and the lower band corresponds to electrons that did not produce the required total energy in the EC because some of the scintillation layers failed to produce a signal. The lower band may also contain some pions since pions can produce only a small signal in the EC. We used a simple linear cut to separate these two bands:

$$E_{total} > 0.15P, \tag{3.7}$$

where P is particle momentum in GeV/c and E_{total} is the total energy deposited into EC in GeV. This cut corresponds to the cut value of 0.15 on the sampling fraction shown in Figure 3-8, where the sampling fraction is defined as the ratio of the total energy deposited in the EC and the particle momentum P. The tails of the distributions can be well fitted by exponentials. The region between small peak I on

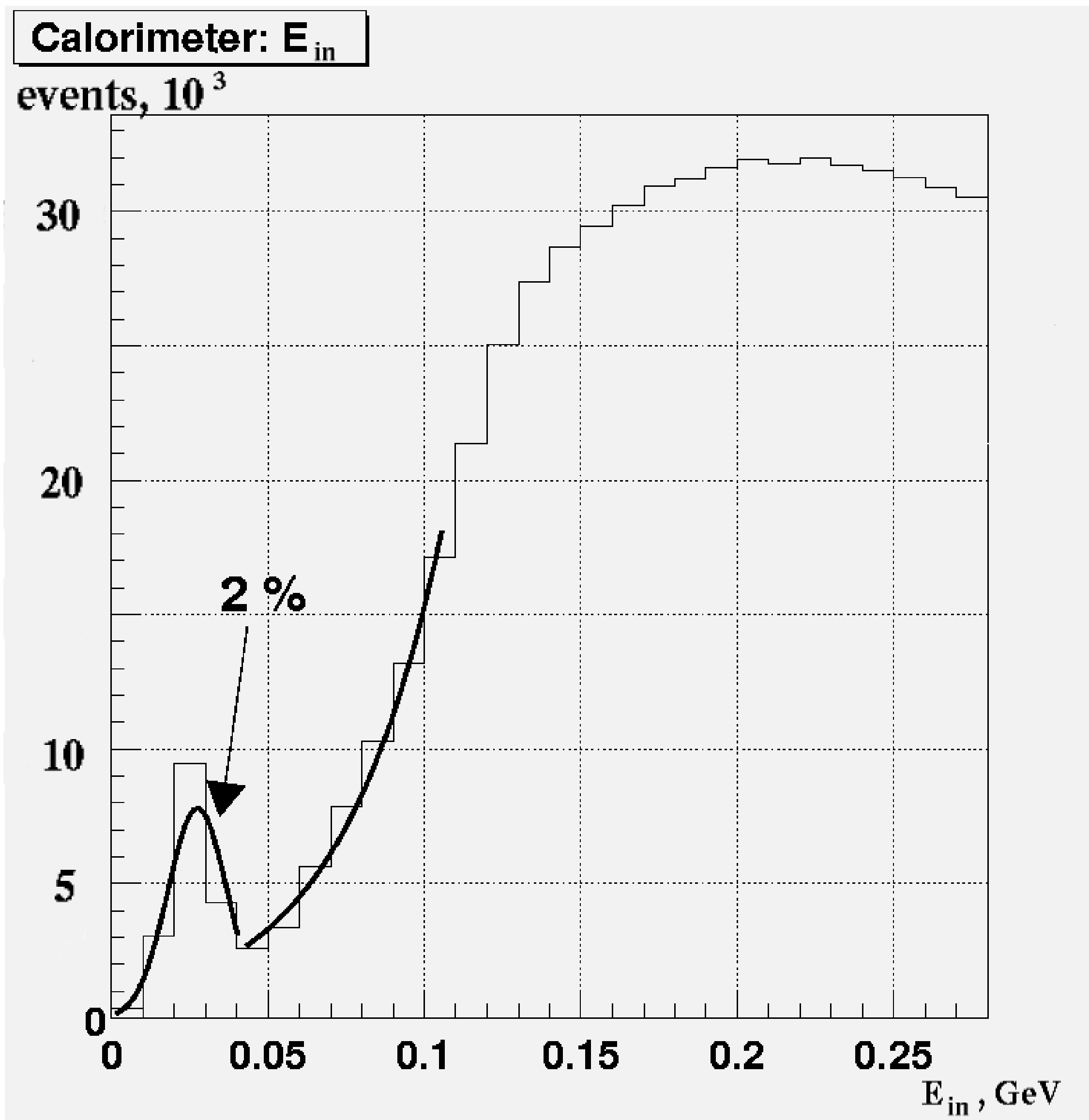

Figure 3-7: The distribution of the energy deposited by the electron candidate into the inner layer of the Electron Calorimeter. A small peak on the left is associated with pions.

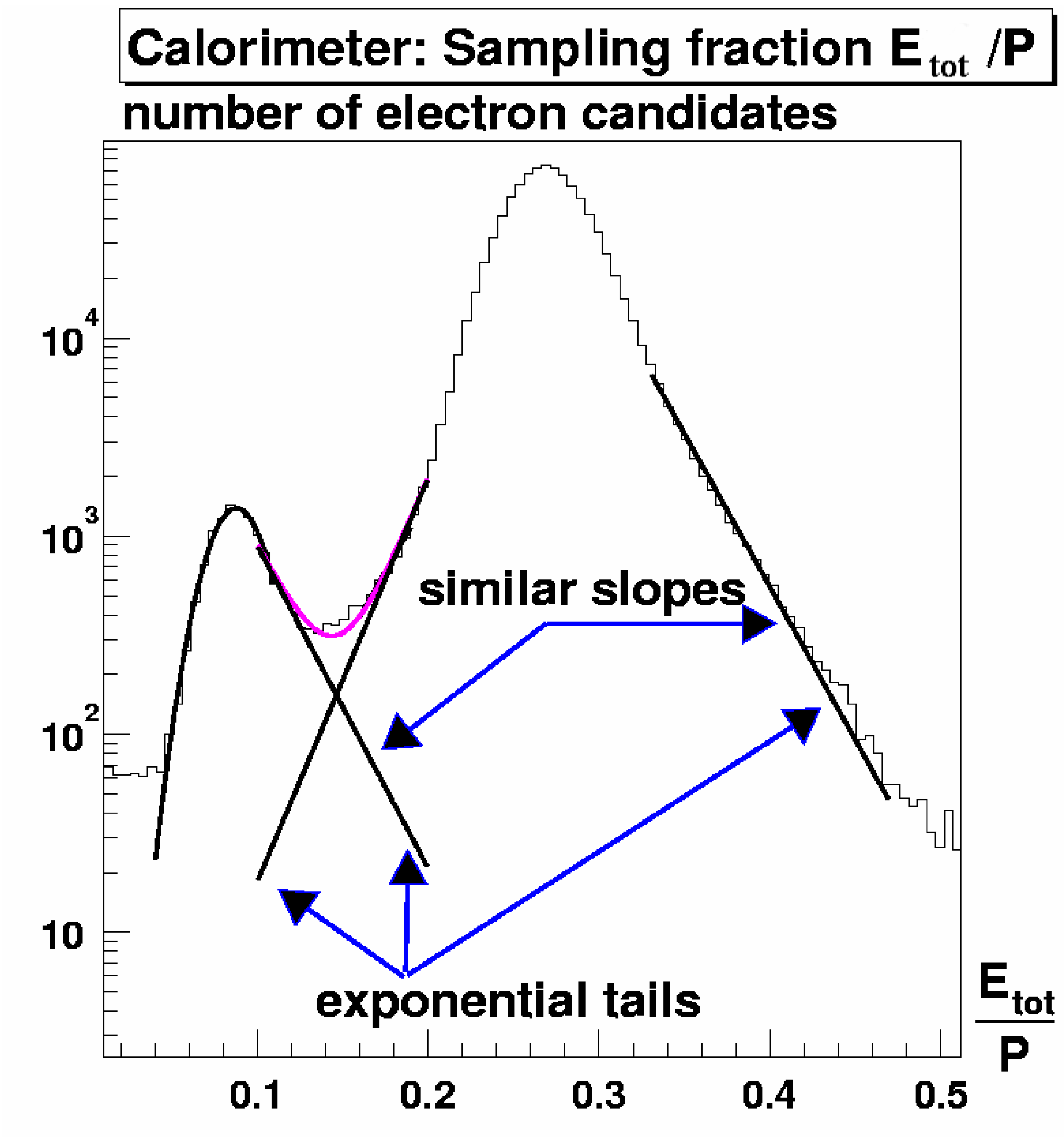

Figure 3-8: The sampling fraction for electron candidates. The small peak on the left corresponds to electrons with wrong EC energy, while the larger peak to the right corresponds to good electrons.

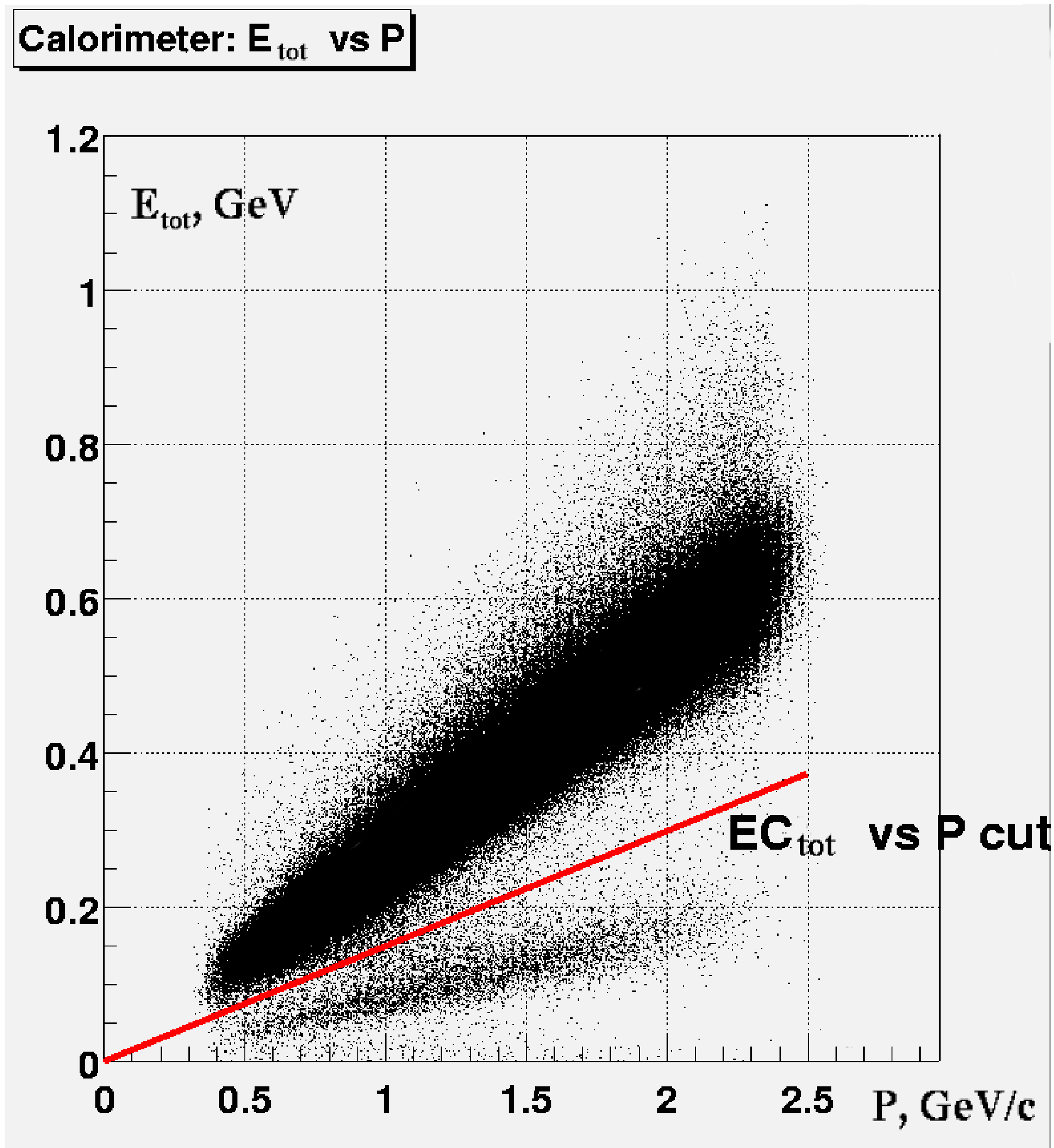

Figure 3-9: The total energy deposited by the electron candidate in Electron Calorimeter vs electron candidate momentum. The upper band corresponds to good electrons.

the left and electron peak II was fitted with the sum of two exponential tails. The slope of the peak I right tail derived from the fit has a value very similar to the value of the right slope of the electron distribution II. This suggests that the fitting procedure was reasonable. The contamination from the peak I as well as the electron loss can be estimated now. The contamination is 0.081%, while the electron loss is 0.078%. The correction factor for the overall normalization has to be $R_{EC2} = 1.00078$. The main contributor to the uncertainty in R_{EC2} is the assumption about the exponential nature of the tails. We can conservatively take Err_{EC2} to be 100% of the quantity $(R_{EC2} - 1)$: $Err_{EC2} = 0.08\%$. If we assume the worst case that all events in the peak I are good electrons then we can estimate the systematic error as the number of events in the peak I.

$$Error_{EC2} = 1.5\%. \tag{3.8}$$

This is our final EC error.

EC E_{total} vs E_{inner} cut

Due to reconstruction problems, a small number of events had a total energy E_{total} deposited into the calorimeter less than the energy E_{inner} deposited into the inner layer. The additional cut $E_{total} \geq E_{inner}$ was used as shown in Figure 3-10. It eliminates 0.053% of the data. We can take the normalization error associated with this cut to be 100% of the above value

$$Error_{E_{total}E_{inner}} = 0.053\%. \tag{3.9}$$

3.2.4 Electron Momentum Correction

Due to the fact that the CLAS magnetic field was not known exactly, reconstruction of the particle momentum from the track inside the drift chambers resulted in a small error. Since CLAS has the ability to measure different channels at the same time, we can use the well known elastic scattering kinematics to determine the needed

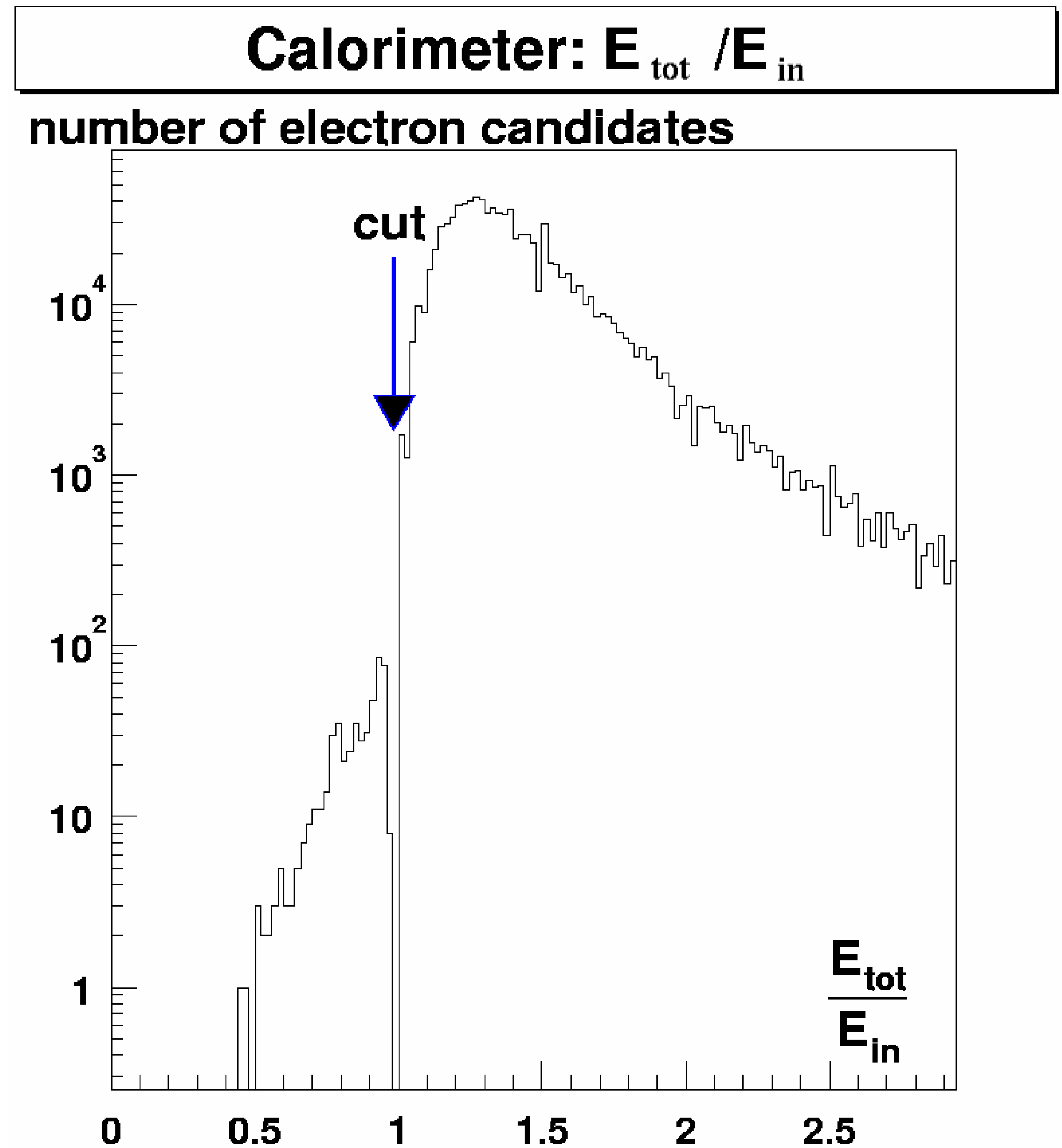

Figure 3-10: The ratio of the total energy deposited into the calorimeter and the energy deposited into the inner layer. Due to reconstruction problems a small number of events had a total energy E_{total} deposited into the calorimeter less than the energy E_{inner} deposited into the inner layer.

momentum correction. The correction should be a function of the strength of the CLAS magnetic field, the particle momentum and the scattering angle. An empirical expression has been used to fit the data in such a way that the W distribution had the elastic peak centered exactly at the proton mass $M_p = 0.938 GeV$. Each sector has been fitted independently with its own set of coefficients. The resulting correction was usually less than 1% of the electron momentum and provided much better agreement and alignment of different sectors. In a typical case the elastic peak could be shifted by 20 MeV before correction. The correction centers the elastic peak at the correct value 938 MeV. The width of the elastic peak calculated using all the sectors improves from 23 to 16 MeV when this correction is applied.

3.2.5 Data Acquisition Live Time

During data taking, not all events available for recording were actually recorded. Because of computer dead time some events have been disregarded. This situation is described by the relations:

$$N_r = N \frac{T_{live}}{T}, \tag{3.10}$$

$$T = T_{live} + T_{dead}, \tag{3.11}$$

where N_r is the number of actual events recorded, N is the number of events that were generated, $T_{live}(T_{dead})$ is the duration of time when the Data Acquisition System was (was not) able to record events. The average live time during data taking was more than 90% ($\frac{T_{live}}{T} > 0.9$). In order to extract a cross section from the number of events a corresponding correction $k_{live} = \frac{T}{T_{live}}$ (Eq. 3.10) of about several percent has to be made to the recorded number N_r.

When the corrections are small, it is natural to expect that the dead time is an increasing linear function of the data rate since dead time results from the inability of the computer to process large volumes of data in a short period of time. Accordingly,

$$k_{live} = a + bN_{trig}, \tag{3.12}$$

where N_{trig} is the number of recorded triggers and a and b are linear coefficients determined by a fit to the data. Using a gated and an ungated clock we can determine the data acquisition live time since the gated clock is counting only when data acquisition is "live," while the ungated clock is always counting. By taking the ratio of the gated to the ungated clock we obtain the needed live time correction $k_{live} = \frac{T}{T_{live}}$.

Once the live time is known we can correct the yield by multiplying it by k_{live}. During data taking we did not have gated scalers that contained information about the beam helicity. The gated clock information was read out only every 10 seconds while the helicity was changing every second. Because of the different trigger rates for positive and negative beam helicities, it is possible to have different dead time corrections for plus and minus helicity.

We have studied the dead time as a function of the trigger rate by comparing the ratio of gated to ungated clocks to the total number of triggers we get every 10 seconds. A linear fit (Eq. 3.12) can be used to determine coefficients for each distinct set of runs [77]. We then applied the correction k_{live} to each helicity pulse based on the number of triggers during a 1 sec pulse. This is an important correction since our results show that the difference in trigger rates could result in a false asymmetry which can be as large as 15% of the original asymmetry measured by the Faraday Cup.

3.2.6 Elastic Cross Section

The inclusive electron scattering cross section may be written [5], [6]:

$$\frac{d\sigma}{d\Omega} = \Sigma + h * \Delta. \tag{3.13}$$

It contains helicity-sum and helicity-difference contributions, respectively,

$$\Sigma = \frac{1}{2}\left(\frac{d\sigma^{\uparrow\uparrow}}{d\Omega} + \frac{d\sigma^{\uparrow\downarrow}}{d\Omega}\right), \tag{3.14}$$

and

$$\Delta = \frac{1}{2}\left(\frac{d\sigma^{\uparrow\uparrow}}{d\Omega} - \frac{d\sigma^{\uparrow\downarrow}}{d\Omega}\right). \tag{3.15}$$

In Equation (3.13), h is a product of beam and target polarizations,

$$h = P_{beam} * P_{target}. \tag{3.16}$$

In the case of elastic scattering:

$$\Sigma = \sigma_M \frac{E'}{E}\frac{1}{(1+\tau)\epsilon}\left(\epsilon G_E^2 + \tau G_M^2\right), \tag{3.17}$$

and

$$\Delta = -h\sigma_M \frac{E'}{E}\frac{1}{(1+\tau)\epsilon}\left(\sqrt{1-\epsilon^2}cos\Theta_\gamma \tau G_M^2 + \sqrt{\epsilon(1-\epsilon)}sin\Theta_\gamma \sqrt{2\tau}G_E G_M\right). \tag{3.18}$$

The Mott cross section is:

$$\sigma_M = \frac{\alpha^2(hc)^2}{4(2\pi)^2E^2}\left(\frac{cos^2\frac{\Theta}{2}}{sin^4\frac{\Theta}{2}}\right). \tag{3.19}$$

Using existing data, the elastic form factors can be parameterized and we present here different parameterizations.

1) Dipole parameterization

$$G_E^d = \frac{1}{1+\frac{Q^2}{0.71}}, \tag{3.20}$$

$$G_M^d = \mu G_E = 2.79 G_E. \tag{3.21}$$

2) Bosted parameterization [70]

$$G_M^b = \frac{\mu}{1 + 0.35q + 2.44q^2 + 0.5q^3 + 1.04q^4 + 0.34q^5}, \tag{3.22}$$

$$G_E^b = \frac{1}{1 + 0.62q + 0.68q^2 + 2.8q^3 + 0.83q^4}, \tag{3.23}$$

where $q = \sqrt{Q^2}$.

3) Combined parameterization

$$G_M^c = \frac{\mu}{1 + 0.35q + 2.44q^2 + 0.5q^3 + 1.04q^4 + 0.34q^5}, \tag{3.24}$$

$$G_E^c = G_M/\mu. \tag{3.25}$$

4) Parameterization using recent $\frac{G_E}{G_M}$ results from JLab [71]

$$G_M^A = G_M^b, \tag{3.26}$$

$$G_E^A = \frac{G_M^A}{\mu}(1 - 0.14(Q^2 - 0.3)). \tag{3.27}$$

3.2.7 Cross Section Calculation

The number of events in the kinematic bin dK (dK can be dQ^2 or dQ^2dW or a similar expression depending on the variables used) is

$$N_{dK} = \frac{\int Idt}{e}\frac{N_A}{A}\rho L\left(\frac{d\sigma}{dK}\right)dK, \tag{3.28}$$

where ρ, A, L are respectively the target density, atomic number and length. The electron charge is $e = 1.602 * 10^{-19} Coulomb$, and Avogadro's number is $N_A = 6.02 * 10^{23} mol^{-1}$. The target material was a collection of small round pellets tightly packed together. The length of the target L has to take into account the packing fraction P_f of the material. P_f is a number from 0 to 1 and characterizes how compactly the pellets were packed in the target cell.

$$L = L_{physical} P_f = 1cm * 0.58 = 0.58cm. \tag{3.29}$$

The density of the pellets is

$$\rho_{NH_3} = 0.97 \left[\frac{g}{cm^3}\right]. \tag{3.30}$$

If only free hydrogen atoms participate in the reaction, the cross section per hydrogen atom in Equation (3.28) will include the combination

$$\frac{\rho_{NH_3}}{A_{NH_3}} \rightarrow \frac{\rho_{NH_3}}{A_{NH_3}} * 3 \tag{3.31}$$

because we have 3 hydrogen atoms per NH_3 molecule.

The accumulated charge is

$$\int I dt = 10^{-10} N_{FCup} \left[C\right], \tag{3.32}$$

where N_{FCup} is the number of Faraday Cup counts. Each count corresponds to $10^{-10} Coulomb$.

Finally, for the proton cross section

$$\left(\frac{d\sigma}{dK}\right) = \frac{N_{dK}}{dK} \frac{e[C]}{10^{-10} N_{FCup}[C]} \frac{A_{NH_3}}{3} \frac{1}{N_A \rho_{NH_3} L} = \tag{3.33}$$

$$= \frac{N_{dK}}{dK} \frac{1.602 * 10^{-19}[C]}{N_{FCup} 10^{-10}[C]} \left(\frac{18}{3}\right) \frac{1}{6.02 * 10^{23}[g^{-1}] * 0.97 \left[\frac{g}{cm^3}\right] 0.58[cm]}, \tag{3.34}$$

$$\left(\frac{d\sigma}{dK}\right) = \frac{N_{dK}}{dK N_{FCup}} 2.838 * 10^{-2} [\mu Bn], \tag{3.35}$$

where $1\mu Bn = 10^{-30} cm^2$.

3.2.8 Normalization Using Elastic Scattering

The data obtained in our experiment allow us to calculate polarized cross section differences $\frac{d\sigma^{\downarrow\uparrow}}{d\Omega dE'} - \frac{d\sigma^{\uparrow\uparrow}}{d\Omega dE'}$ as in equation (1.37). This cross section difference includes only events from hydrogen, since the nitrogen in the NH_3 target is not polarized. The ratio N_{norm} of the number of the events under the elastic peak (Figure 3-11) to the cross section calculated from formfactors (as in Section 3.2.6) is given by:

$$N_{norm} = P_b P_t f_{eff}, \tag{3.36}$$

where f_{eff} is the CLAS efficiency for detecting electrons.

In our analysis we have been using only very efficient regions of CLAS, and therefore f_{eff} cannot be less than one by more than several percent. $P_b P_t$, on the other hand, has to be about 0.4. We are not able to determine $P_b P_t$ and f_{eff} independently, but for the calculation of cross section it is enough to know the product $N_{norm} = P_b P_t f_{eff}$.

3.2.9 Radiative Corrections for Elastic Scattering

In order to obtain a normalization factor for our data, the events N_{el} that correspond to elastic scattering were integrated from $W_{min} = 0.75 GeV$ up to $W_{max} = 1.058 GeV$ around the elastic peak, as shown in Figure 3-11. These data have to be compared with the elastic cross section calculated from the known elastic form factors. Unfortunately, because of the radiative effects, some elastic events are shifted to values of W higher than W_{max} and are not included in the integral N_{el}. The correction factor K^{el}_{rad} has to be applied to N_{el} before comparison with calculations based on formfactors. This correction factor compensates for the elastic electrons that have $W > W_{max}$. The radiative correction for elastic electron scattering was calculated using equation II.6 of Mo and Tsai [73], [78]. $K^{el}_{rad} = 1.22$ for the beam energy $2.562 GeV$ and Q^2 values between 0.2 and $2.3 GeV$. The target thickness is 0.023

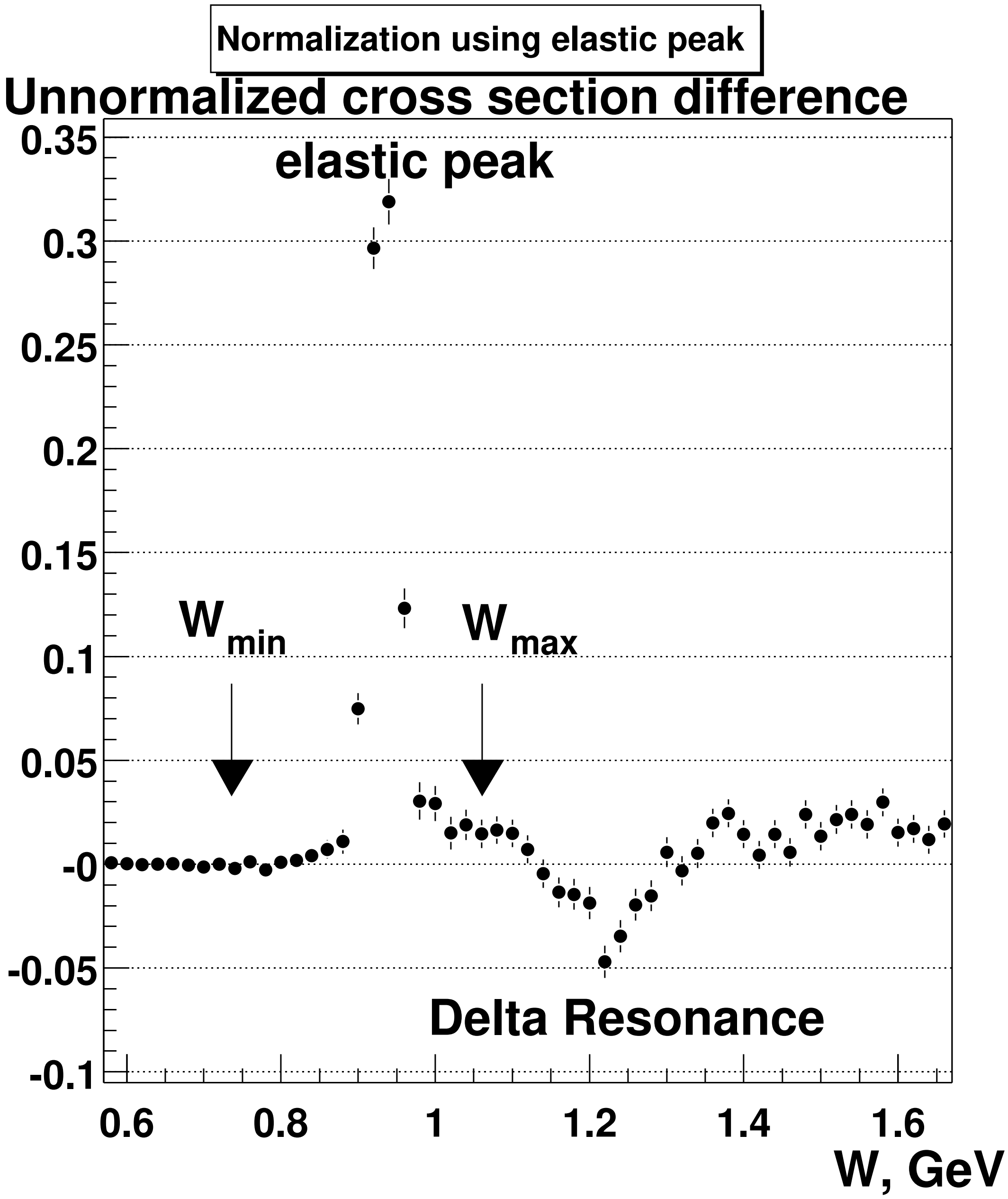

Figure 3-11: Elastic scattering is used to normalize data. The unnormalized data need an overall normalization coefficient $1/N_{norm}$ to be equal to the cross section difference $\sigma^{\downarrow\uparrow} - \sigma^{\uparrow\uparrow}$ defined in Section 1.3.3. The data integrated from W_{min} to W_{max} are compared to the elastic cross section calculated from well known elastic formfactors (Section 3.2.6). As discussed in Section 3.2.8, the ratio of data to calculation provides the needed normalization factor N_{norm}. The beam energy $E = 2.6\ GeV$, $Q^2 = 0.26$ GeV^2.

radiation length. $K^{el}_{rad} = 1.37$ for the beam energy $4.278GeV$ and Q^2 values between 0.55 and $2.3GeV$. The deviation of K^{el}_{rad} from its average value within corresponding Q^2 band is approximately 1% for both energies.

3.2.10 Radiative Corrections for Inelastic Scattering

The code used for making radiative corrections in the inelastic region was based on the radiative corrections code "RCSLACPOL" used at SLAC [75], [79], [80]. The code uses methods developed by Shumeiko, Kuchto [74], and Tsai [38]. The additive correction applied to the data of our experiment is

$$\delta\sigma(W, Q^2) = \sigma_{Born}(W, Q^2) - \sigma_{rad}(W, Q^2), \tag{3.37}$$

where $\sigma_{Born}(W, Q^2)$ is the Born cross section. The code uses this Born cross section to produce radiated cross section $\sigma_{rad}(W, Q^2)$. The model for the Born cross section needed for these calculations was taken from the "Models" program described in Section 3.2.11.

3.2.11 Models

Extraction of the GDH integral requires knowledge of several quantities that were not directly measured in our experiment. Some of these quantities have been measured in other experiments but some are not well known and require models in order to be estimated. The unpolarized structure functions F_1, F_2 and polarized structure functions g_1, g_2 are not known in the entire kinematic region. The g_2 polarized structure function is needed in our analysis in order to extract g_1 from the experimental data. The g_1 polarized structure function in the DIS region is needed for the estimation of the complete GDH integral, since in our experiment it is measured only in the resonance region. We use the model contained in the program for the SLAC experiment E155 radiative corrections [75]. This program called "Models" was modified by incorporating the present world data for F_1, F_2, g_1, g_2. A fit of the world data with smooth functions under several theoretical constrains was used to predict the structure functions for all values of W and Q^2 [40], [41]. Theoretical constraints such as the Soffer positivity limit [76], the Burkhardt-Cottingham Sum Rule [46] and MAID2000 were used. As mentioned earlier, this program was also used in the calculation of the radiative corrections. The result for the g_1 polarized structure function is plotted in Figure 3-12. Figure 3-13 shows the contribution of g_1 to the GDH integral at different values of W. In the GDH integral, kinematic factors suppress the contribution from high W. Thus the model dependence is considerably reduced as shown by a comparison of Figures 3-13 and 3-12.

3.3 Systematic Error Evaluation

3.3.1 The Systematic Errors in the CLAS Efficiency

Only high efficiency kinematic regions have been used for the data analysis as described in Section 3.2.2. The normalization to elastic scattering (Section 3.2.8) eliminates the average CLAS inefficiency. Elastic scattering corresponds to the invariant mass $W = M_p$ where M_p is the proton mass. Therefore inefficiencies that vary as a function of W can not be completely eliminated by the normalization to elastic scattering. The contribution of these inefficiencies to the systematic error is estimated below.

The CLAS inefficiency for a given electron is a function of the electron momentum p, scattered angles θ, ϕ and the strength of the CLAS magnetic field B.

$$F_{in} = F_{in}(p, \theta, \phi, B). \tag{3.38}$$

The inclusive cross section is independent of the azimuthal angle ϕ, so we are interested only in F_{in} averaged over the ϕ angle. This averaged inefficiency function $f_{in}(p, \theta, B)$ can be viewed as a function of the invariant mass W and Q^2:

$$f_{in} = f_{in}(W, Q^2, B). \tag{3.39}$$

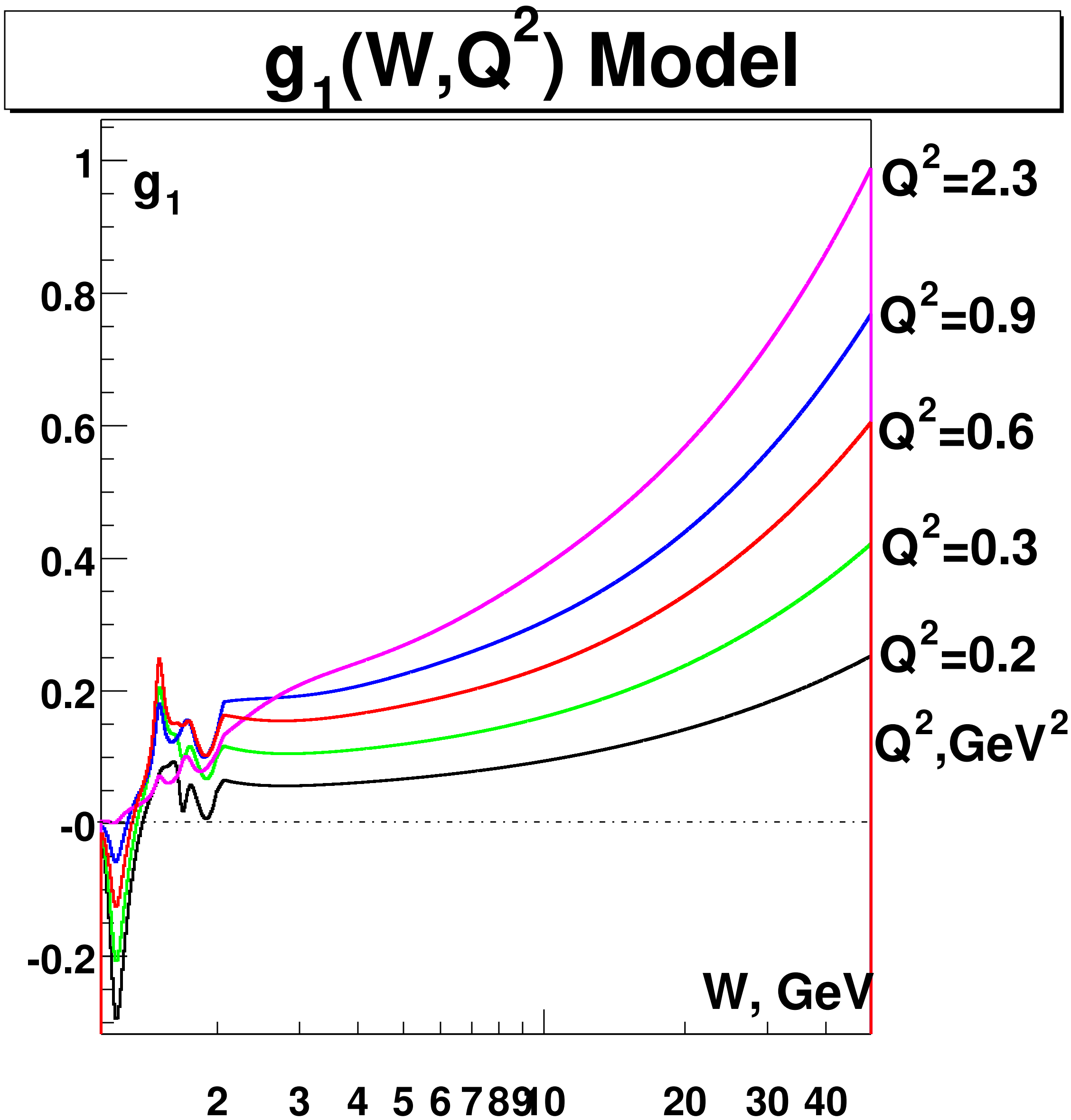

Figure 3-12: The model for $g_1(W, Q^2)$.

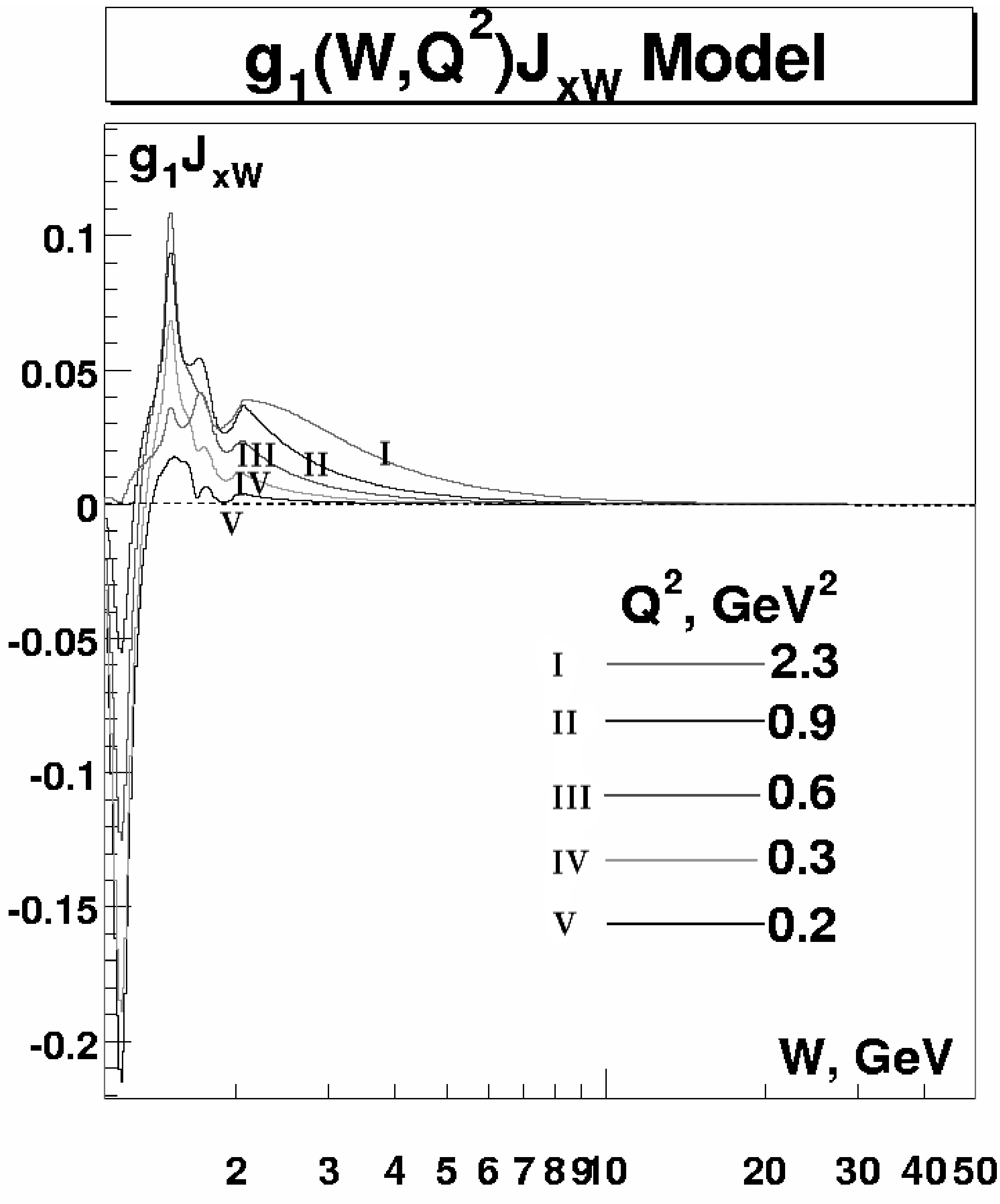

Figure 3-13: The model for $g_1(W, Q^2)$ is multiplied by the Jacobian $J_{xW}(W, Q^2)$ to obtain the integrand of the generalized GDH integral. The Jacobian J_{xW} suppresses the contribution of the high W part of the polarized structure function $g_1(W, Q^2)$ in the GDH integral (compare with Figure 3-12).

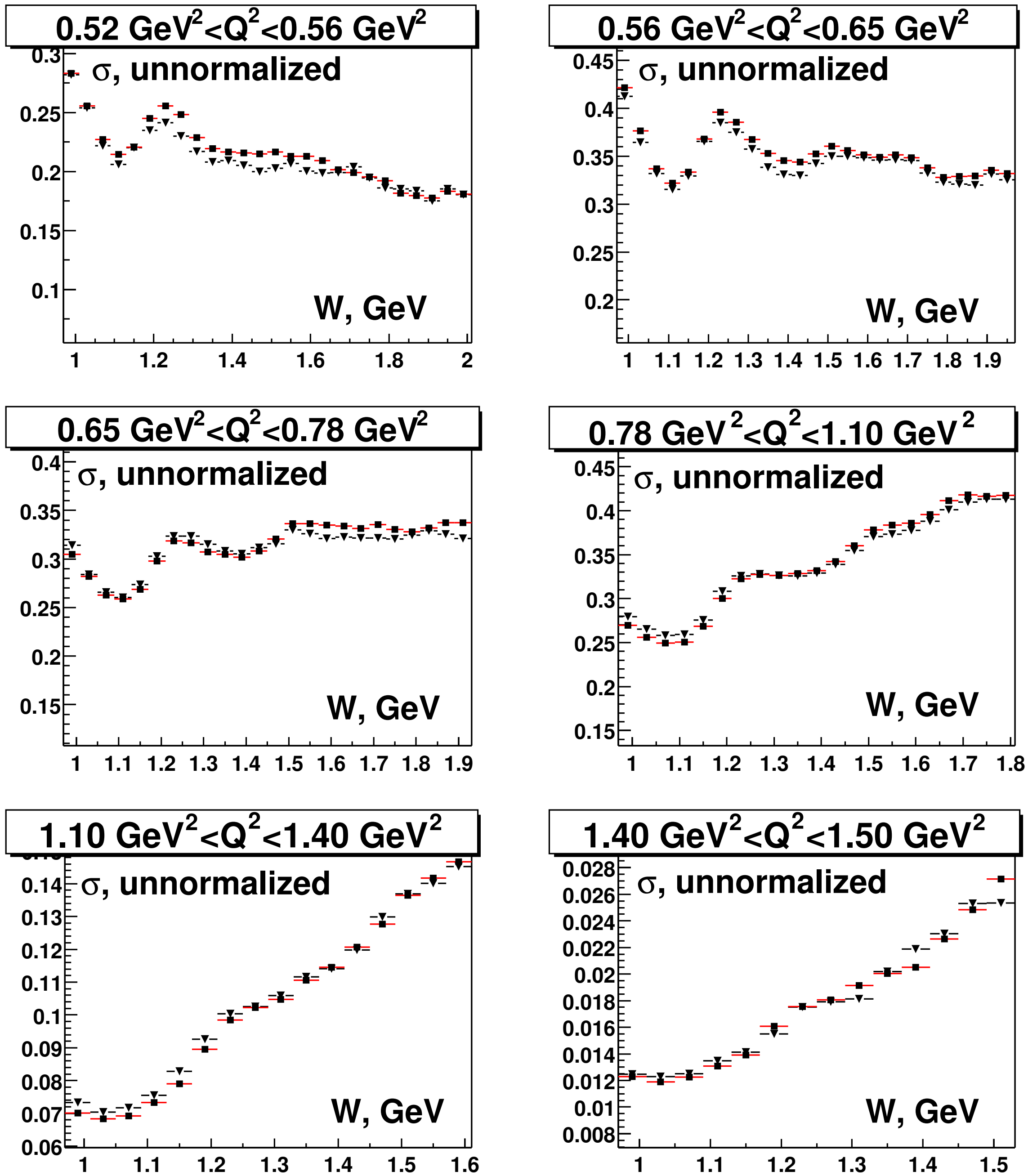

Figure 3-14: The NH_3 unpolarized inclusive cross section $\sigma(W, Q^2)$ is calculated from the data with different CLAS magnetic fields. The magnetic field for the black triangles is 60% of the magnetic field for the black squares. In order to represent a cross section, the data shown above have to be multiplied by an unknown overall normalization constant which is the same for all Q^2. The electron beam energy is $E = 2.6\ GeV$. The errors are statistical only.

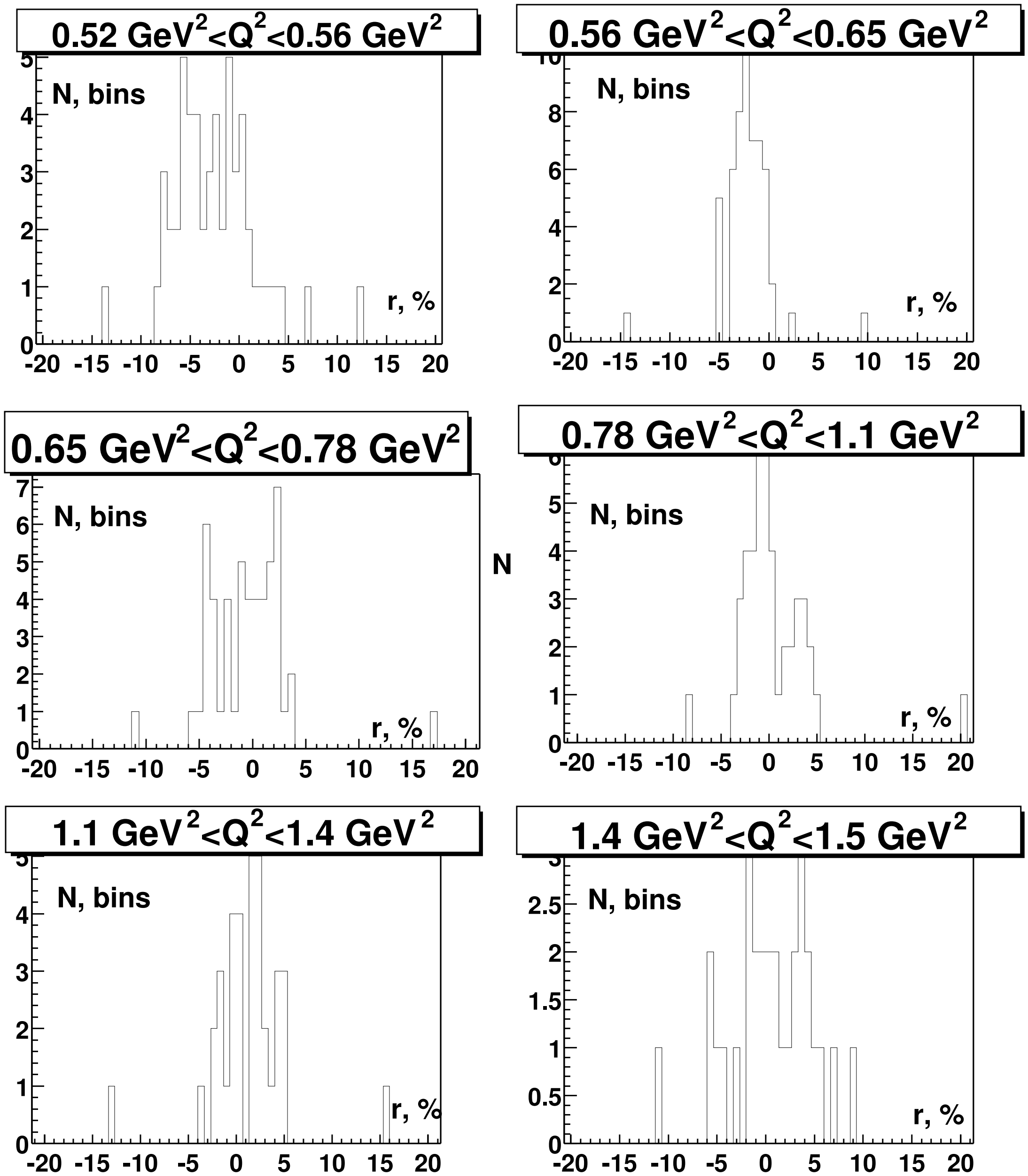

Figure 3-15: The histograms shown in Fig. 3-14 are cross sections binned in W. For each W bin the value of $r = 2\frac{\sigma_1-\sigma_2}{\sigma_1+\sigma_2}$ has been calculated. This figure shows the distribution of the calculated r's. σ_1 and σ_2 are the cross sections calculated by two different methods as described in Section 3.3.1 and plotted in Fig. 3-14. The number of bins, N, for a given value of r is the number of bins from Fig. 3-14 that have that value of r.

.

Experiments were done using different values of the CLAS magnetic field. The electrons with the same W and Q^2, traveling in different magnetic fields pass through different parts of CLAS and have different efficiencies of being detected. Therefore experiments with different magnetic fields have different efficiencies. The different magnetic fields effectively map the same particles to different places in the CLAS inefficiency distribution. Any difference in the electron cross sections calculated from the data with different magnetic fields will be due to variations of f_{in}, provided all the other experimental conditions are the same. This difference is a direct estimate of the systematic error associated with the CLAS inefficiency for the particular (W, Q^2) bin.

Figure (3-14) shows unpolarized inclusive NH_3 cross sections for different CLAS magnetic fields. The difference is due to variation of the CLAS inefficiency. As can be seen from the plot, the difference is usually within 10% of the cross section value. This quantity can be taken as an estimate of the systematic error associated with the CLAS inefficiency.

For each Q^2 we define the relative cross section difference calculated from different data sets for fixed i bin in W as r_i:

$$r_i = 2\frac{\sigma_{1i} - \sigma_{2i}}{\sigma_{1i} + \sigma_{2i}}. \tag{3.40}$$

The distribution of r is shown in Figure 3-15. The systematic error in CLAS inefficiency is equal to the width of this distribution. It is estimated to be

$$Error_{inef} = \sqrt{\frac{\Sigma r_i^2}{N_{bins}}}. \tag{3.41}$$

where N_{bins} is a number of bins in W used for analysis from Figure 3-14. The calculations show that $Error_{inef}$ is less than 5% for each Q^2 bin used in the analysis:

$$Error_{inef} = 5\%. \tag{3.42}$$

A different method can be used to evaluate the same inefficiencies. For a given value of W and Q^2 the cross section calculated from the data obtained from different CLAS sectors should be the same since the inclusive cross section is independent of the azimuthal angle ϕ. Figure 3-16 shows the cross section calculated using the first 3 CLAS sectors , the last 3 sectors and all 6 sectors. For a given value of W and Q^2 the difference is due to variation of the efficiency from sector to sector.

For each Q^2 we define the relative cross section difference calculated using different CLAS sectors for fixed i bin in W as r_i:

$$r_i = 2\frac{\sigma_{1i} - \sigma_{2i}}{\sigma_{1i} + \sigma_{2i}}, \tag{3.43}$$

where σ_{1i}, σ_{2i} are the cross sections from the first 3 and the last 3 CLAS sectors.

The systematic error in the CLAS inefficiency is equal to the width of the r distribution. It is estimated to be

$$Error_{\frac{1}{2}CLAS} = \sqrt{\frac{\Sigma r_i^2}{N_{bins}}} \tag{3.44}$$

where N_{bins} is a number of bins in W used for analysis from Figure 3-16. The subscript "$\frac{1}{2}CLAS$" indicates that $Error_{\frac{1}{2}CLAS}$ is the inefficiency of CLAS if only half of it is used (three sectors out of six):

$$Error_{\frac{1}{2}CLAS} = 7\%. \tag{3.45}$$

$Error_{\frac{1}{2}CLAS}$ is a systematic error in the CLAS inefficiency for the cross section calculated on the basis of the first 3 or the last 3 sectors. This error originates, for example, from the broken SC paddles or the missing Drift Chamber wires in some sectors. The cross section for the experiment is an average of the cross sections σ_1 and σ_2 of the two $\frac{1}{2}$ portions of CLAS:

$$\sigma_i = \frac{1}{2}(\sigma_{1i} + \sigma_{2i}). \tag{3.46}$$

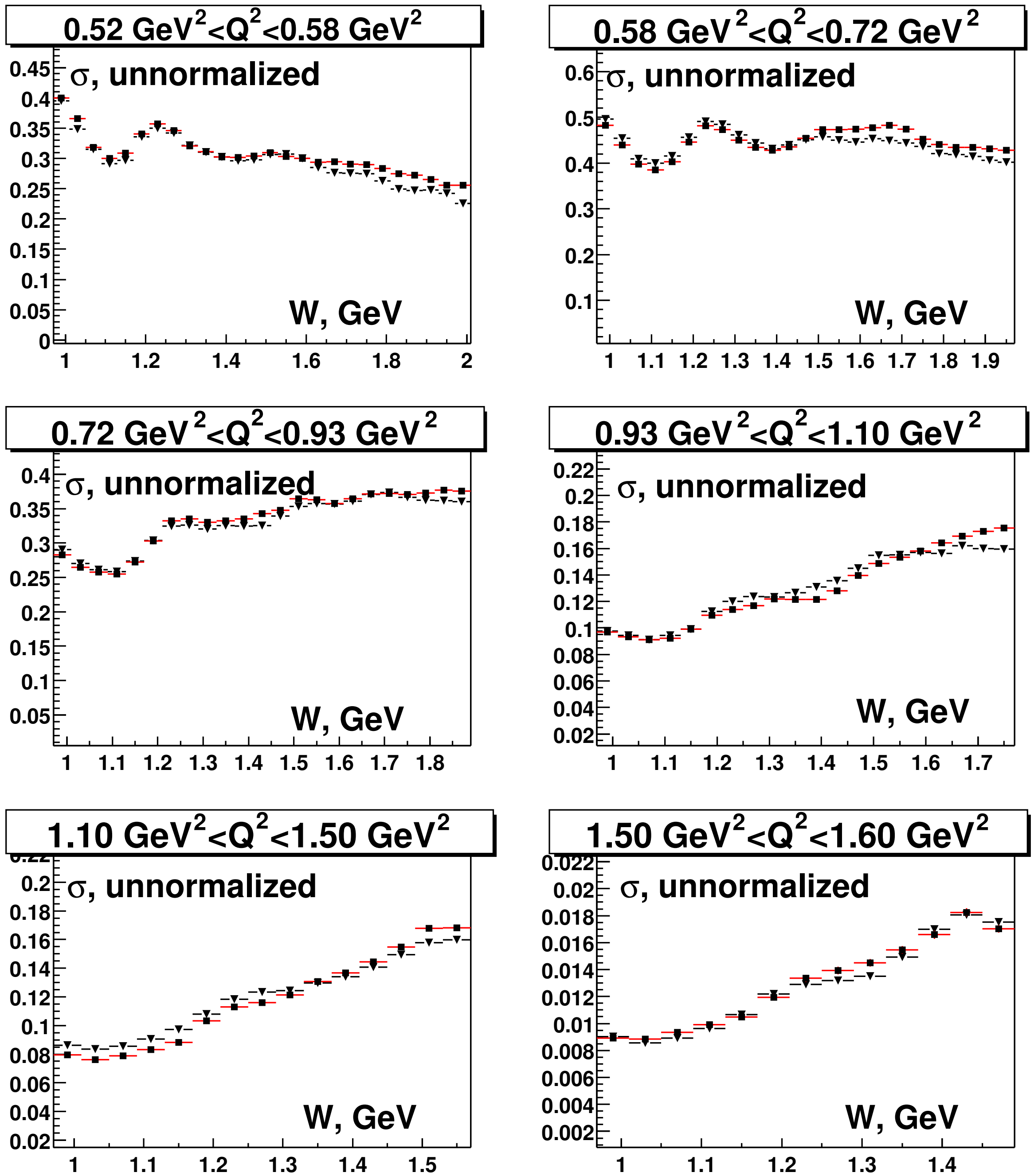

Figure 3-16: The NH_3 unpolarized inclusive cross section, $\sigma(W, Q^2)$, is calculated from the data using three sectors of CLAS. The squares correspond to the first 3 sectors, the triangles to the last 3 sectors. We denote these cross sections as σ_1 and σ_2 respectively. In order to represent a cross section, the data shown above have to be multiplied by an unknown overall normalization constant which is the same for all Q^2. The electron beam energy is $E = 2.6\ GeV$. The errors are statistical only.

The average errors of σ_{1i} and σ_{2i} were estimated to be

$$Error_{\sigma_1 \frac{1}{2}CLAS} = Error_{\sigma_2 \frac{1}{2}CLAS} = Error_{\frac{1}{2}CLAS}, \tag{3.47}$$

where $Error_{\frac{1}{2}CLAS}$ is from Eq. (3.45).

The Drift Chambers, SC paddles and other hardware from different sectors are independent, and therefore $Error_{\sigma_1 \frac{1}{2}CLAS}$ and $Error_{\sigma_2 \frac{1}{2}CLAS}$ are independent and should be added in quadrature to form the error $Error_{inef}$ of the σ_i defined in Eq. (3.46).

$$Error_{inef} = \frac{1}{2}\sqrt{Error^2_{\sigma_1 \frac{1}{2}CLAS} + Error^2_{\sigma_2 \frac{1}{2}CLAS}} = \frac{1}{\sqrt{2}} Error_{\frac{1}{2}CLAS} = \frac{7\%}{\sqrt{2}} = 5\%, \tag{3.48}$$

where $\frac{1}{2}$ comes from Eq. (3.46) and reflects the fact that the errors have to be averaged.

The two independent estimates shown in equations (3.42) and (3.48) produce the same value.

3.3.2 Systematic Errors from Particle Identification (PID)

The errors resulting from electron misidentification were discussed in Section 3.2.3. The total error can be taken to be

$$Error_{PID} = 2\%. \tag{3.49}$$

3.3.3 ^{15}N Polarization

Our experiment used a $^{15}NH_3$ target. In the analysis we have assumed that ^{15}N is not polarized. We will justify this approach and calculate the associated systematic error. Based on data [67] the empirical polynomial dependence between proton and ^{15}N polarizations has been derived [67], [68], [69]

$$P_{15} = -(0.136P_p - 0.183P_p^2 + 0.335P_p^3). \tag{3.50}$$

We operated the target under similar conditions, therefore, we should have the same relationship. The 50% average proton polarization, P_p, corresponds to nitrogen polarization, $P_{15} = -7\%$. This polarization results in the correction factor $C_{^{15}N}$ to the raw asymmetry [68], [69]:

$$C_{^{15}N} = 1 - \frac{1}{9}\frac{P_{^{15}N}}{P_p} g_{^{15}N}, \tag{3.51}$$

where $g_{^{15}N}$ is a correction for the European Muon Collaboration(EMC) effect [11] which is about unity for our case. Substitution of proton and nitrogen polarizations in the above equation results in

$$C_{^{15}N} = 1.015. \tag{3.52}$$

Thus the systematic error due to nitrogen polarization can be estimated to be 1.5%.

$$Error_{^{15}N} = 0.015 \tag{3.53}$$

3.3.4 The Electroweak Interaction

Along with the single photon exchange process (Fig. 1-2) the inclusive cross section (Fig. 1-2) has electroweak processes that contain intermediate W and Z bosons. These processes can contribute to polarization asymmetries and cross section differences. Our experiment was conducted at very moderate values of Q^2 where the contribution of electroweak interactions is small. The propagation of W and Z bosons is suppressed by the factor $P^2_{w,z}$, where $P_{w,z}$ is the propagator of the $W(Z)$ boson. The cross section will be suppressed by the factor k_{weak}

$$k_{weak} \sim \frac{P^2\gamma}{P^2_{w,z}} \sim \frac{Q^4}{(M^2_{W,Z} + Q^2)^2} \sim \frac{Q^4}{M^4_{W,Z}} \tag{3.54}$$

compared to the single photon exchange. $P\gamma$ is a photon propagator. The boson masses are $M_W = 80GeV, M_Z = 91GeV$. The resulting $k_{weak} \sim 10^{-7}$. This estimation shows that electroweak corrections in our experiment are negligible.

3.3.5 The Faraday Cup Normalization

The electron beam current I was monitored using a Faraday Cup. The helicity of the beam was changed with the frequency of $1Hz$. After each pulse with a given helicity the next pulse has 50% probability to be of the same helicity and 50% probability to be of the opposite helicity. This process we call the randomization of the helicity. The Faraday Cup starts counting at the beginning of each helicity pulse and stops at the end. The rate of counting is proportional to the electron current with the proportionality constant k_{FC}.

$$N_{counts} = k_{FC} I, \tag{3.55}$$

$$k_{FC} = 10 \frac{counts/sec}{nA}. \tag{3.56}$$

The Faraday Cup error for each helicity pulse, $Error_{1pulse}$, is 1 count or $0.1 nA * sec$ because counting is discrete. Thus the average current of $2nA$ has an error of 5% which is actually larger than the measured polarization asymmetries. The averaging over all helicity pulses reduces this systematic error $Error_{FC}$ substantially. To estimate the systematic error we will assume that Faraday Cup errors are uncorrelated in time. The charge error is then

$$Err_{FC} = Error_{1pulse} * \sqrt{N_p} = 0.1 * \sqrt{N_p} nA * sec, \tag{3.57}$$

where N_p is the number of helicity pulses. The relative error is

$$Error_{FC} = \frac{Err_{FC}}{I * t} = \frac{0.1}{I\sqrt{N_p}}, \tag{3.58}$$

where t is the number of seconds.

Consider a case where the Faraday Cup errors are correlated in time. The Faraday Cup error due to digitization for the entire data run is still 1 count, which is negligible. The existence of two helicities creates the possibility that one helicity will be correlated with Faraday Cup counts that are above the average. The randomization of the helicity sequence discussed above eliminates any such correlation. The randomization ensures it with a statistical error of about $\sqrt{N_p}$. As a result one of the helicities can have $\sqrt{N_p}$ more pulses with above average Faraday Cup count. The total error is $\sqrt{N_p}*1count$ since the error is at most 1 count per pulse. This estimate gives exactly the same number as the estimation for uncorrelated case.

The experimental beam current was above $0.5nA$ on average. The average number of helicity pulses for each kinematic setting was at least 60,000 resulting in a systematic error of less than 1%:

$$Error_{FC} \sim \frac{0.1}{0.5\sqrt{60,000}} = 0.0008 \tag{3.59}$$

The kinematic setting with the beam energy $E = 2.6GeV$ and the CLAS magnetic field that corresponds to the CLAS Torus current $I_T = 1500nA$ had only 40,000 helicity pulses but the beam current was high enough, $I = 1.8nA$, so that $Error_{FC} = 0.0003 < 1\%$.

3.3.6 Uncertainties from the Kinematics

The errors in the calculation of the kinematic variables such as W and Q^2 contribute to the systematic errors of the experiment. The momentum corrections introduced in Section 3.2.4 change the electron momentum by less than 1%. This resulted in changes in W of about $20MeV$. The error in the beam energy dE is about $50MeV$ which is about 2% for the lowest beam energy $E_{beam} = 2.6GeV$. The DC tracking resolution is about $\frac{\delta p}{p} = 1\%$ (Section 2.2.1), while uncertainties in the reconstructed track angles ϕ, θ are about $2mrad$. We will show below that the systematic errors in Q^2 and W are less than 3%.

From Equation (1.7):

$$Q^2 = 4EE'sin^2\frac{\theta}{2}, \tag{3.60}$$

and

$$\frac{dQ^2}{Q^2} = \sqrt{\left(\frac{dQ^2}{d\theta}\frac{d\theta}{Q^2}\right)^2 + \left(\frac{dQ^2}{dE}\frac{dE}{Q^2}\right)^2 + \left(\frac{dQ^2}{dE'}\frac{dE'}{Q^2}\right)^2}; \tag{3.61}$$

where $\frac{dQ^2}{Q^2 dE}dE = \frac{dE}{E} < 2\%, \frac{dQ^2}{Q^2 dE'}dE = \frac{dE'}{E'} = 1\%$, $\frac{dQ^2}{Q^2 d\theta}d\theta = ctg\frac{\theta}{2}d\theta$. The minimal scattering angle is achieved for $2GeV$ out-bending data. It is $9°$, and therefore, $\frac{dQ^2}{Q^2 d\theta}d\theta < ctg\frac{9°}{2}0.002 = 2.5\%$. The average θ for that setting is $14°$, which corresponds to $ctg\frac{14°}{2}0.002 = 1.6\%$. The final result for $\frac{dQ^2}{Q^2}$ is :

$$\frac{dQ^2}{Q^2} < \sqrt{(0.025)^2 + (0.02)^2 + 0.01^2} = 0.03. \tag{3.62}$$

The invariant mass W is equal to

$$W^2 = M_p^2 - Q^2 + 2M_p(E - E'). \tag{3.63}$$

Thus:

$$\frac{dW}{W} = \frac{dW^2}{2W^2} = \sqrt{\left(\frac{dQ^2}{4W^2}\right)^2 + \left(\frac{2M_p dE}{4W^2}\right)^2 + \left(\frac{2M_p dE'}{4W^2}\right)^2}, \tag{3.64}$$

and

$$\frac{dQ^2}{4W^2} = \frac{dQ^2}{Q^2}\frac{Q^2}{4W^2} < 0.03\frac{2}{4} = 0.015. \tag{3.65}$$

Since the highest measured Q^2 is $\sim 2GeV^2$ and the smallest W is $\sim 1GeV$,

$$\frac{2M_p dE}{4W^2} = \frac{2 * 0.938 * 0.05}{4} = 0.023, \tag{3.66}$$

and

$$\frac{2M_p dE'}{4W^2} = \frac{dE'}{E}\frac{2M_p E'}{4W^2} = 0.01\frac{2 * 0.938 * 4}{4} = 0.019, \tag{3.67}$$

where the highest measured energy of the scattered electron $E' < 4GeV$. From

Eq. (3.64),

$$\frac{dW}{W} < \sqrt{0.015^2 + 0.023^2 + 0.019^2} = 0.03. \tag{3.68}$$

Physical observables in our experiment will be reported as functions of kinematical variables W and Q^2. We have just shown that uncertainties in the determination of these variables are about 3%.

3.3.7 Uncertainties from the Normalization Factor

We have used elastic scattering to calculate the overall normalization factor N_{norm} as described in Section 3.2.8. There are two types of errors that contribute to N_{norm}. One is the uncertainty Err_{GeGm} of the elastic formfactors and the other, Err_{Nstat}, is the statistical error involved in the calculation of the number of events under the elastic peak (Fig. 3-11).

The cross section difference (Eq. (1.37)) can be written as

$$\sigma^{\downarrow\uparrow} - \sigma^{\uparrow\uparrow} = \frac{\sigma^{\downarrow\uparrow} - \sigma^{\uparrow\uparrow}}{\sigma^{\downarrow\uparrow} + \sigma^{\uparrow\uparrow}}(\sigma^{\downarrow\uparrow} + \sigma^{\uparrow\uparrow}) = 2A\sigma_{unpol}, \tag{3.69}$$

where A is asymmetry and σ_{unpol} is the unpolarized cross section.

We used the parameterization of the elastic formfactors by Peter Bosted [70]. It was shown in that paper [70] that the error in the fit to the unpolarized cross section is 3%. The asymmetry, A, depends only on the ratio of formfactors $\frac{G_E}{G_M}$. The recent data from JLab [71] for the ratio can be used instead of the assumption $G_E^c = G_M/\mu$. Our experiment was not sensitive to this ratio. The difference between two parameterizations, (3.21) and (3.27), resulted in a variation less than 1% of the asymmetry A [27]. Therefore the error in the normalization factor N_{norm} due to uncertainty in the elastic formfactors is ;

$$Err_{GeGm} = 3\%, \tag{3.70}$$

Table 3.1: The errors of the normalization factor N_{norm}.

$Setting$	$Err_{Nstat}\%$	$Err_{GeGm}\%$	$Err_{N_{norm}}\%$
2.6 GeV B=1500	7	3	8
2.6 GeV B=2500	4	3	5
2.6 GeV B=-1500	3	3	4
4.3 GeV B=-2250	7	3	8

Table 3.2: The total systematic error of the g_1 structure function.

$Contributor$	$Error\%$
The CLAS Efficiency	5
Particle Identification (PID)	2
^{15}N polarization	1.5
Faraday Cup	0.08
Kinematics	3
Elastic normalization factor N_{norm}	8
F1A2	2
Total	13

$$Err_{N_{norm}} = \sqrt{Err^2_{GeGm} + Err^2_{Nstat}}. \tag{3.71}$$

The error Err_{Nstat} is usually within 7% as shown in Table 3.1.

The normalization factor was calculated using data for all values of Q^2 ; as a result the quoted error is the same for all Q^2 values as well.

3.3.8 The Total Systematic Error

Table 3.2 shows that systematic error is determined mainly by the uncertainty of the CLAS efficiency and the uncertainty of the normalization factor. The systematic errors related to the use of the models for the proton structure functions are discussed in later subsections. The error of the CLAS efficiency was determined as an average number for all the Q^2 values since individual values were the same within the precision of the calculation. The rest of the errors in Table 3.2 are the upper limits.

3.3.9 The Uncertainties of the Models

The experiment measured the cross section difference

$$\Delta\sigma = \sigma^{\uparrow\downarrow} - \sigma^{\uparrow\uparrow}. \tag{3.72}$$

This cross section difference can be expressed in terms of $g_1(x,Q^2)$,$A_2(x,Q^2)$ and $F_1(x,Q^2)$ using the equations of section 1.3.3:

$$\Delta\sigma = 4\sigma_{Mott}tan^2\frac{\theta}{2}\left(\frac{E+E'cos\theta}{M_p\omega}g_1(x,Q^2) - \frac{\sqrt{Q^2}}{M_p\omega}F_1(x,Q^2)A_2(x,Q^2)\right). \tag{3.73}$$

Extraction of the $g_1(x,Q^2)$ polarized structure function requires the knowledge of the product $A_2(x,Q^2)F_1(x,Q^2)$:

$$g_1(x,Q^2) = \frac{M_p\omega}{E+E'cos\theta}\frac{\Delta\sigma}{4\sigma_{Mott}tan^2\frac{\theta}{2}} + \frac{\sqrt{Q^2}}{E+E'cos\theta}F_1(x,Q^2)A_2(x,Q^2). \tag{3.74}$$

There are not many data for $A_2(x,Q^2)$, therefore a model has to be used. The model is described in section 3.2.11. The systematic error of the $g_1(x,Q^2)$ extraction can be estimated by taking $A_2(x,Q^2) = 0$. This estimation puts the entire correction factor of Eq. (3.74) to zero. The calculated systematic error for $\Gamma = \int g_1(x,Q^2)dx$ is less than 0.002 for the range of Q^2 and x used in our experiment.

$$Err_{F1A2} = 0.002. \tag{3.75}$$

3.3.10 The Systematic Error of the DIS contribution

The GDH integral requires the knowledge of the $g_1(W,Q^2)$ structure function for all values of W. We will use the model described in Section 3.2.11 for $g_1(W,Q^2)$ for the values of W above those measured by CLAS. To evaluate the systematic error of this model dependent contribution we will use a different model that has been developed by S. Simula et al. [72]. This model is a new phenomenological parameterization of the proton data. It includes both photo- and electro-production experimental data.

Table 3.3: The systematic error of the DIS contribution.

Q^2, GeV^2	Γ^p Simula	Γ^p Model	$\delta\Gamma^p$
0.19	0.008	0.004	0.004
0.24	0.011	0.0057	0.005
0.33	0.016	0.011	0.005
0.45	0.023	0.019	0.004
0.55	0.03	0.027	0.003
0.69	0.037	0.034	0.003

Table 3.3 shows contribution of the region $W > 2$ estimated by these two models. The systematic error can be estimated as ;

$$Error_{DIS} = \delta\Gamma^p_{W>2} = \Gamma^p_{Simula} - \Gamma^p_{Model}. \tag{3.76}$$

Chapter 4

Experimental Results

4.1 Results for Cross Sections

Results for the cross section difference $\frac{d\sigma^{\downarrow\uparrow}}{dWdQ^2} - \frac{d\sigma^{\uparrow\uparrow}}{dWdQ^2}$ are presented in Figures 4-1-4-6. The data clearly demonstrate the importance of the Delta resonance for small values of Q^2. The Delta is the dominant resonance for $Q^2 = 0.2GeV$, as can be seen in Fig. 4-1, whereas it becomes less and less important for higher values of Q^2. These results are discussed in Section 4.4.

4.2 Results for the $g_1(x, Q^2)$ Polarized Structure Function

A measurement of the generalized GDH Integral $I_{GDH}(Q^2) = \frac{16\pi^2\alpha}{Q^2}\int_0^{x_0} g_1(x, Q^2)dx$ requires knowledge of the $g_1(x, Q^2)$ polarized structure function. Inclusive electroproduction experiments, on the other hand, measure $g_1(x, Q^2)$ with some admixture of the $g_2(x, Q^2)$ polarized structure function as shown in Equation (1.37). Different generalizations of the GDH integral (section 1.7) can include combinations of $g_1(x, Q^2)$ and $g_2(x, Q^2)$ but those combinations are different from the one that is measured (Eq. 1.37). For example the definition I_{GDH_c} includes g_1 only, definition I_{GDH_b} includes combination $g_1 + \frac{4M^2x^2}{Q^2}g_2$, while the experimentally measured

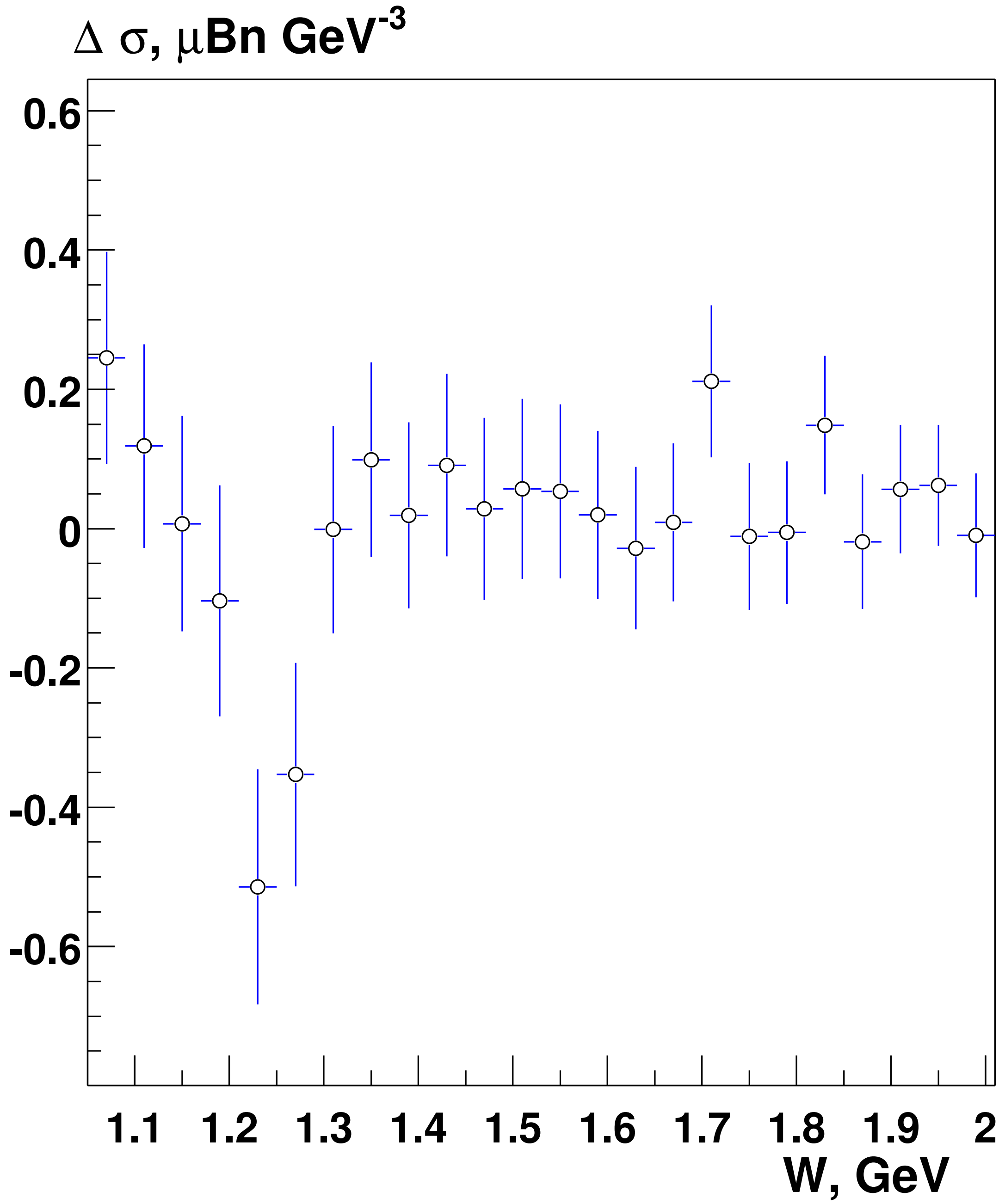

Figure 4-1: $\Delta\sigma = \frac{d\sigma^{\downarrow\uparrow}}{dWdQ^2} - \frac{d\sigma^{\uparrow\uparrow}}{dWdQ^2}$ is plotted as a function of the invariant mass W for $Q^2 = 0.19GeV^2$.

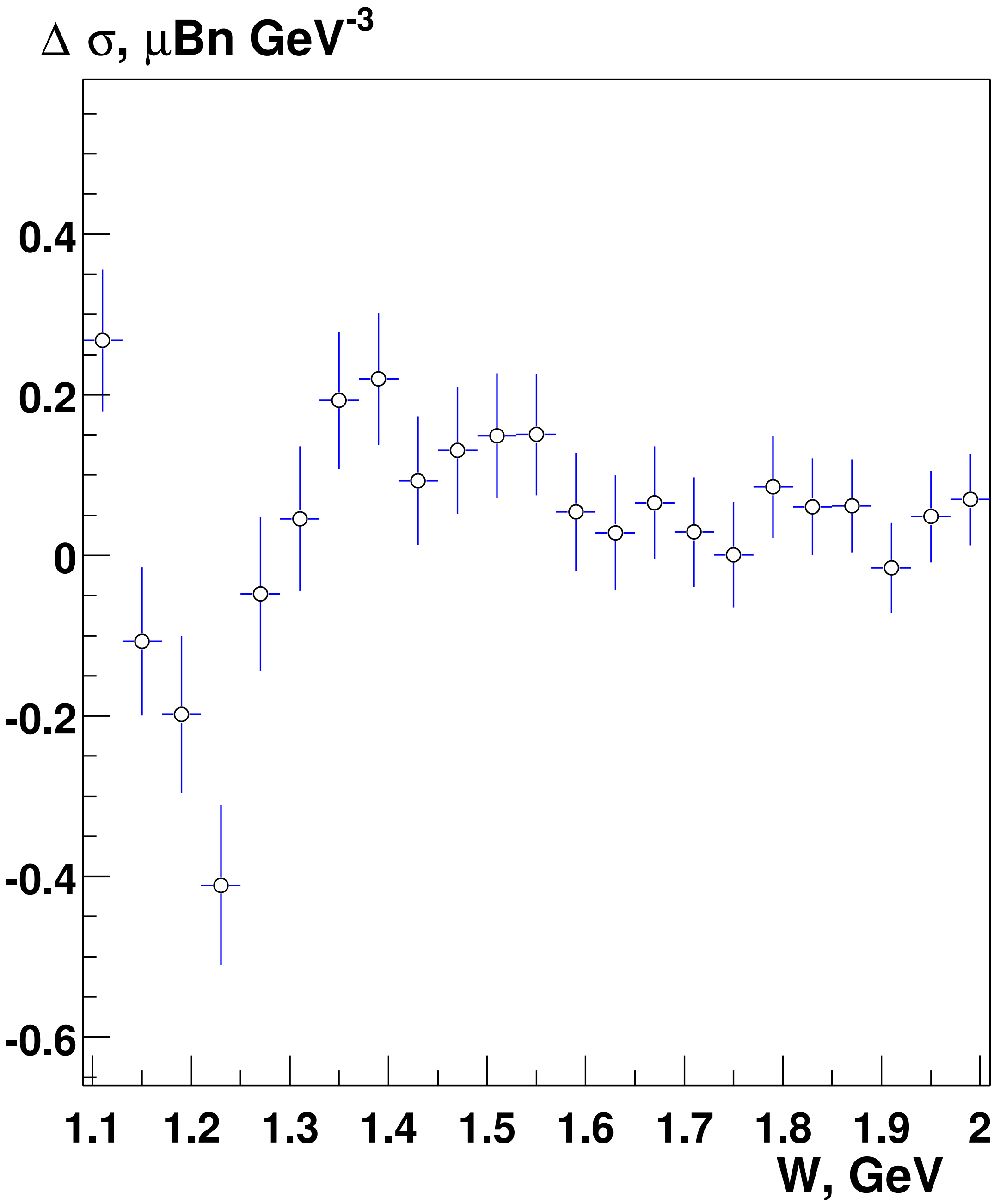

Figure 4-2: $\Delta\sigma = \frac{d\sigma^{\downarrow\uparrow}}{dWdQ^2} - \frac{d\sigma^{\uparrow\uparrow}}{dWdQ^2}$ is plotted as a function of the invariant mass W for $Q^2 = 0.24GeV^2$.

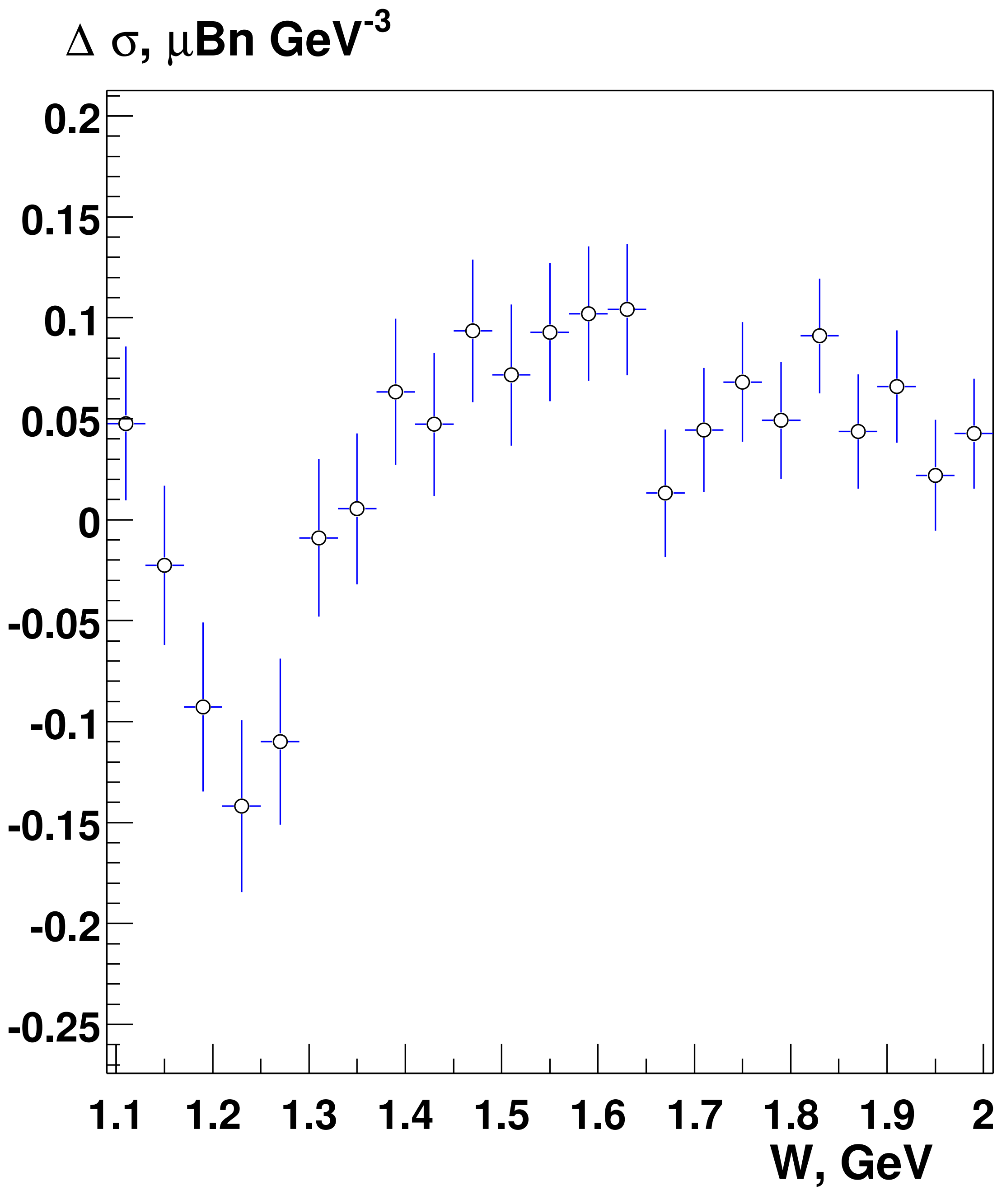

Figure 4-3: $\Delta\sigma = \frac{d\sigma^{\downarrow\uparrow}}{dWdQ^2} - \frac{d\sigma^{\uparrow\uparrow}}{dWdQ^2}$ is plotted as a function of the invariant mass W for $Q^2 = 0.33 GeV^2$.

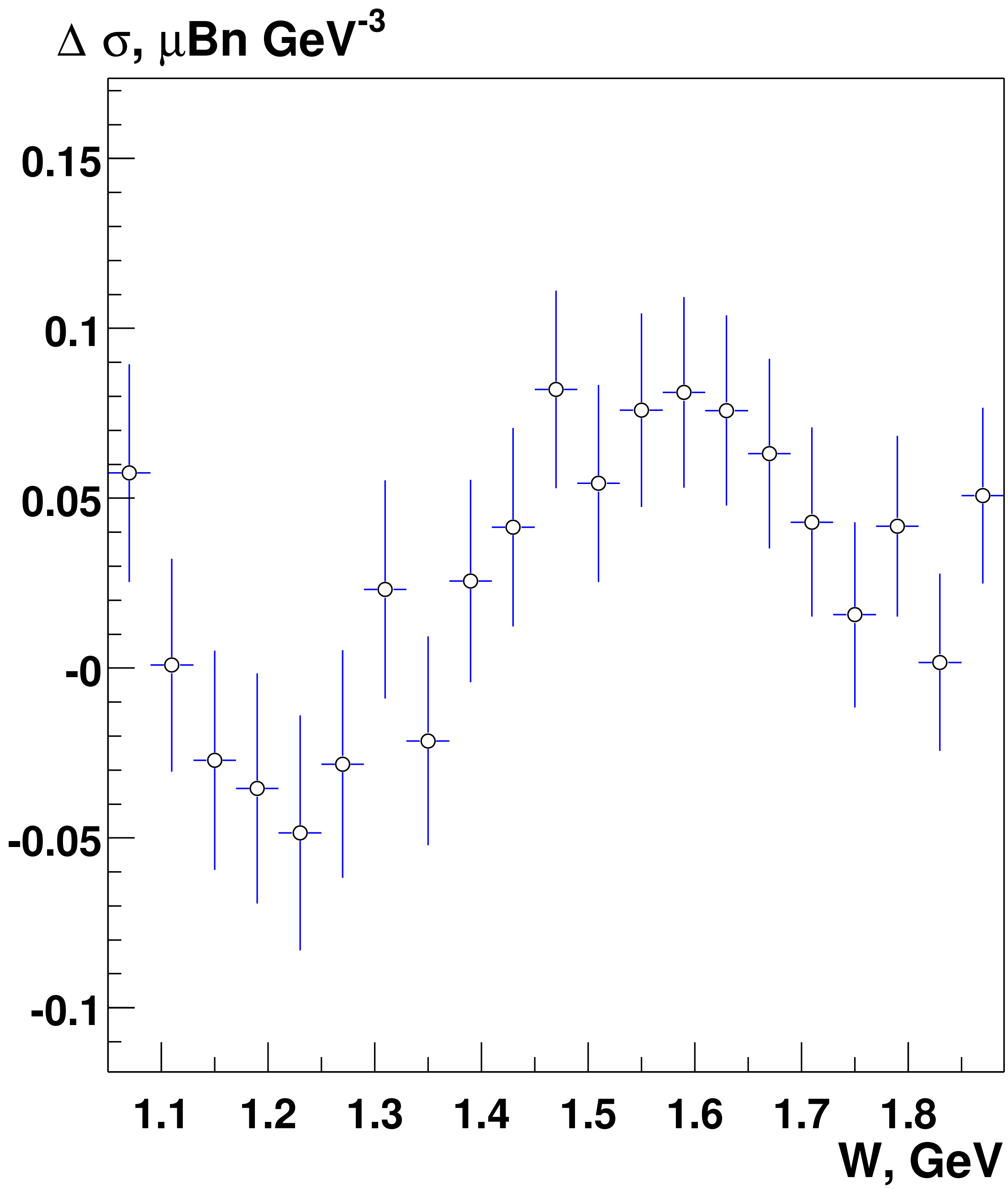

Figure 4-4: $\Delta\sigma = \frac{d\sigma^{\downarrow\uparrow}}{dWdQ^2} - \frac{d\sigma^{\uparrow\uparrow}}{dWdQ^2}$ is plotted as a function of the invariant mass W for $Q^2 = 0.45GeV^2$.

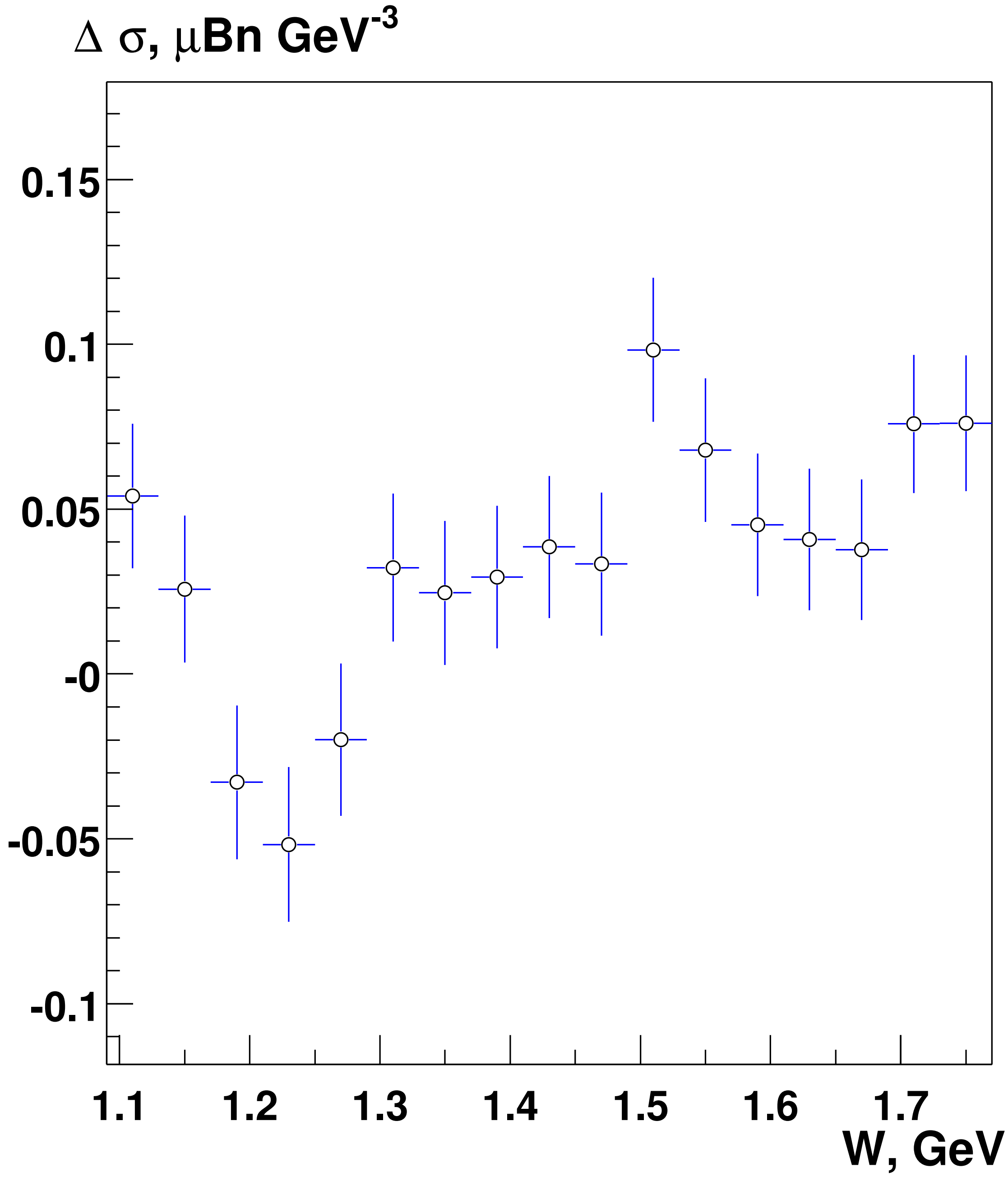

Figure 4-5: $\Delta\sigma = \frac{d\sigma^{\downarrow\uparrow}}{dWdQ^2} - \frac{d\sigma^{\uparrow\uparrow}}{dWdQ^2}$ is plotted as a function of the invariant mass W for $Q^2 = 0.55GeV^2$.

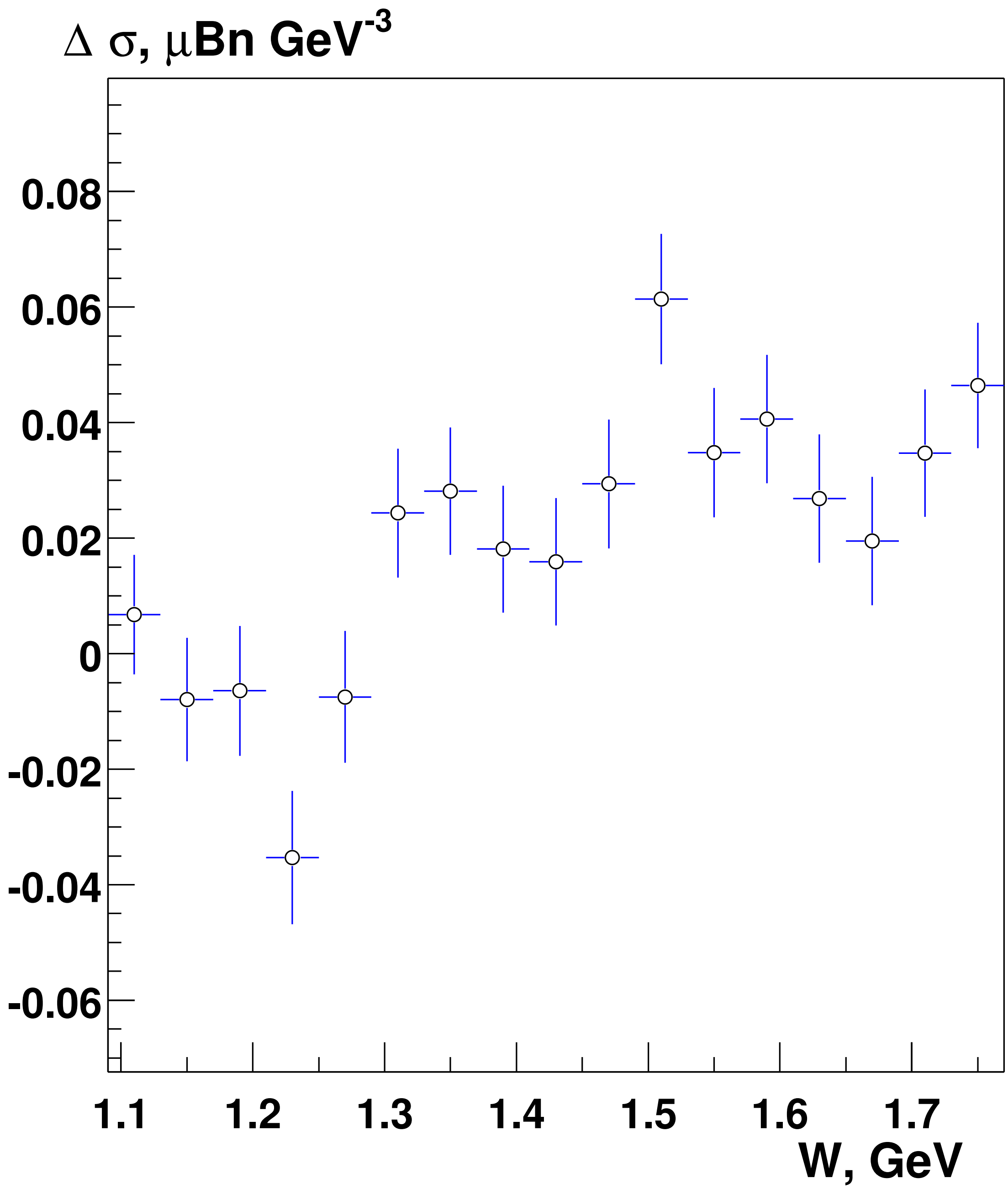

Figure 4-6: $\Delta\sigma = \frac{d\sigma^{\downarrow\uparrow}}{dWdQ^2} - \frac{d\sigma^{\uparrow\uparrow}}{dWdQ^2}$ is plotted as a function of the invariant mass W for $Q^2 = 0.69 GeV^2$.

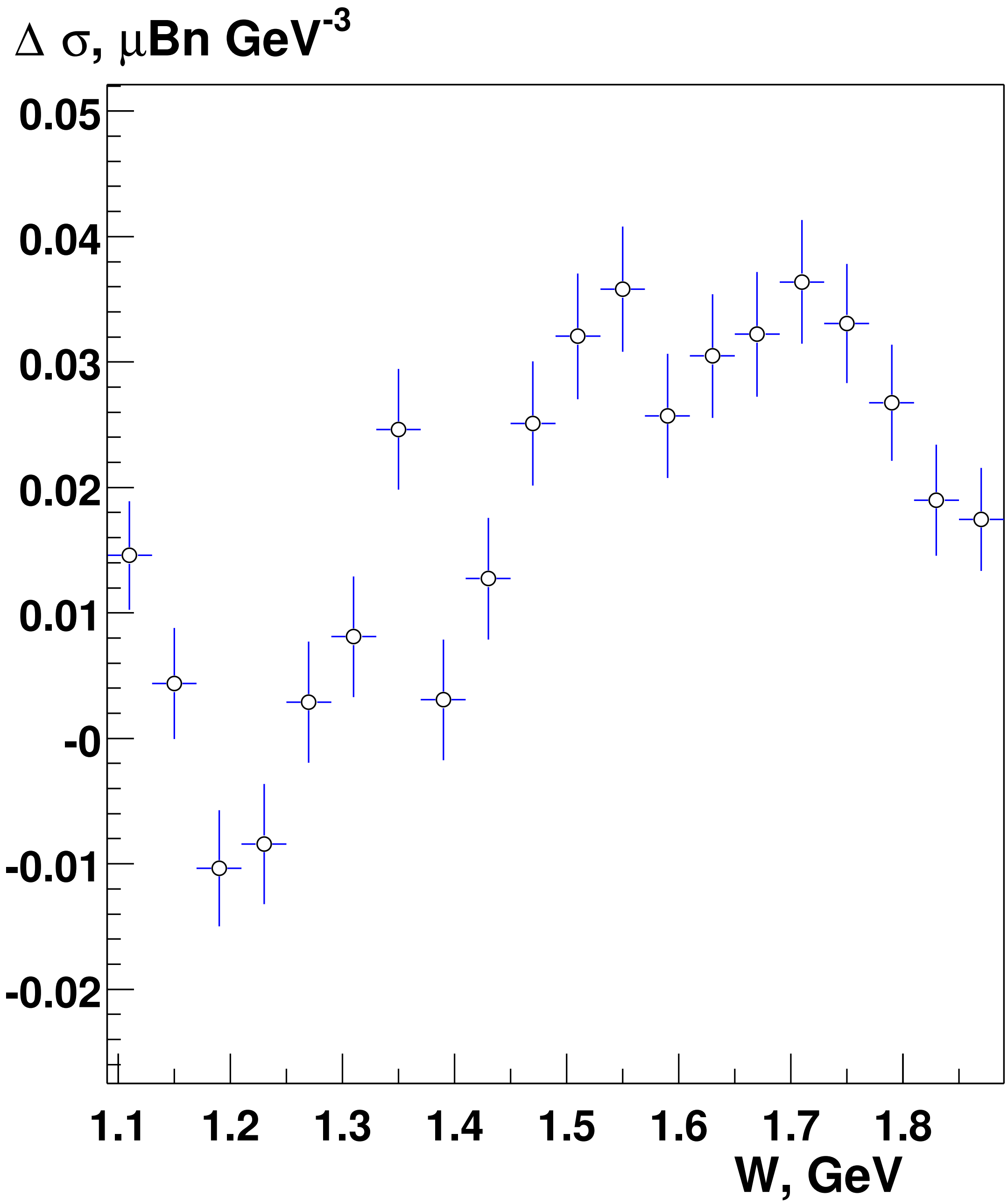

Figure 4-7: $\Delta\sigma = \frac{d\sigma^{\downarrow\uparrow}}{dW dQ^2} - \frac{d\sigma^{\uparrow\uparrow}}{dW dQ^2}$ is plotted as a function of the invariant mass W for $Q^2 = 0.89GeV^2$.

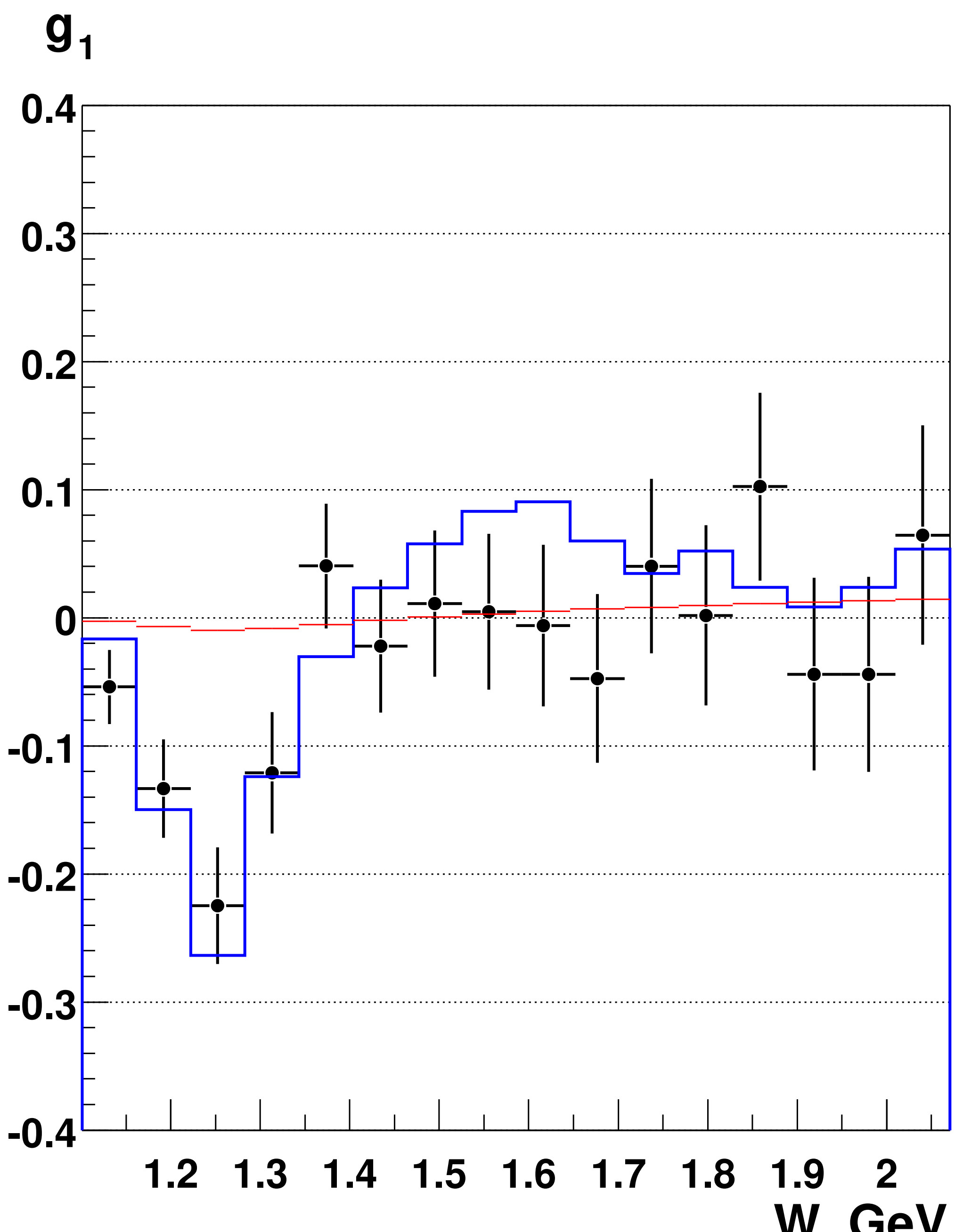

Figure 4-8: $g_1(W, Q^2)$ is plotted as a function of the invariant mass W for $Q^2 = 0.19 GeV^2$. The thick solid line represents the model described in Section 3.2.11. The thin solid line represents the systematic error due to g_2 subtraction.

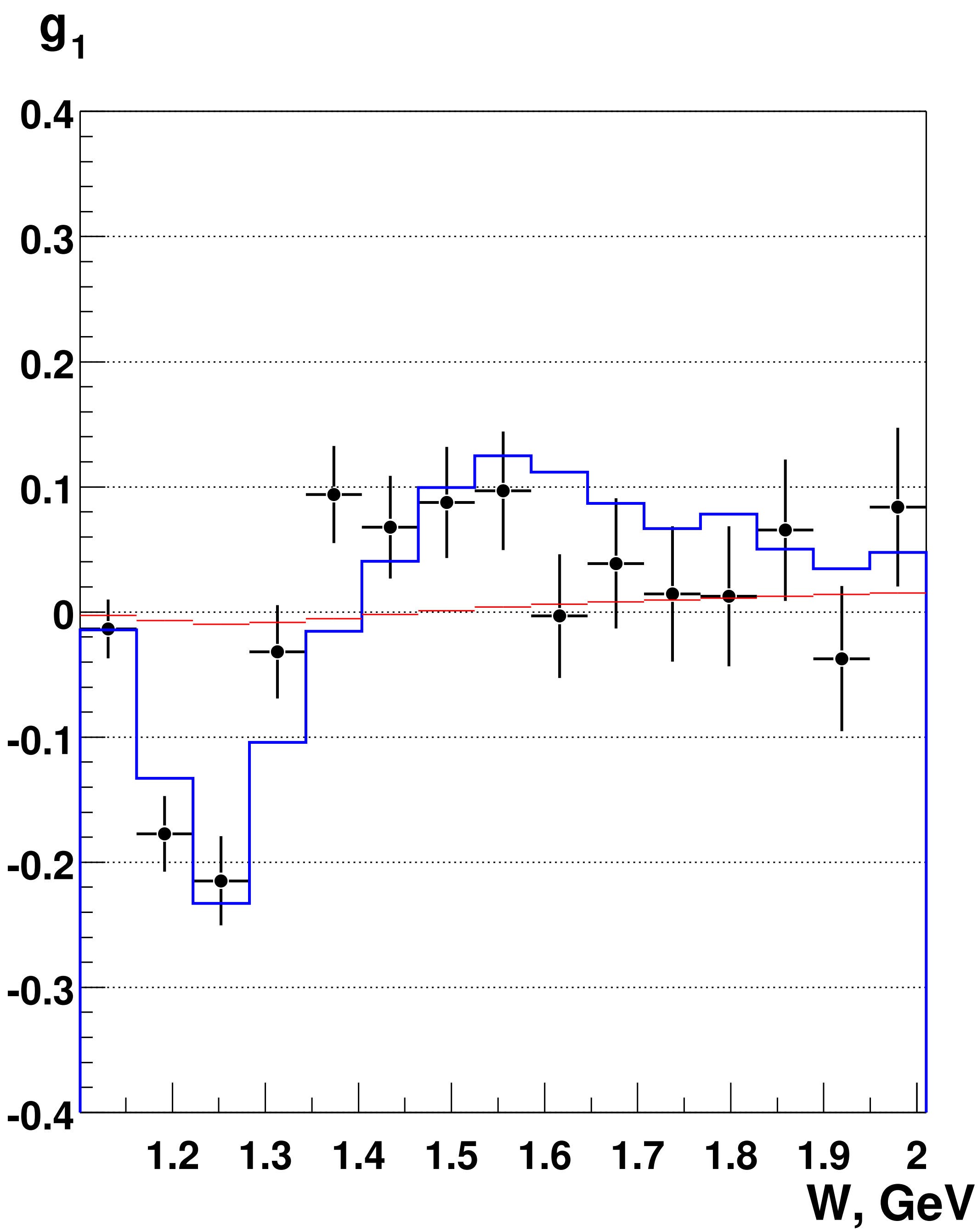

Figure 4-9: $g_1(W, Q^2)$ is plotted as a function of the invariant mass W for $Q^2 = 0.24 GeV^2$. The thick solid line represents the model described in Section 3.2.11. The thin solid line represents the systematic error due to g_2 subtraction.

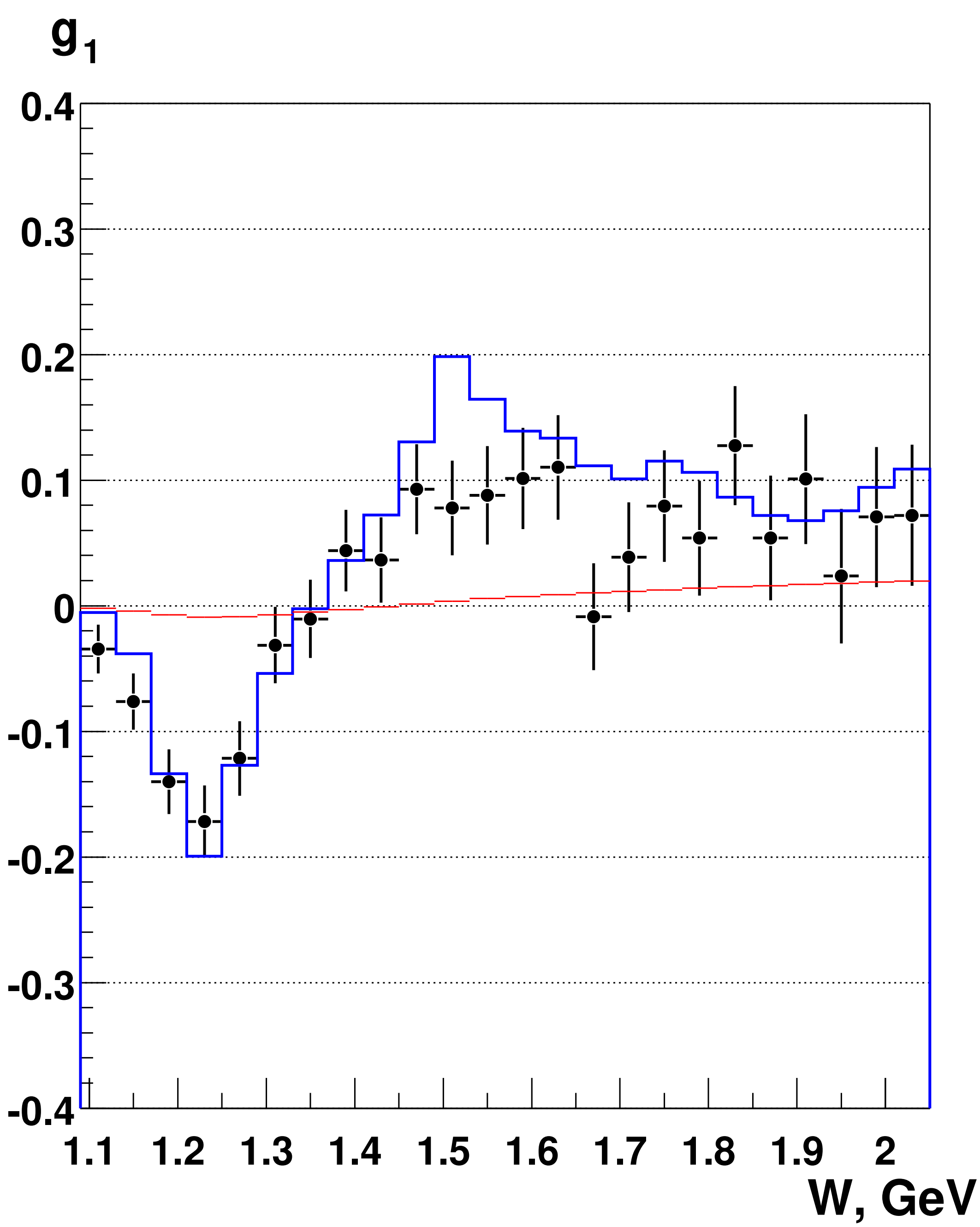

Figure 4-10: $g_1(W, Q^2)$ is plotted as a function of the invariant mass W for $Q^2 = 0.33GeV^2$. The thick solid line represents the model described in Section 3.2.11. The thin solid line represents the systematic error due to g_2 subtraction.

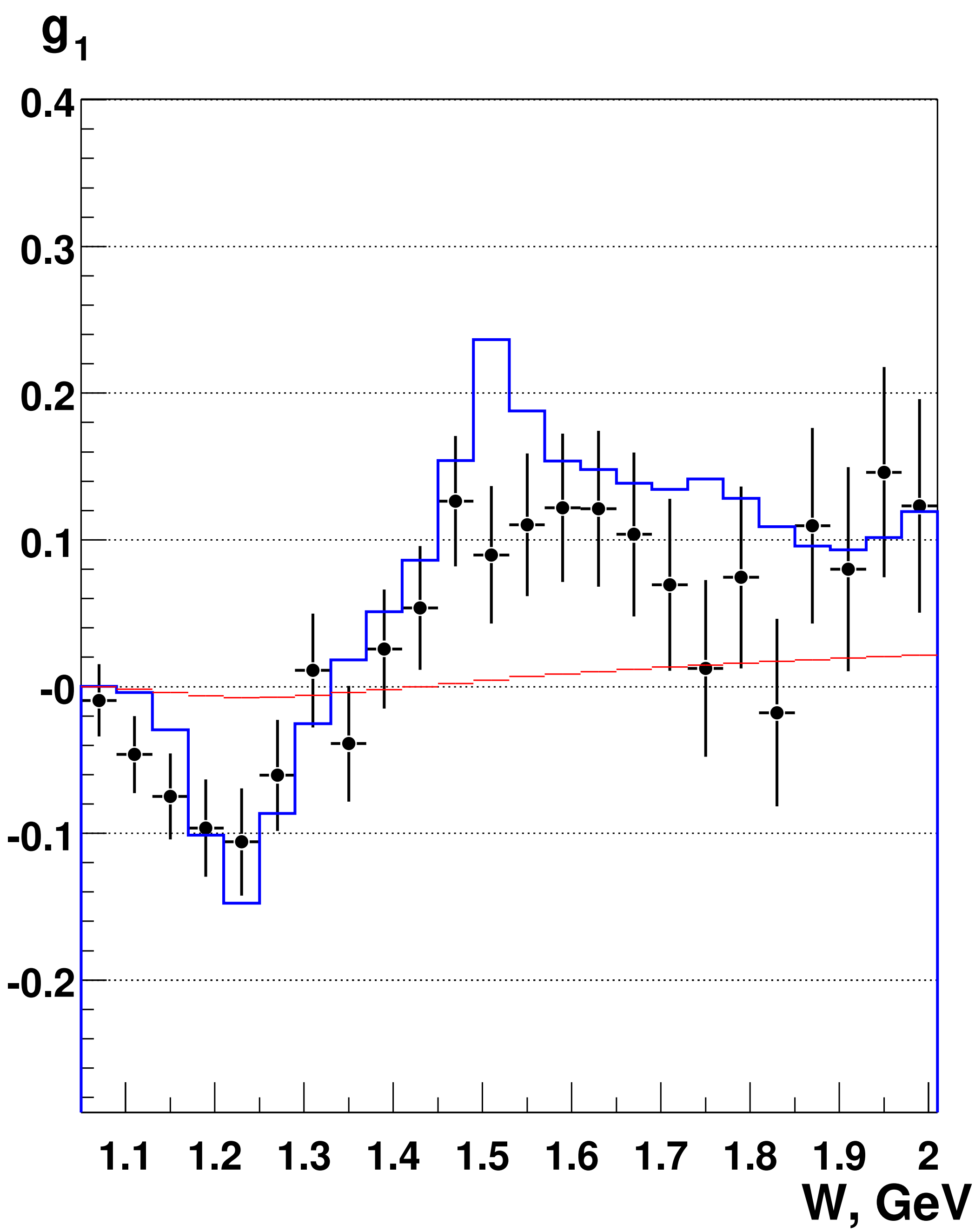

Figure 4-11: $g_1(W, Q^2)$ is plotted as a function of the invariant mass W for $Q^2 = 0.45 GeV^2$. The thick solid line represents the model described in Section 3.2.11. The thin solid line represents the systematic error due to g_2 subtraction.

Figure 4-12: $g_1(W, Q^2)$ is plotted as a function of the invariant mass W for $Q^2 = 0.55 GeV^2$. The thick solid line represents the model described in Section 3.2.11. The thin solid line represents the systematic error due to g_2 subtraction.

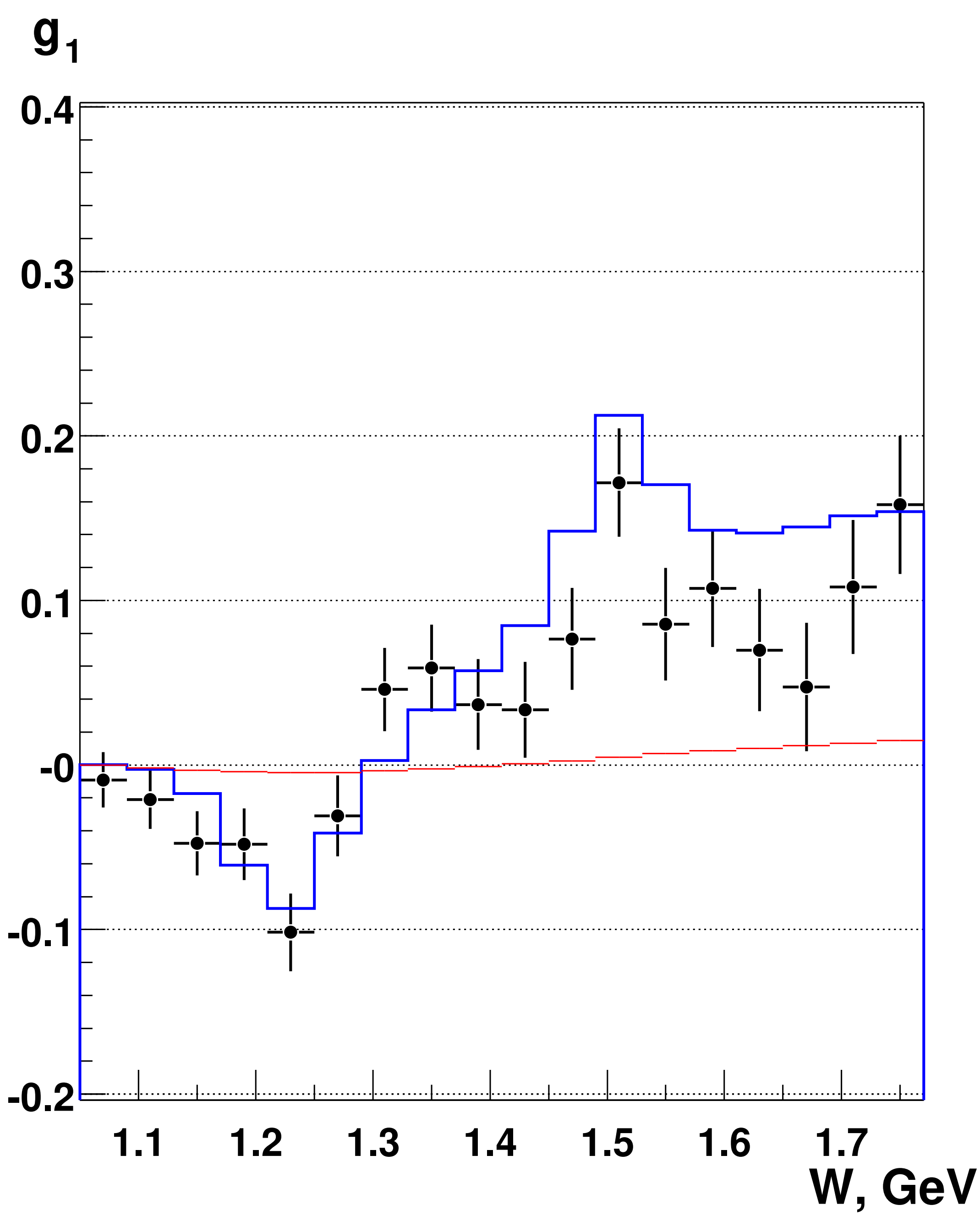

Figure 4-13: $g_1(W,Q^2)$ is plotted as a function of the invariant mass W for $Q^2 = 0.69 GeV^2$. The thick solid line represents the model described in Section 3.2.11. The thin solid line represents the systematic error due to g_2 subtraction.

Figure 4-14: $g_1(W, Q^2)$ is plotted as a function of the invariant mass W for $Q^2 = 0.89 GeV^2$. The thick solid line represents the model described in Section 3.2.11. The thin solid line represents the systematic error due to g_2 subtraction.

combination is $\frac{E+E' cos\Theta}{M\omega}g_1 + \frac{Q^2}{M\omega}g_2$.

To account for the $g_2(x, Q^2)$ structure function, a model is required. The model used in our experiment is a fit to the world data. It is described in Section 3.2.11.

The results for $g_1(x, Q^2)$ after subtraction of the modeled $g_2(x, Q^2)$ are shown in Figures 4-8-4-13. We can change the variable of integration from Bjorken x to invariant mass W:

$$I_{GDH}(Q^2) = \frac{16\pi^2\alpha}{Q^2}\int_0^{x_0} g_1(x, Q^2)dx = \frac{16\pi^2\alpha}{Q^2}\int_{W_0}^{\infty} g_1(x, Q^2)J_{xW}dW, \tag{4.1}$$

where J_{xW} is a Jacobian of transformation from x to W,

$$J_{xW} = |\frac{dx}{dW}| = \frac{2xW}{W^2 + Q^2 - M^2}. \tag{4.2}$$

The Jacobian J_{xW} significantly suppresses contribution of the data at high W. Figures 4-8-4-13 demonstrate that there is a good agreement between the model and the data.

4.3 Results for the First Moment of the Polarized Structure Function g_1 and the Generalized GDH Integral

The polarized structure function $g_1(x, Q^2)$ allows us to determine its first moment $\Gamma^p(Q^2)$:

$$\Gamma^p(Q^2) = \int_0^{x_0} g_1(x, Q^2)dx = \int_{W_0}^{\infty} g_1(x, Q^2)J_{xW}dW, \tag{4.3}$$

where x_0 and W_0 correspond to pion threshold. Since the last integral includes integration up to infinity, the complete $\Gamma^p(Q^2)$ has to include not only the resonance region measured by CLAS but also the region of Deep Inelastic Scattering(DIS).

The contribution of the resonance region to $\Gamma^p(Q^2)$ measured by CLAS is shown in Table 4.1 under the column Γ^p_{CLAS}. For W above the region measured in this

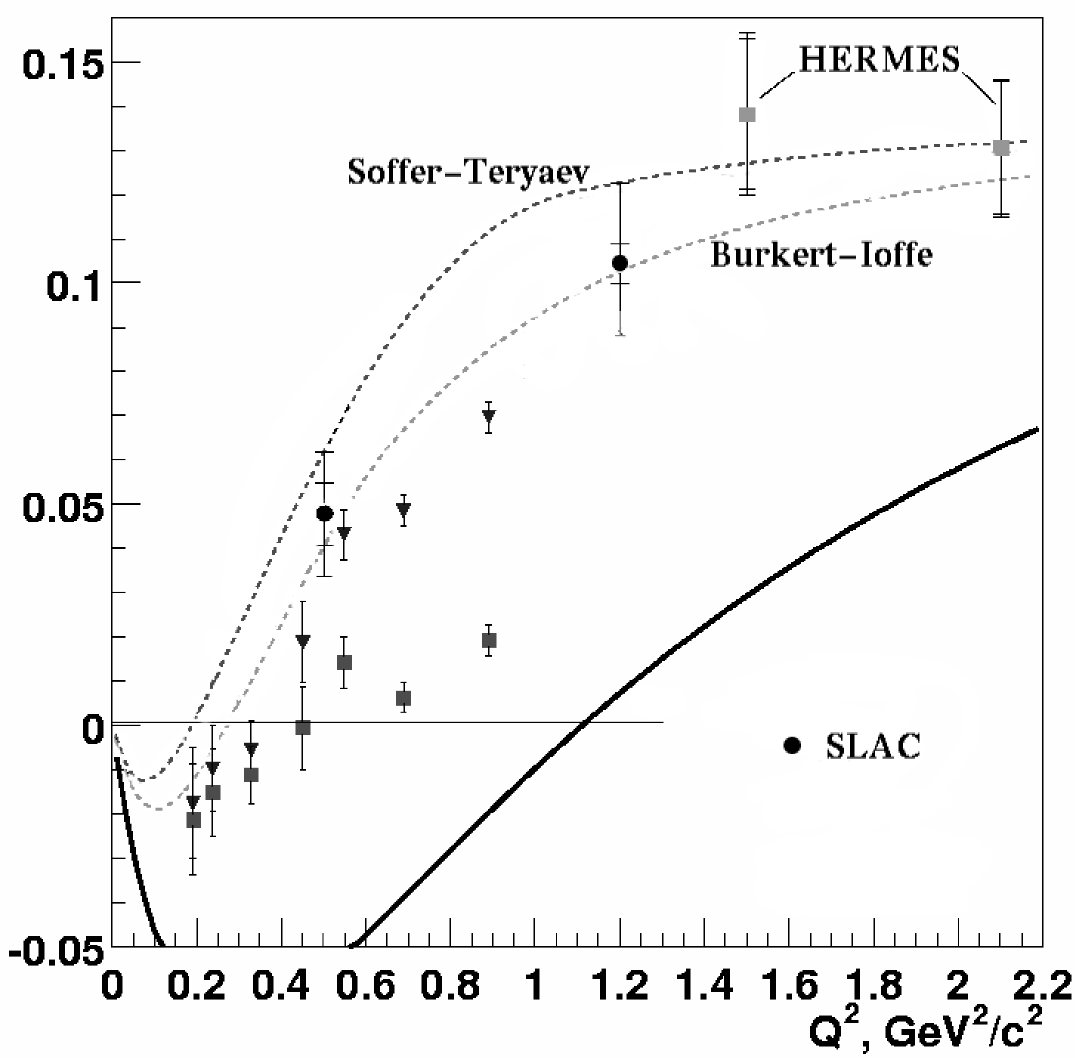

Figure 4-15: The first moment of g_1 is plotted as a function of Q^2. The squares show our data. The triangles represent our data plus the deep inelastic contribution given by the model. Only statistical errors are shown. The solid black line is the model of Anselmino, Ioffe and Leader [31], [32].

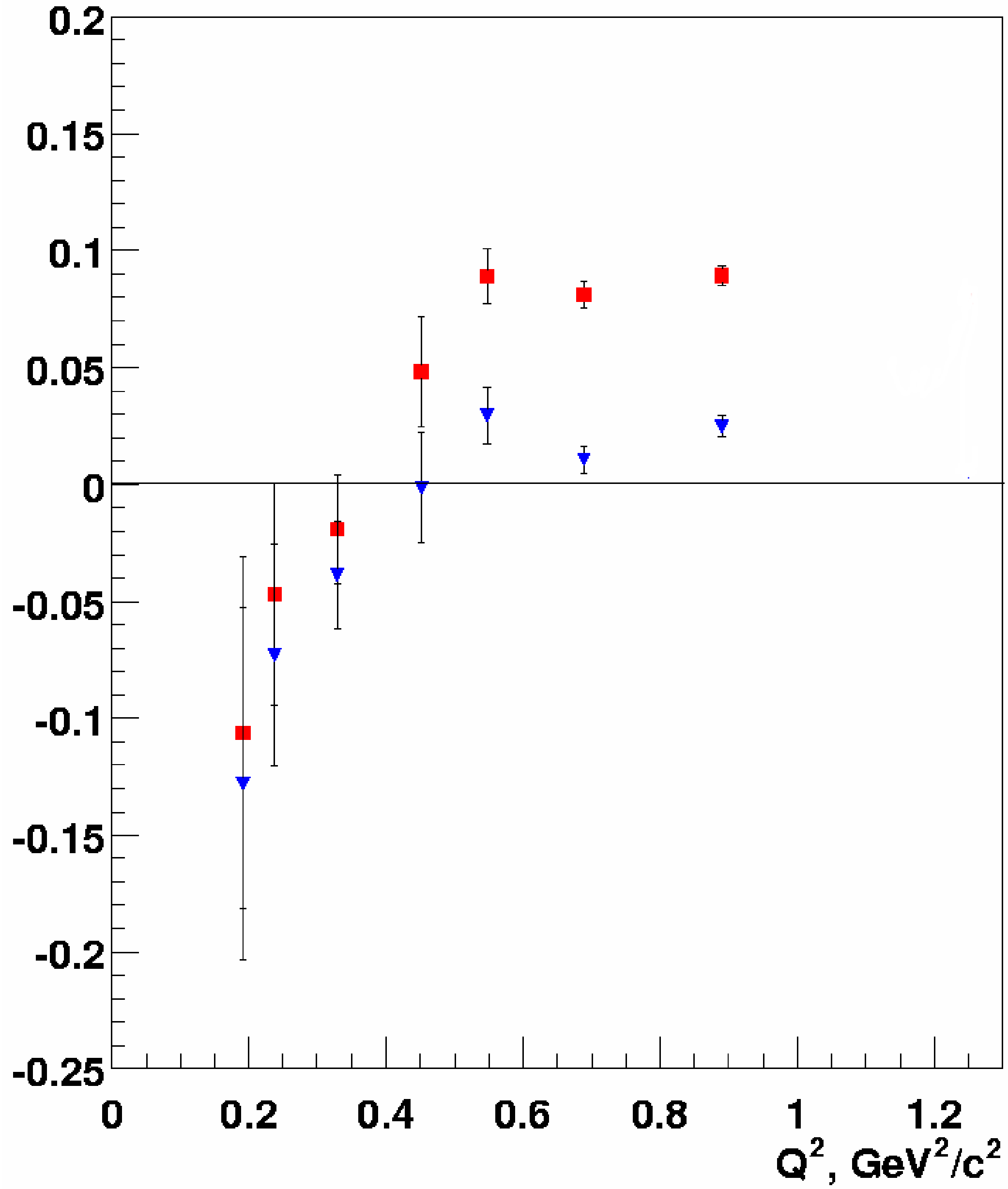

Figure 4-16: The GDH integral is plotted as a function of Q^2. The triangles show our data. The squares show our data plus the deep inelastic contribution given by the model. Only statistical errors are shown.

Table 4.1: The first moment of the proton $\Gamma^p(Q^2)$. W_{max} is the maximum value of W measured in our experiment. $\Gamma^p(Q^2) = \Gamma^p_{CLAS}(Q^2) + \Gamma^p_{DIS}(Q^2)$. $\Gamma^p_{CLAS}(Q^2)$ is measured in our experiment. $\Gamma^p_{DIS}(Q^2)$ is the model dependent contribution of Deep Inelastic Scattering.

Q^2, GeV^2	W_{max}, GeV	Γ^p_{CLAS}	Γ^p_{DIS}	Γ^p	Error stat	Error syst
0.19	2.0	-0.021	0.0035	-0.0175	0.012	0.004
0.24	2.0	-0.0152	0.0055	-0.0097	0.0098	0.005
0.33	2.0	-0.0111	0.0109	-0.0056	0.0065	0.005
0.45	1.9	-0.00059	0.019	0.0189	0.0092	0.005
0.55	1.8	0.0143	0.026	0.0431	0.0058	0.005
0.69	1.75	0.0063	0.043	0.049	0.0034	0.004
0.89	1.9	0.0192	0.0505	0.069	0.0034	0.004

experiment, the model for $g_1(W, Q^2)$ discussed in Section 3.2.11 is used. The model contribution corresponds to Γ^p_{DIS} in Table 4.1. The complete $\Gamma^p(Q^2)$ is shown in Figure 4-15.

The generalized GDH integral can be calculated from $\Gamma^p(Q^2)$:

$$I_{GDH}(Q^2) = \frac{16\pi^2\alpha}{Q^2}\Gamma^p(Q^2) = \frac{16\pi^2\alpha}{Q^2}\int_{W_0}^{\infty} g_1(x, Q^2) J_{xW} dW. \tag{4.4}$$

The data for the generalized GDH integral are shown in Figure 4-16 and Table 4.2. The generalized GDH integral crosses zero at the same Q^2 point as $\Gamma^p(Q^2)$. The zero crossing occurs at $Q^2 \approx 0.25 - 0.35 GeV^2$.

4.4 Discussion and Conclusions

The GDH integral spans an extremely large region of Q^2 and ω. In order to describe it, one has to bring together very different approaches from different physical domains. The high Q^2 region can be described with the use of QCD. The very low Q^2 region can be explored by chiral perturbation theory. At present, the low to intermediate energy region can only be explored through the use of classical phenomenological models such as the vector dominance model and the constituent quark model [48]. For the future, lattice QCD is a hopeful candidate for studies in the intermediate

Table 4.2: The GDH integral $I_{GDH}(Q^2)$. W_{max} is the maximum value of W measured in our experiment. $I_{GDH}(Q^2) = I_{GDHCLAS}(Q^2) + I_{GDHDIS}(Q^2)$. $I_{GDHCLAS}(Q^2)$ is measured in our experiment. $I_{GDHDIS}(Q^2)$ is the model dependent contribution of Deep Inelastic Scattering.

Q^2, GeV^2	W_{max}, GeV	$I_{GDHCLAS}$	I_{GDHDIS}	I_{GDH}	Error stat	Error syst
0.19	2.0	-0.1280	0.0210	-0.1053	0.0722	0.0240
0.24	2.0	-0.0729	0.0264	-0.0465	0.0470	0.0240
0.33	2.0	-0.0387	0.0380	-0.0195	0.0226	0.0174
0.45	1.9	-0.0015	0.0486	0.0483	0.0235	0.0128
0.55	1.8	0.0294	0.0544	0.0888	0.0120	0.0104
0.69	1.75	0.0105	0.0717	0.0811	0.0056	0.0066
0.89	1.9	0.0248	0.0653	0.0893	0.0044	0.0051

region. Most of the theoretical work has been along the lines described above.

As was pointed out by X. Ji [52], it might be possible for chiral perturbation theory to allow us to understand the Q^2-dependence of the GDH integral from $Q^2 = 0$ to the neighborhood of $0.2 GeV^2$. In contrast, it is believed that the operator product expansion (OPE) could be extended from $Q^2 = \infty$ down to the neighborhood of $0.5 GeV^2$. For the window in between these limits, where this experiment has precise data, we do not yet have a firm theoretical understanding of $I_{GDH}(Q^2)$. This is a region where the transition from hadron to parton degrees of freedom occurs. Therefore, we hope that our data will be a testing ground for various theoretical ideas. Below we expand a bit on these ideas.

For large Q^2, Γ can be expressed as a power series in $1/Q^2$ following an operator product expansion [52], [81]:

$$\Gamma(Q^2) = \sum_{\tau=2,4,\ldots} \frac{\mu_\tau(Q^2)}{(Q^2)^{(\tau-2)/2}}. \tag{4.5}$$

Only μ_2 [61] and μ_4 [81] have been calculated so far and no one has yet worked out μ_6. This expansion is expected to converge for $Q^2 > 0.5 GeV^2$ [52]. The physical scale parameter which controls the expansion is the average parton transverse momentum in the nucleon, $k_\perp \approx 0.5GeV$[83]. Dimensional analysis shows that

$$\mu_\tau \sim k_\perp^{\tau-2}. \tag{4.6}$$

Therefore, it is hoped that the $1/Q^2$ expansion can be a good approximation if one restricts one's attention to $Q^2 > 0.5GeV^2$.

It is important to calculate higher-order corrections in the OPE expansion if one is to approach the limit $Q^2 = 0.5GeV^2$. As it stands, the models are far from achieving this. Lattice QCD calculations may help to establish the connection between chiral perturbation theory and operator product expansion calculations; however, there are no lattice QCD calculations available in the region of our experiment at the present time.

The low Q^2 region is naturally the best place to employ chiral perturbation theory (χPT). In χPT, one regards the pion mass, m_π, and the external three-momentum, p, as small compared to any other scale in the problem [82]. Bernard, Kaiser and Meissner [35] have done calculations in this region. They predicted the Q^2 dependence of the GDH integral, $I_{GDH_a}(Q^2)$ (Eq. (1.57)), in the region of small Q^2, where Q^2 is considered to be small if it does not exceed the square of a few pion masses. These calculations were done in the extreme non-relativistic limit and also with a fully relativistic formulation. The value of the derivative, $I'_{GDH_a}(Q^2) = \frac{dI_{GDH_a}(Q^2=0)}{dQ^2}$, was calculated to be approximately in the band from $2.2GeV^{-4}$ to $5.7GeV^{-4}$. According to the approach of Bernard, Kaiser and Meissner the integral $I_{GDH_a}(Q^2)$ crosses zero at $Q^2 = 0.23GeV^2$.

X. Ji and J. Osborn [52] used the relationship between the generalized GDH integral and the amplitude for virtual-photon Compton scattering:

$$\int G_1(\omega, Q^2)\frac{d\omega}{\omega} = \frac{1}{4}S_1(\omega = 0, Q^2), \tag{4.7}$$

where $G_1(\omega, Q^2)$ (Eq. 1.13,1.32) is the spin-dependent structure function and where $S_1(0, Q^2)$ [52] is the forward Compton amplitude with the elastic contribution subtracted. They have calculated the right-hand side of the equation using χPT. X. Ji and J. Osborn made calculations in the leading-order of chiral perturbation theory for the Q^2 dependence of the GDH integral [52] using heavy-baryon chiral perturbation theory ($HB\chi PT$), in which one formally takes the nucleon mass to infinity. Ji and Osborn found out that the leading chiral contribution is the same as in the work of Bernard, Kaiser, and Meissner [35].

Calculations in next-to-leading order ($O(p^4)$) in χPT [82] predict the slope of the GDH integral to be negative. The leading order calculations ($O(p^3)$) by Bernard, Kaiser, and Meissner [35] predicted the slope to be about the same value but of opposite sign.

There is a substantial difference between the results of [82] and [35]. The hope is that the agreement might be better once two-loop and Δ resonance effects are included. The comparison of the ($O(p^3)$) results [35] and ($O(p^4)$) results [82] shows that higher order corrections are large, so that even orders higher than ($O(p^4)$) must be computed. Our experimental data start at a Q^2, which is relatively high for χPT and the present status of the calculations is too incomplete to consider a comparison at $Q^2 \sim 0.2GeV^2/c^2$.

Corrections to the leading order of χPT become very important at high Q^2. These corrections limit the applicability of χPT to the generalized GDH integrals to region of very small Q^2. V. Burkert [51] showed that while this is true for calculation of I_n of the neutron and for I_p of the proton the calculation of their difference, $I_p - I_n$, may be valid to considerably higher Q^2. It is very difficult to deal with resonances in the χPT framework. Taking the difference $I_p - I_n$ eliminates the isospin 3/2 resonances such as the $\Delta(1232)$ and reduces the contribution of others [51].

One of the important questions involves the convergence of the GDH Integral. Mueller and Trueman [84] showed that, under the general assumptions of Regge theory, a “worst-case” high-energy behavior of $\sigma_{1/2} - \sigma_{3/2}$ is $\frac{const}{ln^2\omega}$, which makes the integral finite.

The GDH integral was parameterized by Soffer and Teryaev [28], [29], [30]. The integral was parameterized to reproduce the GDH and Burkhardt-Cottingham [46] values at $Q^2 = 0$ and the EMC [54] data at high Q^2. Soffer and Teryaev considered the GDH integral $I_1(Q^2) = \frac{2M^2}{Q^2}\int_0^1 g_1(x)dx$, as a difference of the integral $I_{1+2}(Q^2) = I_1(Q^2) + I_2(Q^2)$ and the integral $I_2(Q^2)$, where

$$I_2(Q^2) = \frac{2M^2}{Q^2}\int_0^1 g_2(x)dx. \tag{4.8}$$

A straightforward calculation [45] shows that;

$$I_{1+2}(Q^2 = 0) = \frac{\mu_a}{4}, \tag{4.9}$$

and

$$I_2(Q^2 = 0) = \frac{\mu_a^2 + \mu_a}{4}. \tag{4.10}$$

This is consistent with our familiar GDH value, $I_1(Q^2 = 0) = -\frac{\mu_a^2}{4}$. The Burkhardt-Cottingham sum rule [46] states that

$$I_2(Q^2) = \frac{1}{4}\mu G_M(Q^2)[\mu G_M(Q^2) - G_E(Q^2)], \tag{4.11}$$

where $G_M(Q^2)$ and $G_E(Q^2)$ are the nucleon Sachs formfactors normalized so that $G_M(0) = G_E(0) = 1$. For large values of Q^2, $I_{1+2}(Q^2) = I_1(Q^2)$. Comparison of $I_{1+2}(0)$ with the Q^2 behavior observed by the EMC collaboration at large Q^2 [54] shows that $I_{1+2}(Q^2)$, unlike $I_1(Q^2)$ and $I_2(Q^2)$, does not have a strong Q^2 behavior and can be smoothly interpolated between $Q^2 = 0$ and large Q^2. Figure 4-17 shows $I_{1+2}(Q^2)$, -$I_2(Q^2)$ and $I_1(Q^2) = I_{1+2}(Q^2) - I_2(Q^2)$, where $I_{1+2}(Q^2)$ is obtained by interpolation and $I_2(Q^2)$ is calculated from Eq. (4.11). The prediction that $I_1(Q^2) = 0$ at $Q^2 = 0.2GeV^2$ does not depend strongly on the interpolation.

Several models inspired by the vector-dominance model have been proposed over the years. The model by Anselmino, Ioffe and Leader [31], [32] parameterized the GDH integral $I_{GDH}(Q^2)$ by fitting to the GDH value at $Q^2 = 0$ and the EMC data at high Q^2 [54]. The following form of the Q^2 parameterization was chosen:

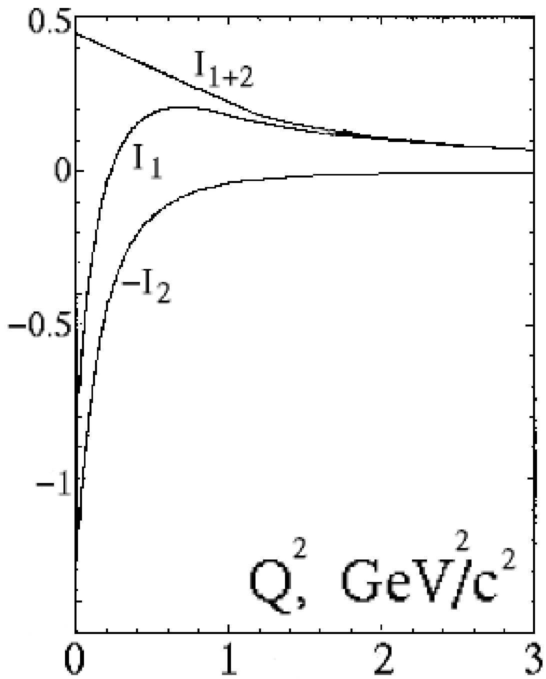

Figure 4-17: The various contributions to the GDH sum rule vs $Q^2, GeV^2/c^2$. The top, the middle, and the bottom lines represent $I_{1+2}(Q^2)$, $I_1(Q^2)$, and $-I_2(Q^2)$, respectively, as explained in the text [28].

$$I(Q^2) = 2M_p^2\Gamma_p^{as}\left(\frac{1}{Q^2+\mu^2} - \frac{c\mu^2}{(Q^2+\mu^2)^2}\right), \tag{4.12}$$

where

$$I(Q^2) = \frac{2M_p^2}{Q^2}\Gamma_p(Q^2), \tag{4.13}$$

$$\Gamma_p^{as} = \lim_{Q^2\to\infty}\Gamma_p(Q^2), \tag{4.14}$$

and

$$c = 1 + \frac{1}{8}\frac{\mu^2}{M_p^2}\frac{2}{\Gamma_p^{as}}. \tag{4.15}$$

The mass parameter μ characterizes the scale of the Q^2 variation. The model predicts zero crossing of the GDH integral at $Q^2 = 1.0 GeV^2$ for $\mu = m_\rho$. This model is contradicted by our experimental data (Fig. 4-15).

The model by Burkert and Ioffe [33], [34] added an estimation of the resonance contribution Γ_p^{res} to the calculation [31], [32]. Resonances up to $W = 1.8 GeV$ were included. The zero crossing of the GDH integral was predicted to occur at $Q^2 = 0.23 GeV^2$, which agrees with our data very well (Fig. 4-15), and we may conclude that inclusion of resonances (in particular the $\Delta(1232)$) plays an important role.

A Unitary Isobar Model has been developed for pion photo- and electro-production on the proton [85]. This Unitary Isobar Model is available from Mainz as the MAID2000 program. It contains Born terms, vector mesons and nucleon resonances ($P_{33}(1232)$, $P_{11}(1440)$, $D_{13}(1520)$, $S_{11}(1535)$, $F_{15}(1680)$, and $D_{33}(1700)$). The resonance contributions are included taking into account unitarity and providing the correct phases of the pion photo-production multipoles. This model is supposed to describe pion photo- and electro-production on nucleons at photon energies up to $1 GeV$.

MAID2000 takes into account only the single pion production channel. Resonance decays into multi-meson final states are not taken into account. Only Δ resonance is dominated by single pion decay ($> 99\%$). Resonances with higher mass ($1400 MeV < M < 1700 MeV$) have only $50 - 70\%$ chance to have a single pion decay, while resonances with $M \geq 1700 MeV$ ($D_{13}(1700)$, $D_{33}(1700)$, $P_{13}(1720)$, $P_{31}(1910)$, $P_{33}(1920)$, $F_{35}(1905)$) have probability of about 20%.

Our data are in good agreement with MAID2000 at small values of Q^2 where the $\Delta(1232)$ resonance dominates (Fig. 4-18). As one can see from Fig. 4-18, MAID2000 does not reproduce our (and SLAC) data for $Q^2 > 0.6 GeV^2/c^2$. Higher mass resonances and resonance decay into channels that involve more than single pion production become more important at such Q^2. The AO model discussed below works much better in this region, due to the fact that it takes into account resonance decays into all channels and not only into the single pion channel. The AO model also includes resonances at higher masses than MAID2000.

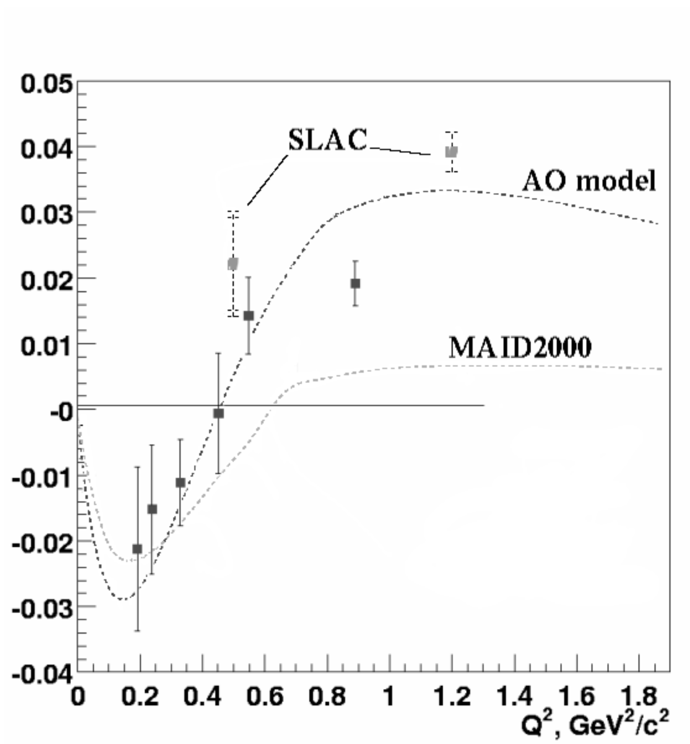

Figure 4-18: Our results for $\Gamma^p(Q^2)$ compared to MAID2000 and the AO models $(W \leq 2GeV)$.

In the MAID200 model, the non-resonant contribution was described by an effective Lagrangian. A major problem in applying MAID2000 to the case of virtual photons is associated with a lack of knowledge of the Q^2 dependence of the amplitudes. This might be another reason why MAID2000 fails to reproduce the data for high values of Q^2. The parameterizations of these dependences used in MAID2000 have to be checked by future experiments, since there is only a small amount of experimental information available at present.

Experimental data on helicity amplitudes are incorporated in the AO model [53]. The transition to the $P_{33}(1232)$ was described by the magnetic transition form factor G_M^Δ. The following empirical parameterization was used:

$$G_M^\Delta(Q^2) = G_M^\Delta(0) G_D^\Delta(Q^2) e^{-0.2Q^2}, \tag{4.16}$$

$$G_E^\Delta(Q^2) = 0, \tag{4.17}$$

where G_D^Δ is the usual dipole form factor. This parameterization is similar to the one used in the MAID2000. The available data for higher mass states ($P_{11}(1440)$, $S_{11}(1535)$, $D_{13}(1520)$, $F_{15}(1680)$) were also parametrized and incorporated into the model. Additional assumptions (such as $SU(6)$ algebraic symmetry between the transitions) were made for the experimentally undetermined transition amplitudes to the $S_{11}(1650)$, $S_{31}(1620)$, $D_{13}(1700)$, $D_{33}(1700)$, $D_{15}(1675)$, $P_{13}(1720)$, $P_{31}(1910)$, $P_{33}(1920)$, $F_{35}(1905)$, $F_{37}(1950)$. It was assumed that only a single quark is affected in the transitions. With currently available data, the assumption of the single quark transition and the algebraic relations cannot be tested accurately. The AO model is not able to estimate the contribution of the states with masses greater than $2GeV$ because no electro-production data exist for these states. The non-resonant contributions were neglected except for the single pion Born term at low energies. The AO model takes into account resonance decays into all known states while MAID2000 includes single pion channel only. The AO model is in a good agreement with our data. It suggests that the assumption about the single quark transition is well justified and that the multiple quark transition amplitudes can be neglected in this region. At higher values of Q^2 the agreement with the AO model is considerably better than with MAID2000. It suggests that channels apart from single pion production are probably important.

4.5 Summary

We made measurements of the inclusive cross sections in the Q^2 region where the transition from hadron to parton degrees of freedom occurs. Our experiment is in reasonable agreement with previous SLAC [9] and HERMES [56] data. This region is not well understood theoretically, as it is immensely complicated from the theoretical point of view and no satisfactory description exists at the present moment. It is hoped that our new results will provide a testing ground for new theoretical ideas. In particular, our experiment already clearly shows the importance of the resonance contributions in the intermediate Q^2 range.

The investigation of the GDH integral as a function of Q^2 in the resonance region and finding its zero crossing have been accomplished in these measurements. The contribution of the resonance region to the GDH integral I_{GDH} is seem to be particularly important for small values of Q^2. The Delta resonance is the dominant contributor to I_{GDH} for $Q^2 = 0.2GeV$, as can be seen in Fig. 4-8-4-13, whereas it becomes less and less important for higher values of Q^2, and its diminishing role is responsible for the negative to positive sign change of I_{GDH}. The GDH integral crosses zero at $Q^2 \approx 0.3GeV^2$. The rapid drop of the integral at small Q^2 is consistent with the large negative value of the GDH sum rule for real photons, although an extension of this study to values of Q^2 even smaller than $0.2GeV^2$ will be needed to make a meaningful extrapolation to the $Q^2 = 0$ case from the electro-production data.

At the present moment, neither chiral perturbation theory nor the operator product expansion theory is appropriate for describing the Q^2 region of an experiment. The model of J. Soffer and O. Teryaev [28], [29], [30] consistently overestimates $\Gamma^p(Q^2)$ and I_{GDH} in the resonance region. We can conclude that simple smooth interpolation of $\Gamma_{1+2}(Q^2) = \Gamma_1(Q^2) + \Gamma_2(Q^2)$ from $Q^2 = 0$ to the high Q^2 used in the model may not be adequate. The Soffer and Teryaev result is very sensitive to the validity of the Burkhardt-Cottingham sum rule [46]. Violation of this rule can also contribute to the discrepancy between the model and the data. The model of V. D. Burkert and B. L. Ioffe [33], [34] is in better agreement with our experiment, although it slightly overestimates the data. The AO model is in good agreement with our data and a comparison with the MAID2000 shows the importance of channels other than single pion production.

Although the behavior of the integral has been well captured by this experiment, there are still some details that might be interesting to investigate further. Data with better precision are needed to make a separation of the g_1 and g_2 structure functions. The separation will eliminate the g_2 model dependence that is present in our results. The investigation of the GDH integral for the neutron usually requires subtraction of the proton contribution. This is the case for any experiment with a deuteron target. The improved precision of the proton data will be a big help for such experiments. The other area that will benefit from the better precision experiments is the measurement of the higher moments of the proton structure functions. These higher moments are related to the proton polarizability and would be an interesting subject to investigate.

Appendix A

The GDH Sum Rule for Real Photons

The Gerasimov sum rule connects static properties of the nucleon with the integral that runs over all energies:

$$\int_{\omega_0}^{\infty} \frac{(\sigma_{\frac{1}{2}}(\omega') - \sigma_{\frac{3}{2}}(\omega'))d\omega'}{\omega'} = -\frac{2\pi^2\alpha\mu_a^2}{M^2}, \tag{A.1}$$

where μ_a, M are the anomalous magnetic moment and the mass of the nucleon. ω_0 is the energy threshold for pion-production. $\sigma_{\frac{1}{2}}(\omega)$ and $\sigma_{\frac{3}{2}}(\omega)$ are the photo-absorption cross sections for the total helicity of the photon-nucleon system in the center of mass system being $\frac{3}{2}$ and $\frac{1}{2}$ respectively. The integral runs over photon energies starting from pion threshold up to infinity.

For the sake of understanding the limitations of and possible ways of breaking the GDH sum rule, we will examine its derivation in the next sections.

A.0.1 Outline of the Conventional Derivation of the GDH Sum Rule

We will use the following outline for the proof of the GDH sum rule.

1) The total photo-absorption cross section in the GDH integral can be found

by calculating the amplitude of the forward Compton scattering since the Optical Theorem connects the two. We will discuss the general form of this amplitude.

2) Subsequently we will examine a dispersion relationship as a way to connect the GDH type integral over all energies to the low energy limit of electron-nucleon scattering.

3) The following subsection will examine the low energy limit of the electron-nucleon interaction.

4) The last subsection will connect all of the above in the proof of the GDH sum rule.

A.0.2 Compton Scattering

Consider the amplitude T of the forward Compton scattering (Fig. A-1). The cross section for Compton scattering in the lab frame is

$$\frac{d\sigma(\omega)}{d\Omega} = T(\omega)T^*(\omega), \tag{A.2}$$

where the amplitude $T(\omega)$ is a complex but scalar quantity.

From general principles we have to form a scalar quantity $T(\omega)$ having only 3 non-scalar physical quantities ϵ, ϵ' and s, where the first two are 3-dimensional polarization vectors of incident and scattered photons respectively and $\vec{s}$ is a 3-dimensional hadron spin. We are interested in elastic scattering with $\epsilon' = \epsilon$. The only combinations of these vectors that have the needed properties and conserve parity are $(\epsilon^*\epsilon')$ and $(s[\epsilon^*\epsilon])$ where () and [] denote scalar and vector products of 3-vectors. Therefore the amplitude $T(\omega)$ generally is a sum of two terms with two unknown scalar functions $f_1(\omega)$ and $f_2(\omega)$ multiplying the corresponding vector combinations. The functions $f_1(\omega)$ and $f_2(\omega)$ are independent of polarization vectors ϵ, ϵ' and spin s.

$$T(\omega) = f_1(\omega)(\epsilon^*\epsilon) + 2i\omega f_2(\omega)(s[\epsilon^*\epsilon]), \tag{A.3}$$

where we took the factor $2i\omega$ out of $f_2(\omega)$ for convenience. Since both spin s and the

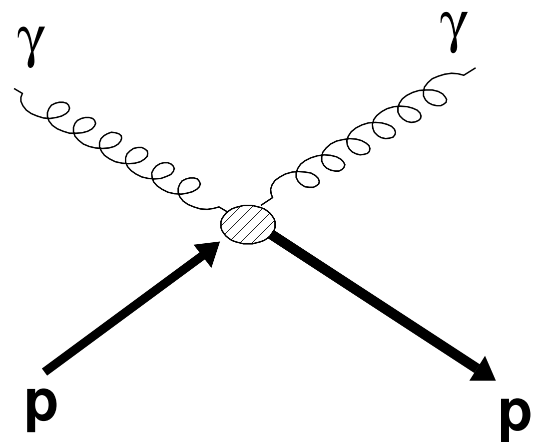

Figure A-1: Compton scattering from a nucleon.

vector product are pseudo vectors, the combination $(s[\epsilon^*\epsilon])$ conserves parity.

Let us consider the laboratory frame of reference with the third axis e_3 pointing in the direction of the incoming and outgoing photon (these two are the same since it is a forward scattering). The other two axes are perpendicular to e_3 and each other with no additional restrictions. Now consider scattering of circular polarized photons of positive helicity (left-circular) traveling along the e_3 axis. The polarization vector ϵ of these photons has the following components in the frame discussed:

$$\epsilon = \frac{1}{\sqrt{2}}(1, -i, 0), \tag{A.4}$$

and the complex conjugate

$$\epsilon^* = \frac{1}{\sqrt{2}}(1, +i, 0). \tag{A.5}$$

The product $(\epsilon^*\epsilon)$ can be directly computed to be

$$(\epsilon^*\epsilon) = 1, \tag{A.6}$$

while the vector product $[\epsilon^*\epsilon]$ is

$$[\epsilon^*\epsilon] = (0, 0, i). \tag{A.7}$$

Thus the amplitude of forward Compton scattering of left-circular photons is

$$\begin{aligned} T(\omega) &= f_1(\omega)(\epsilon^*\epsilon) + 2i\omega f_2(\omega)(s[\epsilon^*\epsilon]) \\ &= f_1(\omega) + 2\omega f_2(\omega)(s_1, s_2, s_3)(0, 0, -1)^T \\ &= f_1(\omega) - 2\omega f_2(\omega) s_3. \end{aligned} \tag{A.8}$$

The projection s_3 of the nucleon spin on the third axis can be ether $\frac{1}{2}$ or $-\frac{1}{2}$. Introducing subscripts $\frac{1}{2}$ and $\frac{3}{2}$, to distinguish the two possible situations of different total helicity of the photon-hadron system in the center of mass frame,

$$T_{\frac{1}{2}}(\omega) = f_1(\omega) + \omega f_2(\omega), \tag{A.9}$$

and

$$T_{\frac{3}{2}}(\omega) = f_1(\omega) - \omega f_2(\omega). \tag{A.10}$$

The Optical Theorem relates the total photo-absorption cross section $\sigma(\omega)$ to the imaginary part of the amplitude for forward Compton scattering $T(\omega)$,

$$\frac{\omega}{4\pi}\sigma = ImT(\omega). \tag{A.11}$$

Applying the Optical Theorem to the case of scattering of left-circular polarized photons with nucleons, we obtain for the two cases of nucleon polarization:

$$\frac{\omega}{4\pi}\sigma_{\frac{1}{2}} = ImT_{\frac{1}{2}}(\omega) = Imf_1(\omega) + \omega Imf_2(\omega), \tag{A.12}$$

and

$$\frac{\omega}{4\pi}\sigma_{\frac{3}{2}} = ImT_{\frac{3}{2}}(\omega) = Imf_1(\omega) - \omega Imf_2(\omega). \tag{A.13}$$

Adding and subtracting we fined,

$$Imf_i(\omega) = \frac{\omega^{2-i}}{8\pi}(\sigma_{\frac{1}{2}} + (-1)^{i-1}\sigma_{\frac{3}{2}}), \tag{A.14}$$

where i is 1 or 2.

A.0.3 Dispersion Relationship

We will use standard convention $c = 1, \frac{h}{2\pi} = 1$. The GDH integral is a dispersion integral of the familiar Kramers-Kronig type [13], [14]. As we will illustrate below, it is a direct consequence of the analyticity of the scattering amplitude which in turn is a consequence of causality.

It is well known that the requirement to preserve causality results in restrictions on the form of the scattering amplitude as a function of complex frequency [13], [14]. Namely, the scattering amplitude $f(\omega)$ can be analytically [17] continued into the upper half of the complex frequency plane. The two axes of the plane are the real and the imaginary part of ω.

To illustrate the connection between causality and analytical properties of the scattering amplitude we will consider a classical case of light propagating in a medium along the x axis [13],[14]. We will follow the derivation presented in Bjorken and Drell [15]. The forward-scattering amplitude is

$$a_{scatt}(\omega) = f(\omega)a_{inc}(\omega), \tag{A.15}$$

where incident light of any given frequency behaves like $a_{inc}(\omega)e^{-i\omega(t-x)}$ and the whole incident wave packet has the form

$$A_{inc}(x,t) = \int_{-\infty}^{\infty} d\omega a_{inc}(\omega')e^{-i\omega(t-x)}. \tag{A.16}$$

If the incident wave was absent in the scattering point x=0 before t=0 then causality demands that the incident signal vanishes for $x > t$ for any $x > 0$. Therefore,

$$a_{inc}(\omega) = \frac{1}{2\pi}\int_{-\infty}^{\infty} dx A_{inc}(x,0)e^{-i\omega x} = \frac{1}{2\pi}\int_{-\infty}^{0} dx A_{inc}(x,0)e^{-i\omega x}. \tag{A.17}$$

As a result of integration only up to zero, we can analytically continue $a_{inc}(\omega)$ into the upper half of the complex frequency plane by constructing the absolutely convergent integral:

$$a_{inc}(\omega + i\nu) \equiv \frac{1}{2\pi}\int_{-\infty}^{0} dx A_{inc}(x,0)e^{-i\omega x-\nu|x|}, \tag{A.18}$$

where $\nu > 0$ is a complex part of the frequency. The integral over dx exists since it differs from the previous one only by the damping factor $e^{-\nu|x|}$.

Similar arguments for the scattered wave demand that $a_{inc}(\omega)f(\omega) = a_{scatt}(\omega)$ is analytic in the upper half of the complex plane. $f(\omega) = \frac{a_{inc}(\omega)f(\omega)}{a_{inc}(\omega)}$ also has to be analytic in the upper half plane since both $a_{inc}(\omega)$ and $a_{inc}(\omega)f(\omega)$ are analytic in the upper half plane. Zeros in $a_{inc}(\omega)$ cannot produce poles in $f(\omega)$ because $f(\omega)$ is independent of $a_{inc}(\omega)$, which is an arbitrary incident wave (this arbitrariness allows us to put $a_{inc}(\omega)$ zeros anywhere). We have illustrated the connection between analytical properties of scattering amplitude $f(\omega)$ and causality.

The same arguments can be applied to our case of forward Compton scattering basically without any changes. The amplitudes $f_i(\omega)$ for forward Compton scattering described earlier are again analytic in the upper half of the complex ω plane. We will continue the amplitudes into the lower half by using the Schwarz reflection principle

[16]:

$$f_i(\omega^*) \equiv f_i(\omega)^* \tag{A.19}$$

where ω is purely imaginary. Approaching the real axis $\omega + i\epsilon$ where ω is real and $\epsilon > 0$, we see that $f_i(\omega + \epsilon) = f_i(\omega)$, $f_i(\omega + \epsilon)^* = f_i(\omega)^*$ since $f_i(\omega)$ is analytic in the upper half of the complex frequency plane including the real axis.

In the lower part of the complex plane by construction

$$f_i(\omega - \epsilon) = f_i(\omega + \epsilon)^* = f_i(\omega)^*. \tag{A.20}$$

Therefore,

$$f_i(\omega + \epsilon) - f_i(\omega - \epsilon) = f_i(\omega) - f_i(\omega)^* = 2iImf(\omega), \tag{A.21}$$

where ω is real. There is a discontinuity $2iImf(\omega)$ in the imaginary part of $f_i(\omega)$ while the real part is continuous.

$f_i(\omega)$ can pick up an imaginary part only with inelastic processes. If we work only within the precision of the first order of the fine structure constant α, no electromagnetic processes can actually contribute (processes like $e+$ $e-$ pair creation). $f_i(\omega)$ will gain an imaginary part only with the onset of inelastic processes for photoproduction reactions in the sector of strong interactions (or with the onset of the virtual multi-particle intermediate states using Compton scattering language) [16]. Single pion production is the first channel available with a threshold $\omega_0 = m_\pi + \frac{m_\pi^2}{2M_p}$. We established that the first cut in the complex plane is from ω_0 to ∞ along the real axis. $f_i(\omega)$ for negative ω can pick up an imaginary part from the u channel which has the same lowest state of interest, namely πN with threshold $-\omega_0$. This will result in the second cut from $-\infty$ to $-\omega_0$ along the real axis.

Cauchy's theorem [17] may be used for any finite contour of integration C, as long as it does not cross any cut:

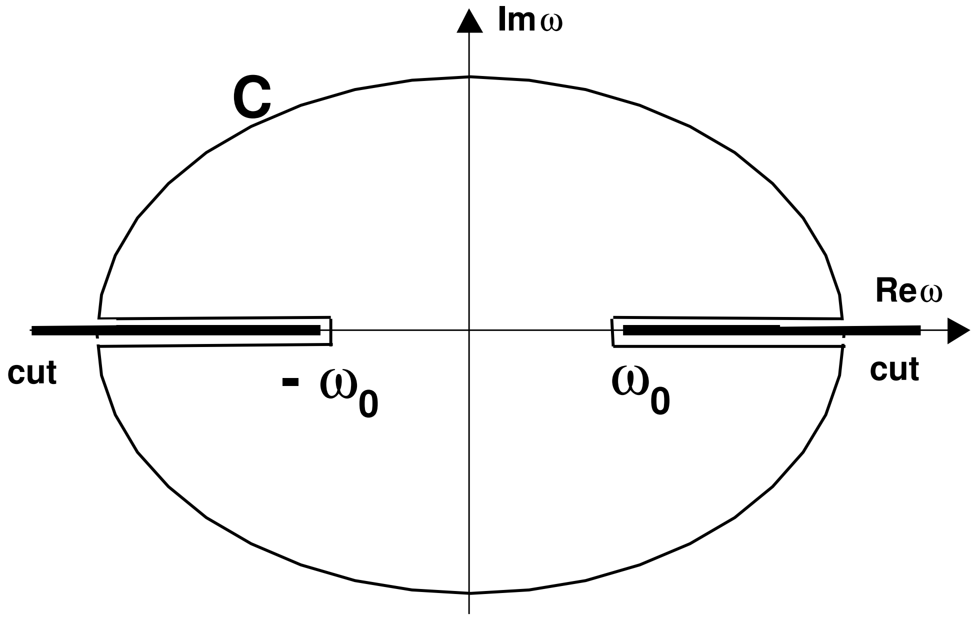

Figure A-2: Analytical properties of forward scattering Compton amplitudes f_i.

$$f_i(\omega) = \frac{1}{2\pi i} \int_C \frac{f_i(\omega')d\omega'}{\omega' - \omega}, \tag{A.22}$$

where ω is any point inside the integration contour C.

Let us take the integration contour shown in Fig. A-2 to infinity. A contribution, I_R, from the straight lines along the right cut is

$$I_R = \frac{1}{2\pi i} \int_{\omega_0}^{\infty} \frac{(f_i(\omega') - f_i^*(\omega'))d\omega'}{\omega' - \omega} = \frac{1}{\pi} \int_{\omega_0}^{\infty} \frac{Imf_i(\omega')d\omega'}{\omega' - \omega}, \tag{A.23}$$

where the two parts correspond to the integration above and below the cut.

A contribution I_L from the left cut is

$$I_L = \frac{1}{\pi} \int_{\omega_0}^{\infty} \frac{Imf_i(\omega')d\omega'}{\omega' + \omega}. \tag{A.24}$$

We denote the rest of the contour C as C_∞ since all C_∞ points go to infinity as we take contour C to infinity.

$$f_i(\omega) = \frac{1}{2\pi i}\int_C \frac{f_i(\omega')d\omega'}{\omega' - \omega} = I_R + I_L + I_\infty, \tag{A.25}$$

where

$$I_\infty = \frac{1}{2\pi i}\int_{C_\infty} \frac{f_i(\omega')d\omega'}{\omega' - \omega}. \tag{A.26}$$

Substituting into Cauchy's theorem

$$\begin{aligned} f_i(\omega) &= I_R + I_L + I_\infty \\ &= \frac{1}{\pi}\int_{\omega_0}^{\infty} Imf_i(\omega')d\omega'(\frac{1}{\omega' - \omega} + \frac{1}{\omega' + \omega}) + I_\infty \\ &= \frac{2}{\pi}\int_{\omega_0}^{\infty} \frac{Imf_i(\omega')\omega' d\omega'}{\omega'^2 - \omega^2} + I_\infty. \end{aligned} \tag{A.27}$$

A contribution I_∞ from infinity does depend on the asymptotic behavior of $f_i(\omega)$. The GDH sum rule assumes that $I_\infty = 0$. We cannot say a priori that the above assumption is valid. It will remain the biggest open question and the weakest link in our discussion of the GDH sum rule. The same asymptotic behavior has to provide convergence for the part of the integral that comes from the cuts.

To illustrate the requirements on the asymptotic behavior of $f(\omega')$, we can take contour C_∞ to be a part of a circle $\omega' = Re^{i\phi}$ where (R, ϕ) are the polar coordinates of ω' in the complex plane. Taking the contour C to infinity corresponds to taking R to infinity. If for example $f(\omega') \to A$ where A is a constant then

$$I_\infty \to \frac{1}{2\pi i}\int_{C_\infty} \frac{Ad\omega'}{\omega' - \omega} = \frac{1}{2\pi i}\int_{C_\infty} \frac{Ad(Re^{i\phi})}{Re^{i\phi} - \omega} \to \frac{1}{2\pi i}\int_{C_\infty} \frac{ARe^{i\phi}id\phi}{Re^{i\phi}} = \frac{1}{2\pi i}\int_{C_\infty} Aid\phi = A. \tag{A.28}$$

In this case the GDH sum rule will be valid only if the constant A is equal to zero.

A.0.4 Low Energy Theorem

One of the important ingredients of the GDH Sum rule is the Low Energy Theorem. This theorem states that at low energies, the interaction of an electron with a spin $\frac{1}{2}$ hadron does not depend on the details of the hadron structure. This result has been first shown by F. E. Low [18], 1954, M. Gell-Mann and M. L. Goldberger [19], 1954. We will follow the treatment of the subject by V. B. Berestetskii, E. M. Lifshits and L. P. Pitaevskii [20].

In the low energy limit, the scattering amplitude M, as a function of photon energy, generally can have a regular and an irregular part.

$$M = M_r + M_i. \tag{A.29}$$

The regular part M_r can be decomposed into a Taylor series of the form

$$M_r = \sum_{i,j}^{\infty} a_{ij}\omega^i {\omega'}^j, \tag{A.30}$$

where ω is the energy of the incident photon and ω' is the energy of the scattered photon. The irregular part M_i can have poles: that is, terms of the form $\frac{1}{\omega}, \frac{1}{\omega^2}$, etc. From field theory we know that poles can come only from one-particle intermediate states [16]. Multipartical intermediate states cannot produce poles in the amplitude M. This result is clear in the context of perturbation theory, and it is actually a general result relying only on principles of relativity and quantum mechanics [16].

For the case of an electron colliding with a spin $\frac{1}{2}$ hadron, there are only two diagrams that have a one-particle intermediate state (see Fig A-3). As a consequence only these two diagrams can have poles. In these two diagrams electromagnetic vertices are well defined. They include electromagnetic formfactors. Since both photons are real, the formfactors have to be taken at $Q^2 = 0$ where their value is equal to the electric charge e and the anomalous magnetic moment μ_a.

The contribution of the pole diagrams to the scattering amplitude can be calculated directly.

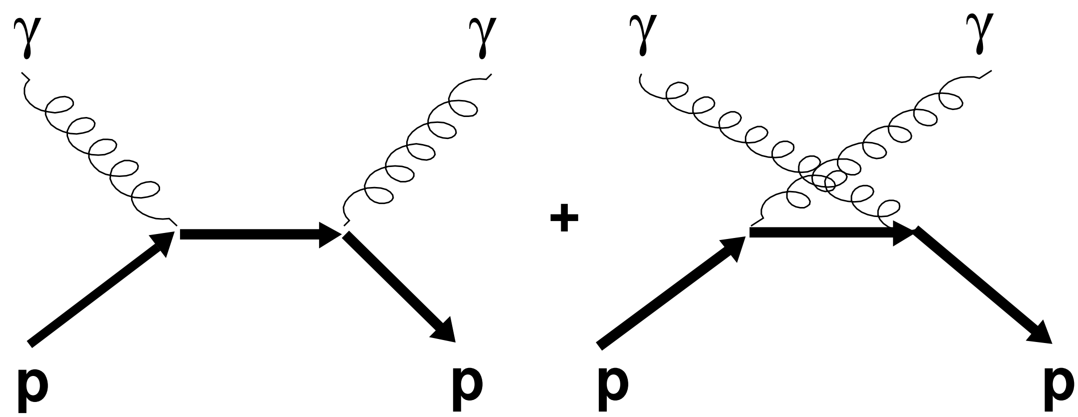

Figure A-3: Compton scattering from a nucleon. Irregular part of the amplitude.

$$M_i = -4\pi(e^2)e'^{*}_{\mu} e_\nu(\bar{u}' Q^{\mu\nu} u), \tag{A.31}$$

where e_ν, e'^{*}_{μ} are the polarization vectors of the incident and scattered photons respectively. $u, \bar{u}'$ are the spinors of the incident and scattered hadrons. The hadron mass is M.

$$Q^{\mu\nu} = (\gamma^\mu + S'^\mu)\frac{\gamma p + \gamma k + M}{s - M^2}(\gamma^\nu - S^\nu) + (\gamma^\nu - S^\nu)\frac{\gamma p - \gamma k' + M}{u - M^2}(\gamma^\mu + S'^\mu), \tag{A.32}$$

where

$$s = (p + k)^2, \tag{A.33}$$

$$u = (p' - k)^2, \tag{A.34}$$

$$eS^{\mu} \equiv \mu_{an} \sigma^{\mu\gamma} k_{\lambda}, \tag{A.35}$$

$$eS'^{\mu} \equiv \mu_{an} \sigma^{\mu\gamma} k'_{\lambda}, \tag{A.36}$$

and k, k', p, p' are the 4-momenta of the incident and scattered photons and protons respectively. γ^{ν} are Dirac gamma matrices. $\sigma^{\mu\gamma} \equiv \frac{1}{2}(\gamma^{\mu}\gamma^{\gamma} - \gamma^{\gamma}\gamma^{\mu})$. It can be proved that

$$k'_{\mu}(\bar{u}' Q^{\mu\nu} u) = (\bar{u}' Q^{\mu\nu} u) k_{\nu} = 0 \tag{A.37}$$

since $k^2 = 0$, $(\gamma k)^2 = 0$, $kS = k'S' = 0$.

The total amplitude M for our process has two external photons and, as a consequence, has the following form:

$$M = e_{\mu}^{'*} e_{\nu} D^{\mu\nu}(k, k'), \tag{A.38}$$

where $D(k, k')$ is a part of the total amplitude with polarization vectors $e_{\mu}^{'*}$ and e_{ν} explicitly displayed. We define

$$D_1^{\mu}(k, k') = e_{\nu} D^{\mu\nu}(k, k'), \tag{A.39}$$

and

$$D_2^{\nu}(k, k') = e_{\mu}^{'*} D^{\mu\nu}(k, k'). \tag{A.40}$$

From the Ward identity [16],

$$k_{\mu} D^{\mu\nu} = k'_{\nu} D^{\mu\nu} = 0. \tag{A.41}$$

This is just a direct consequence of gauge invariance, which can be seen from the following consideration. External photons are created by the interaction term $\int d^4xej^\mu A_\mu$, and we expect D_1^μ (similar applies to D_2^ν) to be a matrix element of the Heisenberg field j^μ:

$$D_1^\mu = \int d^4xe^{ikx} < f]j^\mu(x)|i >, \tag{A.42}$$

where the initial and the final states include all particles except the final photon (in the case of D_2^ν, the initial photon). From gauge invariance, it follows that the electromagnetic current $j^\mu = \bar{\psi}\gamma\psi$ is conserved: $\partial_\mu j^\mu(x) = 0$, immediately giving us (A.41).

We can again use our decomposition of the amplitude into the regular and irregular part

$$M = e_\mu^{'*}e_\nu D^{\mu\nu}(k,k') = e_\mu^{'*}e_\nu(D_r^{\mu\nu}(k,k') + D_i^{\mu\nu}(k,k')). \tag{A.43}$$

Since from (A.31) $D_i^{\mu\nu} = -4\pi(\bar{u}'Q^{\mu\nu}u)$, from (A.37)

$$k_\mu D_i^{\mu\nu} = k'_\nu D_i^{\mu\nu} = 0. \tag{A.44}$$

Because $D^{\mu\nu} = D_i^{\mu\nu} + D_r^{\mu\nu}$ using (A.41) we conclude

$$k_\mu D_r^{\mu\nu} = k'_\nu D_r^{\mu\nu} = 0. \tag{A.45}$$

To summarize, the total amplitude is gauge invariant. We have proved by direct computation that the irregular part is gauge invariant by itself , and as a consequence, the regular part also has to be invariant.

Using (A.45) and our decomposition (A.30) of the regular amplitude into a power series in photon momenta k, k', we get

$$0 = k_\nu D_r^{\mu\nu} = k_\nu \sum_{n=0,k=0}^{\infty} b_{n,k}^{\mu\nu\alpha_0...\alpha_n\beta_0...\beta_k} k_{\alpha_0}...k_{\alpha_n}k'_{\beta_0}...k'_{\beta_k}. \tag{A.46}$$

Since k, k' are arbitrary and the expression has to be zero for any k, k', we conclude that each term in the decomposition, as a power of k, as well as each term in the decomposition as a power of k', has to be zero by itself. The term $b^{\mu\nu\alpha_0}_{n=0}(k')k$ which is the first in the series can be 0 for any k only if $b^{\mu\nu\alpha_0}_{n=0}(k') \equiv 0$ (for a moment we have absorbed the k' dependence into the coefficients b). Consequently, the decomposition has to include at least one power of k and, by the same reasoning, at least one power of k'.

$$D^{\mu\nu}_r = \sum_{n=1,k=1}^{\infty} b^{\mu\nu\alpha_0...\alpha_n\beta_0...\beta_k}_{n,k} k_{\alpha_0}...k_{\alpha_n} k'_{\beta_0}...k'_{\beta_k} = b^{\mu\nu\alpha_1\beta_1}_{1,1} k_{\alpha_1} k'_{\beta_1} + (...) \tag{A.47}$$

Since the energy of the scattered photon ω' is of the same order of magnitude as energy of the incident photon ω, $\omega' \sim \omega$, the regular part of the amplitude starts with terms $\sim \omega^2$ and doesn't contribute to the scattering amplitude in the first and second order. The contribution from the irregular part can be calculated directly and involves the charge, mass and the anomalous magnetic moment as the only quantities we need to know about hadron structure [20].

$$T(\omega) = -\frac{\alpha}{M_p} + i\omega\sigma[\epsilon^*\epsilon](-\frac{\alpha\mu_a^2}{2M_p^2}). \tag{A.48}$$

A.0.5 Putting All the Pieces Together

From consideration of the forward Compton scattering in Section A.0.2 we concluded that

$$T(\omega) = f_1(\omega)(\epsilon^*\epsilon) + 2i\omega f_2(\omega)(s[\epsilon^*\epsilon]), \tag{A.49}$$

$$Imf_i(\omega) = \frac{\omega^{2-i}}{8\pi}(\sigma_{\frac{1}{2}} + (-1)^{i-1}\sigma_{\frac{3}{2}}). \tag{A.50}$$

In Section A.0.3 using causality, under the assumption of the accepted behavior of $f_i(\omega)$ at infinity, we proved the dispersion relationship:

$$f_i(\omega) = \frac{2}{\pi}\int_{\omega_0}^{\infty} \frac{Imf_i(\omega')\omega' d\omega'}{\omega'^2 - \omega^2}. \tag{A.51}$$

For example, this relationship is valid if $f_i(\omega)$ goes to zero at infinity and invalid if it goes to any other constant.

In Section A.0.4, using gauge invariance, we proved that for low ω, the Compton scattering amplitude behaves like

$$T(\omega) = -\frac{\alpha}{M_p} + i\omega(\sigma[\epsilon^*\epsilon])(-\frac{\alpha\mu_a^2}{2M_p^2}) + O(\omega^2). \tag{A.52}$$

This implies that

$$f_1(0) = -\frac{\alpha}{M_p}, \tag{A.53}$$

$$f_2(0) = -\frac{\alpha\mu_a^2}{2M_p^2}. \tag{A.54}$$

Substituting $Imf_2(\omega)$ into (A.51) we get

$$f_2(\omega) = \frac{1}{4\pi^2}\int_{\omega_0}^{\infty} \frac{(\sigma_{\frac{1}{2}}(\omega') - \sigma_{\frac{3}{2}}(\omega'))\omega' d\omega'}{\omega'^2 - \omega^2}. \tag{A.55}$$

Taking the limit $\omega \to 0$ and using the Low Energy Theorem:

$$-\frac{\alpha\mu_a^2}{2M_p^2} = f_2(0) = \frac{1}{4\pi^2}\int_{\omega_0}^{\infty} \frac{(\sigma_{\frac{1}{2}}(\omega') - \sigma_{\frac{3}{2}}(\omega'))d\omega'}{\omega'}. \tag{A.56}$$

Finally the GDH sum rule is

$$\int_{\omega_0}^{\infty} \frac{(\sigma_{\frac{1}{2}}(\omega') - \sigma_{\frac{3}{2}}(\omega'))d\omega'}{\omega'} = -\frac{2\pi^2\alpha\mu_a^2}{M_p^2}. \tag{A.57}$$

Appendix B

Data Tables for the $g_1(W, Q^2)$ Polarized Structure Function

The following tables contain data for the $g_1(W, Q^2)$ polarized structure function. The data are shown in Figures 4-8-4-13.

Table B.1: $g_1(W, Q^2)$ polarized structure function for $Q^2 = 0.19 GeV^2/c^2$.

W, GeV	$g_1(W, Q^2)$	Error stat	Error syst
1.11	-0.0444	0.0147	0.0059
1.15	-0.0615	0.0160	0.0084
1.19	-0.0923	0.0178	0.0124
1.23	-0.1138	0.0194	0.0153
1.27	-0.0231	0.0202	0.0047
1.31	0.0205	0.0208	0.0039
1.35	0.0511	0.0215	0.0069
1.39	0.0512	0.0225	0.0067
1.43	0.0397	0.0236	0.0052
1.47	0.0958	0.0252	0.0126
1.51	0.1547	0.0268	0.0204
1.55	0.1168	0.0280	0.0161
1.59	0.0903	0.0291	0.0135
1.63	0.0404	0.0304	0.0095
1.67	0.0554	0.0319	0.0116
1.71	0.0948	0.0330	0.0160
1.75	0.1721	0.0339	0.0251
1.79	0.0686	0.0346	0.0153
1.83	0.0191	0.0342	0.0136
1.87	0.0855	0.0334	0.0181
1.91	-0.0009	0.0319	0.0150
1.95	-0.0010	0.0308	0.0158
1.99	-0.0232	0.0311	0.0169

Table B.2: $g_1(W, Q^2)$ polarized structure function for $Q^2 = 0.24 GeV^2/c^2$.

W, GeV	$g_1(W, Q^2)$	Error stat	Error syst
1.11	0.0135	0.0277	0.0027
1.15	-0.1164	0.0326	0.0158
1.19	-0.1832	0.0385	0.0250
1.23	-0.2794	0.0429	0.0377
1.27	-0.0802	0.0450	0.0141
1.31	-0.0105	0.0460	0.0080
1.35	0.0859	0.0471	0.0126
1.39	0.1135	0.0486	0.0152
1.43	0.0435	0.0508	0.0058
1.47	0.0790	0.0538	0.0103
1.51	0.0995	0.0565	0.0132
1.55	0.0979	0.0585	0.0134
1.59	0.0216	0.0601	0.0064
1.63	0.0018	0.0622	0.0071
1.67	0.0300	0.0643	0.0092
1.71	0.0000	0.0660	0.0094
1.75	-0.0246	0.0675	0.0109
1.79	0.0650	0.0687	0.0143
1.83	0.0409	0.0689	0.0135
1.87	0.0463	0.0697	0.0147
1.91	-0.0451	0.0715	0.0154
1.95	0.0424	0.0767	0.0160
1.99	0.0766	0.0806	0.0187

Table B.3: $g_1(W,Q^2)$ polarized structure function for $Q^2 = 0.33 GeV^2/c^2$.

W, GeV	$g_1(W,Q^2)$	Error stat	Error syst
1.11	-0.0345	0.0194	0.0049
1.15	-0.0763	0.0222	0.0108
1.19	-0.1400	0.0258	0.0196
1.23	-0.1716	0.0285	0.0241
1.27	-0.1216	0.0298	0.0181
1.31	-0.0313	0.0305	0.0083
1.35	-0.0104	0.0313	0.0053
1.39	0.0439	0.0324	0.0064
1.43	0.0365	0.0339	0.0048
1.47	0.0928	0.0358	0.0121
1.51	0.0779	0.0377	0.0107
1.55	0.0880	0.0392	0.0128
1.59	0.1013	0.0403	0.0151
1.63	0.1102	0.0415	0.0169
1.67	-0.0087	0.0426	0.0103
1.71	0.0386	0.0437	0.0126
1.75	0.0794	0.0445	0.0164
1.79	0.0539	0.0456	0.0156
1.83	0.1275	0.0474	0.0224
1.87	0.0541	0.0496	0.0175
1.91	0.1009	0.0517	0.0215
1.95	0.0236	0.0537	0.0182
1.99	0.0706	0.0558	0.0210

Table B.4: $g_1(W,Q^2)$ polarized structure function for $Q^2 = 0.45 GeV^2/c^2$.

W, GeV	$g_1(W,Q^2)$	Error stat	Error syst
1.11	-0.0462	0.0263	0.0063
1.15	-0.0748	0.0294	0.0105
1.19	-0.0964	0.0333	0.0140
1.23	-0.1059	0.0365	0.0156
1.27	-0.0605	0.0379	0.0107
1.31	0.0110	0.0388	0.0061
1.35	-0.0389	0.0395	0.0065
1.39	0.0257	0.0406	0.0039
1.43	0.0537	0.0422	0.0070
1.47	0.1265	0.0445	0.0166
1.51	0.0897	0.0468	0.0125
1.55	0.1103	0.0487	0.0159
1.59	0.1220	0.0505	0.0180
1.63	0.1212	0.0531	0.0188
1.67	0.1037	0.0558	0.0179
1.71	0.0694	0.0586	0.0160
1.75	0.0125	0.0603	0.0147
1.79	0.0744	0.0619	0.0186
1.83	-0.0177	0.0639	0.0173
1.87	0.1097	0.0666	0.0232

Table B.5: $g_1(W, Q^2)$ polarized structure function for $Q^2 = 0.55 GeV^2/c^2$.

W, GeV	$g_1(W, Q^2)$	Error stat	Error syst
1.11	0.0218	0.0254	0.0034
1.15	-0.0101	0.0277	0.0040
1.19	-0.0928	0.0310	0.0132
1.23	-0.1154	0.0334	0.0162
1.27	-0.0519	0.0349	0.0090
1.31	0.0382	0.0359	0.0070
1.35	0.0320	0.0370	0.0053
1.39	0.0432	0.0387	0.0058
1.43	0.0662	0.0408	0.0086
1.47	0.0652	0.0434	0.0088
1.51	0.2056	0.0458	0.0272
1.55	0.1312	0.0482	0.0185
1.59	0.0814	0.0502	0.0139
1.63	0.0764	0.0526	0.0146
1.67	0.0755	0.0548	0.0157
1.71	0.1830	0.0565	0.0275
1.75	0.1952	0.0584	0.0296
1.79	0.0075	0.0606	0.0168

Table B.6: $g_1(W, Q^2)$ polarized structure function for $Q^2 = 0.69 GeV^2/c^2$.

W, GeV	$g_1(W, Q^2)$	Error stat	Error syst
1.11	-0.0209	0.0179	0.0032
1.15	-0.0475	0.0196	0.0070
1.19	-0.0482	0.0217	0.0074
1.23	-0.1017	0.0236	0.0140
1.27	-0.0310	0.0246	0.0061
1.31	0.0459	0.0254	0.0070
1.35	0.0589	0.0263	0.0080
1.39	0.0367	0.0276	0.0048
1.43	0.0336	0.0291	0.0044
1.47	0.0766	0.0310	0.0103
1.51	0.1717	0.0328	0.0228
1.55	0.0856	0.0342	0.0131
1.59	0.1073	0.0356	0.0164
1.63	0.0698	0.0373	0.0137
1.67	0.0475	0.0391	0.0133
1.71	0.1082	0.0406	0.0194
1.75	0.1582	0.0419	0.0254

Table B.7: $g_1(W,Q^2)$ polarized structure function for $Q^2 = 0.89 GeV^2/c^2$.

W, GeV	$g_1(W,Q^2)$	Error stat	Error syst
1.11	0.0157	0.0119	0.0024
1.15	-0.0115	0.0127	0.0026
1.19	-0.0589	0.0140	0.0081
1.23	-0.0504	0.0151	0.0072
1.27	-0.0014	0.0159	0.0030
1.31	0.0229	0.0166	0.0038
1.35	0.0842	0.0173	0.0110
1.39	0.0065	0.0181	0.0009
1.43	0.0439	0.0190	0.0058
1.47	0.0996	0.0202	0.0132
1.51	0.1312	0.0214	0.0176
1.55	0.1395	0.0223	0.0192
1.59	0.0980	0.0231	0.0150
1.63	0.1283	0.0241	0.0191
1.67	0.1453	0.0253	0.0218
1.71	0.1732	0.0263	0.0257
1.75	0.1616	0.0265	0.0252
1.79	0.1338	0.0270	0.0233
1.83	0.0972	0.0271	0.0210
1.87	0.0959	0.0263	0.0219

Appendix C

Data Tables for the Polarized Cross Section Difference

The following tables contain data for cross section difference $\Delta\sigma(W, Q^2) = \frac{d\sigma^{\downarrow\uparrow}}{dW dQ^2} - \frac{d\sigma^{\uparrow\uparrow}}{dW dQ^2}$. This cross section difference is shown in Figures 4-1-4-6.

Table C.1: $\Delta\sigma(W, Q^2) = \frac{d\sigma^{\downarrow\uparrow}}{dWdQ^2} - \frac{d\sigma^{\uparrow\uparrow}}{dWdQ^2}, \mu BnGeV^{-3}$ for $Q^2 = 0.19GeV^2/c^2$.

W, GeV	$\Delta\sigma(W, Q^2)$	Error stat	Error syst
1.11	0.1186	0.1462	0.0154
1.15	0.0070	0.1545	0.0009
1.19	-0.1038	0.1661	0.0135
1.23	-0.5146	0.1687	0.0669
1.27	-0.3530	0.1603	0.0459
1.31	-0.0012	0.1488	0.0002
1.35	0.0989	0.1396	0.0129
1.39	0.0192	0.1334	0.0025
1.43	0.0911	0.1310	0.0118
1.47	0.0281	0.1307	0.0037
1.51	0.0571	0.1292	0.0074
1.55	0.0536	0.1250	0.0070
1.59	0.0198	0.1207	0.0026
1.63	-0.0282	0.1167	0.0037
1.67	0.0088	0.1135	0.0011
1.71	0.2115	0.1093	0.0275
1.75	-0.0113	0.1055	0.0015
1.79	-0.0057	0.1021	0.0007
1.83	0.1486	0.0995	0.0193
1.87	-0.0189	0.0966	0.0025
1.91	0.0566	0.0923	0.0074
1.95	0.0622	0.0869	0.0081
1.99	-0.0097	0.0892	0.0013

Table C.2: $\Delta\sigma(W,Q^2) = \frac{d\sigma^{\downarrow\uparrow}}{dWdQ^2} - \frac{d\sigma^{\uparrow\uparrow}}{dWdQ^2}, \mu BnGeV^{-3}$ for $Q^2 = 0.24GeV^2/c^2$.

W, GeV	$\Delta\sigma(W,Q^2)$	Error stat	Error syst
1.11	0.2677	0.0883	0.0348
1.15	-0.1072	0.0922	0.0139
1.19	-0.1983	0.0982	0.0258
1.23	-0.4110	0.0995	0.0534
1.27	-0.0481	0.0955	0.0063
1.31	0.0456	0.0900	0.0059
1.35	0.1931	0.0852	0.0251
1.39	0.2197	0.0818	0.0286
1.43	0.0930	0.0799	0.0121
1.47	0.1309	0.0790	0.0170
1.51	0.1489	0.0779	0.0194
1.55	0.1505	0.0759	0.0196
1.59	0.0543	0.0734	0.0071
1.63	0.0282	0.0716	0.0037
1.67	0.0654	0.0700	0.0085
1.71	0.0290	0.0679	0.0038
1.75	0.0009	0.0658	0.0001
1.79	0.0851	0.0634	0.0111
1.83	0.0606	0.0603	0.0079
1.87	0.0615	0.0578	0.0080
1.91	-0.0156	0.0562	0.0020
1.95	0.0484	0.0571	0.0063
1.99	0.0694	0.0569	0.0090

Table C.3: $\Delta\sigma(W,Q^2) = \frac{d\sigma^{\downarrow\uparrow}}{dWdQ^2} - \frac{d\sigma^{\uparrow\uparrow}}{dWdQ^2}, \mu BnGeV^{-3}$ for $Q^2 = 0.33GeV^2/c^2$.

W, GeV	$\Delta\sigma(W,Q^2)$	Error stat	Error syst
1.11	0.0477	0.0380	0.0062
1.15	-0.0226	0.0394	0.0029
1.19	-0.0928	0.0418	0.0121
1.23	-0.1418	0.0426	0.0184
1.27	-0.1098	0.0411	0.0143
1.31	-0.0090	0.0391	0.0012
1.35	0.0054	0.0373	0.0007
1.39	0.0634	0.0362	0.0082
1.43	0.0473	0.0355	0.0061
1.47	0.0936	0.0353	0.0122
1.51	0.0717	0.0350	0.0093
1.55	0.0929	0.0343	0.0121
1.59	0.1021	0.0333	0.0133
1.63	0.1041	0.0324	0.0135
1.67	0.0132	0.0316	0.0017
1.71	0.0444	0.0307	0.0058
1.75	0.0682	0.0296	0.0089
1.79	0.0492	0.0288	0.0064
1.83	0.0910	0.0284	0.0118
1.87	0.0437	0.0282	0.0057
1.91	0.0660	0.0279	0.0086
1.95	0.0220	0.0275	0.0029
1.99	0.0426	0.0271	0.0055

Table C.4: $\Delta\sigma(W,Q^2) = \frac{d\sigma^{\downarrow\uparrow}}{dWdQ^2} - \frac{d\sigma^{\uparrow\uparrow}}{dWdQ^2}, \mu BnGeV^{-3}$ for $Q^2 = 0.45GeV^2/c^2$.

W, GeV	$\Delta\sigma(W,Q^2)$	Error stat	Error syst
1.11	0.0009	0.0313	0.0001
1.15	-0.0271	0.0323	0.0035
1.19	-0.0355	0.0338	0.0046
1.23	-0.0485	0.0345	0.0063
1.27	-0.0282	0.0335	0.0037
1.31	0.0231	0.0321	0.0030
1.35	-0.0214	0.0307	0.0028
1.39	0.0256	0.0298	0.0033
1.43	0.0415	0.0292	0.0054
1.47	0.0820	0.0291	0.0107
1.51	0.0544	0.0290	0.0071
1.55	0.0759	0.0285	0.0099
1.59	0.0811	0.0281	0.0105
1.63	0.0759	0.0280	0.0099
1.67	0.0632	0.0280	0.0082
1.71	0.0430	0.0279	0.0056
1.75	0.0157	0.0272	0.0020
1.79	0.0418	0.0266	0.0054
1.83	0.0017	0.0261	0.0002
1.87	0.0508	0.0259	0.0066

Table C.5: $\Delta\sigma(W,Q^2) = \frac{d\sigma^{\downarrow\uparrow}}{dWdQ^2} - \frac{d\sigma^{\uparrow\uparrow}}{dWdQ^2}, \mu BnGeV^{-3}$ for $Q^2 = 0.55GeV^2/c^2$.

W, GeV	$\Delta\sigma(W,Q^2)$	Error stat	Error syst
1.11	0.0540	0.0219	0.0070
1.15	0.0257	0.0223	0.0033
1.19	-0.0328	0.0233	0.0043
1.23	-0.0517	0.0235	0.0067
1.27	-0.0199	0.0231	0.0026
1.31	0.0323	0.0224	0.0042
1.35	0.0246	0.0218	0.0032
1.39	0.0294	0.0216	0.0038
1.43	0.0386	0.0216	0.0050
1.47	0.0333	0.0218	0.0043
1.51	0.0983	0.0218	0.0128
1.55	0.0679	0.0218	0.0088
1.59	0.0452	0.0216	0.0059
1.63	0.0407	0.0215	0.0053
1.67	0.0377	0.0213	0.0049
1.71	0.0758	0.0209	0.0099
1.75	0.0760	0.0206	0.0099
1.79	0.0097	0.0203	0.0013

Table C.6: $\Delta\sigma(W,Q^2) = \frac{d\sigma^{\downarrow\uparrow}}{dWdQ^2} - \frac{d\sigma^{\uparrow\uparrow}}{dWdQ^2}, \mu BnGeV^{-3}$ for $Q^2 = 0.69 GeV^2/c^2$.

W, GeV	$\Delta\sigma(W,Q^2)$	Error stat	Error syst
1.11	0.0068	0.0104	0.0009
1.15	-0.0080	0.0107	0.0010
1.19	-0.0065	0.0112	0.0008
1.23	-0.0353	0.0115	0.0046
1.27	-0.0075	0.0114	0.0010
1.31	0.0243	0.0112	0.0032
1.35	0.0281	0.0110	0.0037
1.39	0.0181	0.0110	0.0024
1.43	0.0159	0.0110	0.0021
1.47	0.0294	0.0112	0.0038
1.51	0.0614	0.0113	0.0080
1.55	0.0348	0.0112	0.0045
1.59	0.0406	0.0111	0.0053
1.63	0.0269	0.0111	0.0035
1.67	0.0195	0.0111	0.0025
1.71	0.0347	0.0110	0.0045
1.75	0.0464	0.0108	0.0060

Table C.7: $\Delta\sigma(W,Q^2) = \frac{d\sigma^{\downarrow\uparrow}}{dWdQ^2} - \frac{d\sigma^{\uparrow\uparrow}}{dWdQ^2}, \mu BnGeV^{-3}$ for $Q^2 = 0.89GeV^2/c^2$.

W, GeV	$\Delta\sigma(W,Q^2)$	Error stat	Error syst
1.11	0.0146	0.0043	0.0019
1.15	0.0044	0.0044	0.0006
1.19	-0.0104	0.0046	0.0013
1.23	-0.0084	0.0048	0.0011
1.27	0.0029	0.0048	0.0004
1.31	0.0081	0.0048	0.0011
1.35	0.0246	0.0048	0.0032
1.39	0.0031	0.0048	0.0004
1.43	0.0127	0.0049	0.0017
1.47	0.0251	0.0049	0.0033
1.51	0.0321	0.0050	0.0042
1.55	0.0358	0.0050	0.0047
1.59	0.0257	0.0049	0.0033
1.63	0.0305	0.0049	0.0040
1.67	0.0322	0.0050	0.0042
1.71	0.0364	0.0049	0.0047
1.75	0.0331	0.0048	0.0043
1.79	0.0268	0.0046	0.0035
1.83	0.0190	0.0044	0.0025
1.87	0.0175	0.0041	0.0023

Bibliography

[1] Goossens, Michel, *The LaTeX companion,* (New York: Addison, 1994).

[2] S. B. Gerasimov, Yadernaya Fizika, 1965.

[3] S. B. Gerasimov, Sov. J. Nucl. Phys., 2, 430 (1966).

[4] J. D. Bjorken, Phys. Rev. 148, 1467 (1966).

[5] A. S. Raskin and T.W. Donnelly, Ann. Phys. 191, 78 (1989)

[6] T.W. Donnelly, Course Lectures, MIT (1997), Cambridge, USA.

[7] K. Abe *et al.,* (E143 Collaboration), Phy. Rev. Lett. 78, 815 (1997).

[8] E143, K. Abe *et al.*, Phys. Rev. Lett. 74, 346 (1995); Phys. Rev. Lett. 75, 25 (1995); Phys. Rev. Lett. 76, 587 (1996).

[9] E143 Collaboration, K. Abe *et al.,* Phys. Rev., D58, 112003 (1998).

[10] E142, P. L. Anthony *et al.,* Phys. Rev. Lett. 71, 959 (1993).

[11] The E142 Collaboration Phys. Rev. D 49, 4348 (1994).

[12] D. S. Carman *et al.,* NIM A 419, 315 (1998).

[13] H. A. Kramers, Atti Congr. Intern. Fisici Como (1927).

[14] R. Kronig, J. Op. Soc. Am., 12, 547 (1926).

[15] J. D. Bjorken, S. D. Drell "Relativistic Quantum Fields," McGraw-Hill, Inc, (1965).

[16] M. E. Peskin, D. V. Schroeder, “An Introduction to Quantum Field Theory.”

[17] S. G. Krantz, “Function Theory Of Several Complex Variables”.

[18] F. E. Low, Phys. Rev. 96, 1428 (1954).

[19] M. Gell-Mann and M. L. Goldberger, Phys. Rev. 96, 1433 (1954).

[20] L.D. Landau, “Quantum Electrodynamics.”

[21] J. Yun, “DC Calibration Procedures,” clas-notes (1999).

[22] “The Region One Drift Chamber for the Jefferson Laboratory,” CMU Progress Report (1997-1998).

[23] A. V. Vlasov, M. V. Kossov, V. D. Burkert, “CLAS Cerenkov Detector Simulations and Design Analysis.”

[24] E. S. Smith *et al.*, “The Time-of-flight System for CLAS,” Nucl. Instr. and Meth. A432, 265-298 (1999).

[25] Jefferson Laboratory Picture Archive.

[26] E. S. Smith *et al.*, “Calibration of the CLAS TOF System,” CLAS-notes 99-011.

[27] Raffaella De Vita, Ph. D. Thesis.

[28] J. Soffer and O. Teryaev, Phys Rev. Lett. 70, 3373 (1993).

[29] J. Soffer and O. Teryaev, Phys Rev. D 51, 25 (1995).

[30] J. Soffer and O. Teryaev, Phys Rev. D 56, 7458 (1997).

[31] M. Anselmino, B. L. Ioffe, and E. Leader, Yad. Fiz. 49, 214 (1989).

[32] M. Anselmino, B. L. Ioffe, and E. Leader, Sov. J. Nucl. Phys. 49, 136 (1989).

[33] V. D. Burkert and B. L. Ioffe, Phys. Lett. B 296, 223 (1992).

[34] V. D. Burkert and B. L. Ioffe, Zh. Eksp. Teor. Fiz. 105, 1153 (1994), [JETP 105, 619 (1994)].

[35] V. Bernard, N. Kaiser, and U. G. Meissner, Phys. Rev. D 48, 3062 (1993).

[36] S. Stepanyan, R. Hutchins, private communications.

[37] Peter Bosted, “Pair symmetric contributions to EG1,” EG1 collaboration document.

[38] Y. S. Tsai, Rev. Mod. Phys., 46, 815(1974).

[39] G. Mitchell, E155 collaboration, arXiv:hep-ex/9903055v1 (1999).

[40] S. Kuhn, “EG1 Analysis - Models for inclusive cross sections and Asymmetries,” EG1 collaboration document, JLab.

[41] S. Kuhn, “Models for the Asymmetry A_2,” submitted to World Scientific on July 11, 2001.

[42] S. Kuhn, Hampton University Graduate Summer School (HUGS ’97).

[43] Phys. Lett. B 452, 194-200 (1999)

[44] R. Pantforder, “Investigations on the Foundation and Possible Modifications of the Gerasimov-Drell-Hearn Sum Rule”, Ph. D. Thesis, Bonn, Germany, BONN-IR-98-06.

[45] Wu-Yang Tsai, L. Deraad, K. A. Milton, Phys. Rev. D 11, 3537 (1975).

[46] H. Burkhardt and W.N. Cottingham, Ann. Phys. (N.Y.) 56, 543 (1970).

[47] J. Schwinger, Proc. Natl. Acad. Sci. USA 72, 1 (1975); 72, 1559 (1975).

[48] N. Isgur and G. Karl, Phys. Lett 72B, 109 (1977).

[49] Z. Li, “Polarized Structure Function of the Nucleon in the Resonance Region,” Phys. Rev. D 47, 1854 (1993).

[50] "The Nucleon Drell Hearn Gerasimov Sum Rule within a relativistic quark model," Phys. Lett. B 418, 237 (1998).

[51] V. Burkert, "Generalized Gerasimov-Drell-Hearn Sum Rule for the Proton-Neutron Difference in Chiral Pertubation Theory," JLAB-PHY-00-03, nucl-th/0004001 (2000).

[52] X. Ji and J. Osborne, hep-ph/9905410.

[53] "What do we know about the Q^2 evolution of the Gerasimov-Drell-Hearn sum rule ?", V. Burkert, Z. Li, Phys. Rev. D 47, 46 (1993).

[54] Ashman *et al.*, Phys. Lett. B 206, 364 (1998).

[55] Ashman *et al.*, Nucl. Phys. B 328, 1 (1990).

[56] Airapetian *et al.*, "The Q^2-dependence of the Generalised Gerasimov-Drell-Hearn Integral for the Proton," Phys. Lett. B 494 (2000).

[57] K. Ackerstaff *et al.*, "Determination of the Deep Inelastic Contribution to the Generalised Gerasimov-Drell-Hearn Integral for the Proton and Neutron," Phys. Lett. B 444, 531-538 (1998).

[58] A. Airapetian *et al.*, "Measurement of the Proton Spin Structure Function g1p with a Pure Hydrogen Target," Phys. Lett. B 442, 484-492 (1998).

[59] N. Bianchi and E. Thomas, Phys. Lett. B 450, 439 (1999).

[60] SMC, B. Adeva *et al.,* Phys. Lett. B 302, 533 (1993); D. Adams *et al.*, Phys. Lett. B 329, 399 (1994); B 336, 125 (1994); B 357, 248 (1995).

[61] S. A. Larin, Phys. Lett. B 334, 192 (1994).

[62] E80, M. J. Alguard, *et al.,* Phys. Rev. Lett. 37, 1261 (1976); Phys. Rev. Lett. 41, 70 (1978); E130, G. Baum, *et al.,* Phys. Rev. Lett. 51, 1135 (1983).

[63] J. Ahrens, *et al.,* "First measurement of the Gerasimov-Drell-Hearn integral for Hydrogen from 200 to 800 MeV," Phys. Rev. Lett. 87 (2001).

[64] O. Hanstein *et al.*, Nucl. Phys. A 632, 561 (1998).

[65] R. A. Arndt et *al.*, Phys. Rev. C 53, 430 (1996).

[66] D. Drechsel *et al.*, Nucl. Phys. A 645, 145 (1999).

[67] P. McKee, Ph. D. Thesis, University of Virginia, 75-77 (2000).

[68] T. Averett, E155 Tech Note 27 (March 1997).

[69] R. Hutchins , Ph. D. Thesis, University of Virginia (2001).

[70] P. Bosted, Phys. Rev. C, 51, 409 (1995).

[71] K. Jones *et al.*, Phys. Rev. Let., 84, 1398 (2000).

[72] S. Simula *et al.*, arXiv:hep-ph/0107036v1 (2001).

[73] L. Mo, Y. Tsai, *Rev. Mod. Phys.*, 41, 205-235, (1969).

[74] T. V. Kukhto and N. M. Shumeiko, Nucl. Phys., B 219, 412 (1983).

[75] L. Stuart, "Radiative corrections program RCSLACPOL developed at SLAC and based on techniques by T. V. Kukhto and N. M. Shumeiko."

[76] J. Soffer and O. V. Teryaev, hep-ph/9906455.

[77] G. Dodge, private communications.

[78] R. Minehart, private communications.

[79] S. Kuhn, private communications.

[80] K. Griffioen, private communications.

[81] X. Ji and P. Unrau, Phys. Lett. B 333, 228 (1994).

[82] X. Ji, C. Kao, J. Osborne, Phys. Lett., B 472, 1, (2000).

[83] A. de Rujula, H. Georgi, and H. D. Politzer, Ann. Phys. 103, 315 (1977).

[84] A. Mueller and T. Trueman, Phys. Rev. 160, 1306 (1967).

[85] D. Drechsel, O. Hanstein, S. S. Kamalov, L. Tiator, nucl-th/9807001.

[86] "MySQL database for eg1 experiment," $http://claspc10.jlab.org/eg1$.

Acknowledgments

First of all, I would like to thank my adviser, William Bertozzi, for his guidance and support throughout my graduate career. His continuous help and advice made this research project possible. Bill has a remarkable physical intuition and I am fortunate to have the opportunity to learn experimental physics in his group. My special thanks to Shalev Gilad for many discussions about physics and suggestions during my time at MIT. I am grateful to the post-docs in our group, Zilu Zhao, David Rowntree, Kevin Fissum and Jianguo Zhao. Their help was essential, especially during my first years at MIT.

I would like to thank my thesis committee for various comments and suggestions which made my thesis more accurate. The critique of this thesis by Bill Donnelly and June Matthews greatly enhanced its readability and made discussion of the underling physics more clear.

I would like to express my appreciation to Volker Burkert for the leading role he played in the experiment. His guidance in the area of data analysis was crucial. I would like to thank Sebastian Kuhn for his leadership during data acquisition and data analysis. I wish to thank Ralph Minehart, Peter Bosted and Gail Dodge for their contributions to all stages of the experiment. I thank Keith Griffioen. His expertise in the area of radiative corrections was very helpful. Special thanks to Tony Forest. I had a plasure working with Tony on a number of software projects and data analysis issues.

I am very great-full to Stepan Stepanyan for his support of our group during detector calibrations and data analysis. My special gratitude to Mac Mestayer for giving me a guidance in the world of the Drift Chembers. Thanks to Arne Freyberger, who was very helpful during creation of the database for our experiment.

This experiment was a collaborative effort by a big team of technicians, engineers and scientiests. I thank the entire CLAS Collaboration and staff at Jefferson Laboratory for their contribution and their help.

I wish to thank Andrew Blinkovsky from Saharov Academy, BELARUS. Numerous discussions of the nature of physical laws were an important part of my aducation.

It is a pleasure to thank my first physics teacher, Verenich Ivan Fedorovich. He inspired me to be a physicist.

I would like to thank my cousin, Kiselev Alexander Vladimirovich, for the very useful discussions of the laws of Nature. He introduced me to the fascinating subject of Space Time Paradoxes and Black Holes. This subject sparkled my interest in Physics.

I thank my parents for the support they gave me during my years as a student.

Finally, I would like to thank my wife, Veronica, for her love, support and encouragement. Without her this thesis work would not be possible.